U N I V E R S I D A D
AUTÓNOMA DE MADRID

FACULTAD DE CIENCIAS

DEPARTAMENTO DE FÍSICA TEÓRICA

"Estudio submilimétrico de galaxias cercanas (Submillimetric study of nearby galaxies)"

Tesis de investigación presentada por

Ilhuiyolitzin Villicaña Pedraza

para acceder al grado de Doctora

Dentro del Programa Oficial de Posgrado de Astrofísica

Madrid 15 de Octubre de 2015, Madrid, España

Dirigida por

Jesus Martín Pintado y Angeles Díaz Beltrán

Dedicado a MI MADRE

a Paco, Paola y mi abuelo, motores de mi vida

A los que se fueron: Mi abuela y Antonio Sanchez

A todos aquellos que siempre creyeron en mi y me acompañaron sin dudar.

Agradecimientos

Una niña veia las estrellas desde el techo de su casa cada noche, la gente solia convncesrse con solo verlas pero la pequeña siempre queria saber porque brillaban, sus colores, sus tamaños y cada detalle de ellas, esa niña decidio que haria lo que fuera para entender las estrellas y fusionarse con ellas.
Agradezco a todos aquellos que conpartieron conmigo cada momento de mi vida, que siempre creyo en mi, amigos del trabajo, de la escuela. aquellos que me dieron su hombro para llorar pero que a la vez me levantaban.
Agradezco a mis amigos, familia, colegas y en especial a mi angel profesional Sergio Martin.
Agradezco a mi roomate Andy por su paciencia, a mis amigos.
Gracias a Jesus por la beca otorgada y Angeles Diaz por su apoyo.
Agradezco al MINECO por la beca otorgada para el desarrollo de este trabajo.

PREFACIO

La formacion de moleculas en el medio Interestelar es posible bajo condiciones de alta densidad en regiones dadas como consecuencia de colisiones entre atomos. Ademas, una molecula puede ser disociada por un foton UV. Polvo Interestelar puede actuar como proteccion en contra de la disociacion absorbiendo radiacion UV. Por consiguiente, la combinacion de particulas de alta densidad y la presencia de granos de polvo ayudan a la produccion y mantenimiento de moleculas que se encuentran en regiones frias y densas del medio Interestelar.

La formacion de moleculas de hidrogeno tiene lugar en reacciones en la superficie de los granos de polvo los cuales actuan como catalizadores de la reaccion y absorben el exceso de la energia libre durante la formacion de moleculas de H_2 molecule.

El mecanismo basico de formacion molecular en el medio interestelar es la reaccion en la cual una de las particulas esta cargada y es llamado reaccion ion-molecula. Esta clase de reaccion pueden producirse porque en las nubes moleculares hay iones, debido a rayos cosmicos dentro de la nube molecular.

La fotodisociacion del gas molecular por campos UV (regiones PDRs) es producida por la emision de grupos de estrellas OB formandose en el brote de formacion estelar (starburst). La emision molecular desde la regiones centrales de galaxias activas es una herramienta poderosa para entender los procesos fisicos que aumentan la actividad nuclear. El estudio de trazadores moleculares clave y su abundancia en cocientes pueden ser usados para establecer si el mecanismo de calentamiento dominante es debido a choques, regiones de fotodisociacion (PDRs) o regiones dominadas por rayos-x (XDRs). Choques, radiacion UV, rayos x y rayos cosmicos juegan un importante papel en la quimica de las nubes moleculares en el nucleo de galaxias.

Las colisiones generan mantos de hielo de monoxido de carbono, agua y metanol alrededor de

granos de polvo en regiones de alta extincion con densidades mas altas que 10^4 cm^{-3}. El material de los mantos podria regresar a la fase de gas por evaporacion o choques de onda. Fuertes choques pueden romper los granos, y se cree que la presencia de SiO en la fase de gas es un indicador de la presencia de tales choques.

Dentro de la nube, las moleculas pueden sobrevivir a la radiacion, y los iones son producidos por rayos cosmicos los cuales penetran en el interior de la nube molecular. La presencia de especies moleculares complejas que contienen carbon tales como formaldehyde H_2CO, cyanoacetylene C_3HN, formamide NH_2CHO y ethyl alcohol CH_3CH_2OH son considerados excelentes trazadores de quimica de granos de polvo.

En este trabajo se estudia la complejidad quimica y las condiciones fisicas del gas molecular en tres galaxias con diferentes tipos de actividad, en la muestra tenemos una galaxia con brotes de formacion estelar (starburst) NGC 253, una galaxia AGN (nucleo de galaxia activo) con nucleo de starburst NGC 4945 y una galaxia UltraLuminosa (ULIRG) Arp220.
De esta manera, el capitulo 1 nos ofrece una vision de la composicion quimica y condiciones fisicas del gas molecular, ademas de la informacion basica sobre los brotes de formacion estelar y el tipo de galaxias que se estudian en esta tesis.
El capitulo 2 nos habla de las observaciones llevadas a cabo y la instrumentacion empleada para la obtencion de los datos, ademas de informacion sobre la reduccion de los datos.
El capitulo 3 nos habla del analisis de los datos, asi como la identificacion de las lineas para conocer las moleculas encontradas en esa region.
En el capitulo 4 Se realiza un estudio multitransicion de la molecula de H_3O^+ usando modelos en Equilibrio Termodinamico Local (LTE) y fuera de Equilibrio (non-LTE) para explicar la sobreluminosidad de una transicion.
En el capitulo 5 se aborda el estudio de un sondeo submilimetrico de las galaxias NGC 253, NGC 4945 y Arp220 para identificacion y analisis de sus lineas moleculares.
En el capitulo 6 se muestra la deteccion de una nueva molecula, $HCNH^+$, su relacion con el origen y sobreabundancia de HNC siendo su posible precursor.
En el capitulo 7 se muestra la discusion de los resultados obtenidos en esta tesis, de la misma forma en capitulo 8 muestra las conclusiones.
Por ultimo en los apendices se muestran los conceptos basicos de la transferencia radiactiva, las tablas completas de los resultados y una vision teorica de las moleculas en en el medio extragalactico.

Preface

The formation of molecules in the Interstellar medium is possible under the condition of high densities in a given region as the consequence of the occurrence of collisions between atoms. Moreover, a molecule can be dissociated by an UV photon. Interestelar dust can act as a protection against dissociation since it will absorb any UV radiation. Hence the combination of a high particle density and the presence dust grains help the production and maintenence of molecules that are in the dense and cold regions of the Interstellar medium.

The formation of hydrogen molecules takes place in reactions on the surface of dust grains which act as catalysts of the reaction and absorb the excess of free energy during the formation of the H_2 molecule.

The basic mechanism of molecular formation in the Interstellar medium is the occurrence of reactions in which one of the particles involved is charged; these are named ion-molecule reactions. This kind of reactions can be produced because in the molecular clouds there are ions, due to cosmic rays inside the molecular cloud.

The photodisociation of the molecular gas by UV fields (PDRs regions) is produced by the emision of OB star groups formed in the starburst. The molecular emission from the central regions of active galaxies is a powerfull tool to understand the physical processes that give rise to the nuclear activity. The study of key molecular tracers and their abundance ratios can be used to establish if the dominant heating mechanism is due to shocks, photodisociation regions (PDR) or X-ray dominated regions (XDRs). Shocks, UV radiation, X rays and cosmic rays play an important rol in the chemistry of molecular clouds in the nuclei of galaxies.

These collisions generate icy mantles of carbon monoxide, water and methanol around dust grains in high extinction regions with densities of higher than 10^4 cm^{-3}. The mantle material

could be returned to the gas phase by evaporation or shock waves. Strong shocks can break the grains, and it is thought that the presence of SiO in the gas phase is an indicator of the presence of such shocks.

Inside the clouds, the molecules can survive at radiation, and ions are produced by cosmic rays which can penetrate into the interior of a molecular cloud. The presence of complex molecular species that contain carbon such as formaldehyde H_2CO, cyanoacetylene C_3HN, formamide NH_2CHO and ethyl alcohol CH_3CH_2OH are considered excellent tracers of dust grain chemistry.

This work is the study of the chemical complexity and the physical conditions of the molecular gas in three galaxies with different type of activity, in our sample we have a pure starburst (SB) galaxy NGC 253, a AGN with a nuclear starburst NGC 4945 and an UltraLuminous galaxy (ULIRG) Arp220.
On this way, chapter 1 show a vision of the chemical complexity and the physical condition of the molecular gas, also the basic information of the starburst galaxies.
Chapter 2 is about the observations carried out toward the galaxies, the used instrumentation for obtain data and the information of data reduction.
On the chapter 3 talk about the data analysis, the identification of the lines in this region.
A multitransition study of the molecule H_3O^+ is explained in the chapter 4 using Local Thermodinamical Equilibrium (LTE) models and out of Equilibrium (non-LTE models) in order to explain the overluminosity of one transition.
In the chapter 5, shown a submillimetric extragalactic line survey of the galaxies NGC 253, NGC 4945 and Arp220 for identification and analysis of their molecular lines.
A detection of a new extragalactic molecule $HCNH^+$ is explained in the chapter 6, also the origin of HNC overabundance.
In the chapter 7 is the discusion about the results obtained on this thesis and chapter 8 are the conclusions. Finally, Apendix show basic concepts of radiative transfer, complete fit gauss for the galaxies and concepts of molecules in the extragalactic medium..

Contents

List of Figures

List of Tables

Chapter

1 Introduction

1.1 Motivation

Starburst nuclei and active galaxies harbour large masses of molecular gas and dust in their interior. This molecular gas is closely linked to the feeding of the nuclear activity and therefore plays an important role in the evolution of the galaxy. Observations of the molecular gas properties help us to identify and analyze the type of activity in very deeply obscured galactic nuclei. Line ratios between molecular species may help to determine the physical conditions and chemistry of the gas, which could potentially help us to know the type and evolutionary stage of the nuclear activity.

The first detection of the molecule with carbon detected in the interstellar medium was methylidine radical (CH) in 1937 and was discover by Swings and Rosenfelds, later McKellar, A. in 1940, Walter Adams in 1941 from Mount Wilson Observatory, a radio detection was doing by Rydbeck et al 1974.

1.2 Goals

The main goal of the thesis is to study the chemical complexity and the physical conditions of the molecular gas in three galaxies with different type of activity, in our sample we have a pure starburst (SB) galaxy NGC 253, a AGN with a nuclear starburst NGC 4945 and an UltraLuminous galaxy (ULIRG) Arp220. We present in this thesis the first extragalactic unbiased spectral line survey of the full 345 GHz atmospheric window. The specific goals of the thesis were:

- to carry out a molecular survey of the galaxies NGC 253, NGC 4945 and Arp220.
- to determine the molecular abundance for each of the above mentioned galaxies.

- to detect new molecules in the extragalactic medium.
- to compare the molecular astrochemistry of the three galaxies at different frequencies.
- to draw conclusions on the effects of the nuclear activity in galaxies in the physical condition of the molecular clouds and the chemistry.

This study has been carried out with the APEX telescope and data from Herschel.

1.3 Activity in Galaxies

1.3.1 Active galactic nuclei

Active Galactic Nuclei (AGN) are powerful sources located in the central regions of some galaxies. The possibility of observing both the AGN and the host galaxy depends on the contrast between the luminosities of both components, which in turn varies from object to object and is related to the wavelength at which it is observed.

One of the main characteristics of AGN is that they emit a large quantity of energy in all the spectral ranges. This energy is released inside a very small volume and cannot be attributed only to stellar processes. AGN are among the most luminous objects in the sky with luminosities ranging from 10^{42} to10^{48} erg/s. The spectrum of the galaxies hosting active nuclei is very different from those of normal galaxies. (See Fig. 1.1). Observed in it are prominent emission lines such as, MgII, FeII, Paβ, etc. Also some of these objects show variability and some degree of polarization. Luminosity variations may occur at intervals of hours, days or years (Ulrich et al. 1997). There is a strong correlation between the variability seen in the optical, IR and gamma spectral ranges, but there is no correlation with that observed at radio wavelengths (Villicaña (2010)). In the optical spectra of some of these objects very wide emission lines are observed that indicate that the gas producing them is experiencing motions of several thousands of km/s.

Is thought that the AGN host a supermassive black hole in their centers (more than a million solar masses concentrated in a volume smaller than the orbit of the Earth). The material that is falling toward the central black hole spins around it at high speed, causing the heating of particles to temperatures of millions of degrees. This so called accretion disk has an associated corona of electrons that reprocesses the UV radiation from the disk and, by inverse Compton effect, emits X ray radiation. The presence of this corona may be due to fulgurations, consequence of the twisted magnetic lines. A relevant fraction (approximately 50 percent) of the X rays generated in the corona suffer reflection in the disk itself generating the fluorescent lines of the iron (Fe) and photoelectric absorption, with the efficiency of the reflection determining the final shape of the X ray spectrum. For a black hole mass of 10^5-10^3 Mo$\odot$, the accretion disk is heated to 10^5-10^6 K, generating a modified Planck spectrum. Finally, the matter falls inside the black hole releasing a large amount of energy in the form of a burst. During this process of accretion the matter can generate jets that emerge at the magnetic poles almost at velocities close to the speed of light that impact on the intergalactic matter.

1.3.2 Observational classification of AGNs

The AGNs are classified in 3 big groups according with their radio emission: Seyfert, where the AGN is, normally, in a well detected spiral galaxy; quasars, in which the nuclear emission dominates that of the host galaxy; BL Lac or blazars wich show weak emission lines. Regarding to its emission at radio wavelengths, AGN are classified as strong and weak radio emitters. From their brightness and morphology, Fanaroff and Riley (1974) distinguished two kinds of strong radio emitters AGN: FRI and FRII. According to their variability, AGN characterized by a fast and violent variability in the optical band are designed as OVV (Optically Violently Variable) . BL Lac, that was originally identified as a variable star, is the prototype of a class of AGN. OVV and BL Lac objects share some properties and are generally denominated Blazars (Ulrich et al. 1997). Most of them reside in elliptical galaxies.

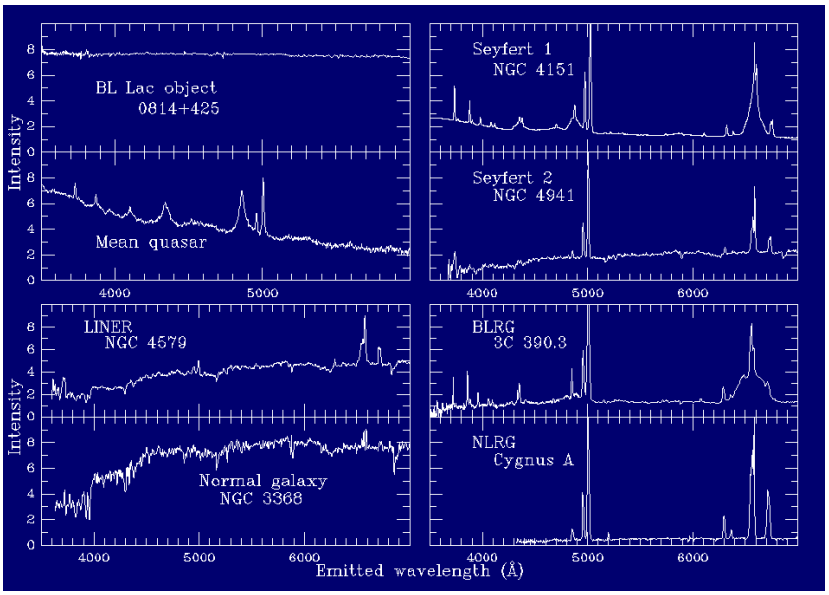

Figure 1.1: Spectral clasification of AGNs.

1.3.3 Standard Model

The standard model postulates the existence of a central black hole that is accreting matter; the matter is spiraling in towards the black hole forming an accretion disk. The friction associated with tidal forces makes that the matter keeps heating more as it jets closer to the center. The loss of kinetic energy causes its orbit to be closer to the black hole. In the regions closest to the black hole, the material is dragged by the magnetic fields generating a high temperature coronal gas. Part of this material is expelled as jets and the rest falls into the black hole. The unified model proposes that the appearance of an AGN depends on the position of the observer with respect to its symmetry axis Antonucci (1993); Urry and Padovani (1995). This is due to the existence of a dust torus with an inner radius of approximately 1 pc that surrounds the black hole and therefore, depending on the position of the observer with respect to the symmetry axis, the torus can hide part of the emission from the innermost region of the accretion disk. According to the unified model, the differences between the spectral characteristics of the different AGN

(see section 1.2) are due to the line of sight crossing or not the torous. The matter in the torus strongly absorbs the light from the central region of the active nucleus.

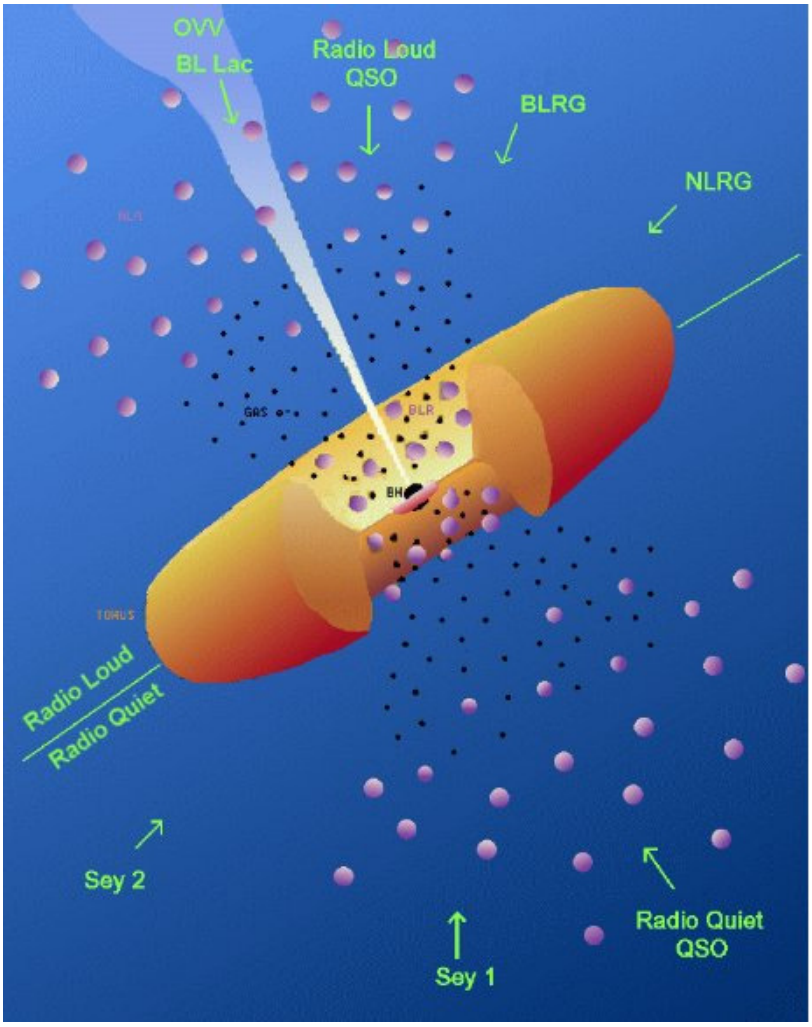

Figure 1.2: Standard Model of AGNs.

The origin of the emission of AGN in the different bands of the observed spectrum are attributed to:

- Radio emission due to jets of electrons. item Infrared irradiation coming from the molecular torus.
- Optical emission from the broad line regions (BLR) and narrow line regions (NLR).
- X ray emission due to the corona of the disk within less than 10 Schwarchild radius.
- Gamma rays emanating from the most interior zone closed to the black hole.

1.3.4 Seyfert galaxies

The Armenian astrophysicist B. Markarian studied in the 60's, in the Byurakán Observatory, galaxies showing an excess of UV emission. These same galaxies were studied in 1943 by Carl

Seyfert who found that some nearby spiral galaxies had a point like bright nucleus. This kind of galaxies was named after him: Seyfert galaxies (Sy). They show an UV excess, their nucleus looks quasi-stellar and show variable emission in time scales of weeks or days. Markarian and coleagues, using the Schmidt cammera in the Byurakan Observatory, catalogued galaxies with continuum spectrua in the UV. In such catalogue, 10% were Seyfert galaxies. This kind of galaxies show different spectra with different line widths. They are split into two main groups: Sy1 and Sy2.

Sy1 galaxies show broad hydrogen recombination lines with linewidths of thousands of km s^{-1} in their central regions. Also, Sy1 are more luminous than Sy2 and their spectra are similar to those of low luminosity QSO. This kind of galaxy, show FWHM for the HI, HeI and HeII lines of 1-5 x 10 ^{3} km s^{-1} , while forbidden lines such as [OIII]$\lambda\lambda$4959, 5007 Å, [NII]$\lambda\lambda$ 6548, 6583 Å and [SII]$\lambda\lambda$ 6716, 6731 Å have a FWHM of 5x10^2 km s^{-1} (E. Khachikian and D.W. Weedman). An example of Seyfert 1 is NGC 3227

In contrast to Sy1 galaxies, the spectra of Sy2 show only narrow emission lines. A 2% of spiral galaxies contain a Sy2 nucleus.

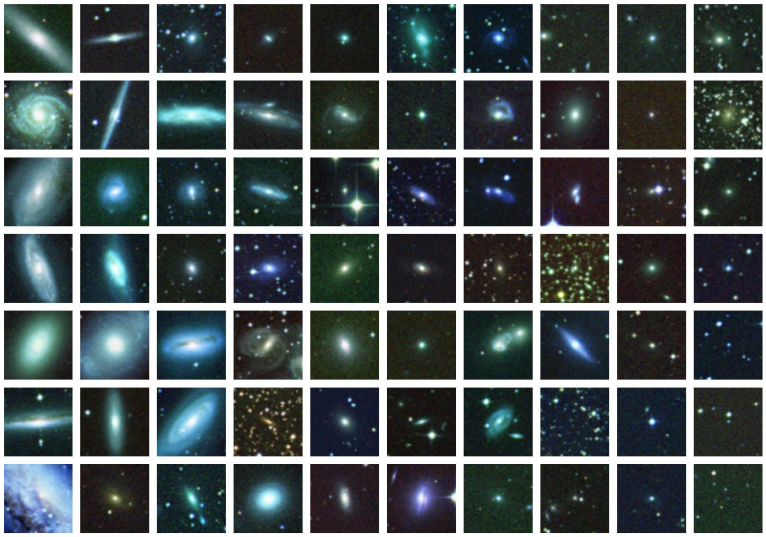

Figure 1.3: Typical Seyfert galaxies. The individual images are taken from Palomar Digital Sky Survey. Source: swift.gsfc.nasa.gov

1.3.5 Starburst galaxies

The name starburst was used for the first time by Weedman et al. (1981) in his study of the nucleus of the galaxy NGC 7714 in account of its large luminosity. Studies of two color diagrams (U-B vs B-V) by Larson y Tinsley (1978) had already shown that galaxies of a similar kind exhibited a special morphology (interaction of galaxies) and bluer colors aand higher dispersion. This was interpreted as a consequence of different star formation rates for galaxies with different

colors, suggesting recently stellar formation phenomena for the bluer ones. Thus, this study was the first proof of the relation between the starburst phenomenon in galaxies and the interaction between them. The growth in the luminosity due to a star formation burst inside a galaxy nucleus is difficult to detect because newly formed stars are inside gas and dust clouds with high opacity to the radiation from the optical to the UV arising from them.

This kind of galaxies are extremely glowing at the infrared, emitting around 98% of their energy in this spectral range compared with non active galaxies such as the Milky Way, which emit about 30% of its luminosity in the IR (Carroll and Ostlie, 1996).
Starburst nuclei and active galaxies harbour large masses of molecular gas and dust in their interior. This molecular gas is closely linked to the feeding of the nuclear activity and therefore plays an important role in the evolution of the galaxy. Observations of the molecular gas properties help us to identify and analyze the type of activity in very deeply obscured galactic nuclei. Line ratios between molecular species may also help to determine the physical conditions and chemistry of the gas, which could potentially help us to know the type and evolutionary stage of the nuclear activity.

1.3.6 ULIRGs

There is yet other kind of active galaxies, known as Ultra Luminous Infrared Galaxies (ULIRG) with super starbursts. ULIRG, were found for the first time in a study of interactions and mergers between galaxies, (Joseph and Wright 1985). Such objects are evolved mergers with a double nucleus (Carico et al. 1990; Mazzarella et al.1992; Majewski et al. 1993). These merging galaxies are two orders of magnitude more luminous than bright spiral galaxies, and one order of magnitude more luminous than typical nearby starbusts.The survey carried out by IRAS showed that starbursts can be a common phenomena in galaxy evolution and that the luminosity of this kind of galaxies are larger than $10^{12}L_o$
ULIRG do not show evidence for a compact central non thermal source, and their emission can be explained solely by star formation (Gehrz et al. 1983).

1.3.7 Conditions leading to a starburst

Diverse physical conditions can lead to a burst of star formation. To explain how the matter is transported from the disk of the galaxy to the nuclear region where the activity is taking place it is necessary to find the mechanisms by which the gas may lose angular momentum. These aremainly two:

- BARS: The gravitational transport, in which the matter looses the angular momentum by friction and shocks between molecular clouds originated inside a galaxy region with a triaxial gravitational potential produced by a bar. There is observational evidence that shows bars to be the reason for the large concentration of gas in the galaxy nucleus (Sakamoto

et al.,1999; Sheth et al., 2002). Also, there are observational proofs of the existence of starbursts located in host barred galaxies (Huang et al., 1996).

- INTERACTIONS: Interactions between galaxies can also contribute to release angular momentum and to trigger the flux of material to feed the starburst (e.g. Shlosman et al., 1989, 1990; Mihos and Hernquist, 1996). ULIRG nuclei show intense star formation (Genzel et al., 1998), and are associated with galaxies affected by strong interactions (Joseph and Wright, 1985; Armus et al., 1987; Sanders et al., 1988; Clements et al., 1996; Murphy et al.,1996; Sanders and Mirabel, 1996).

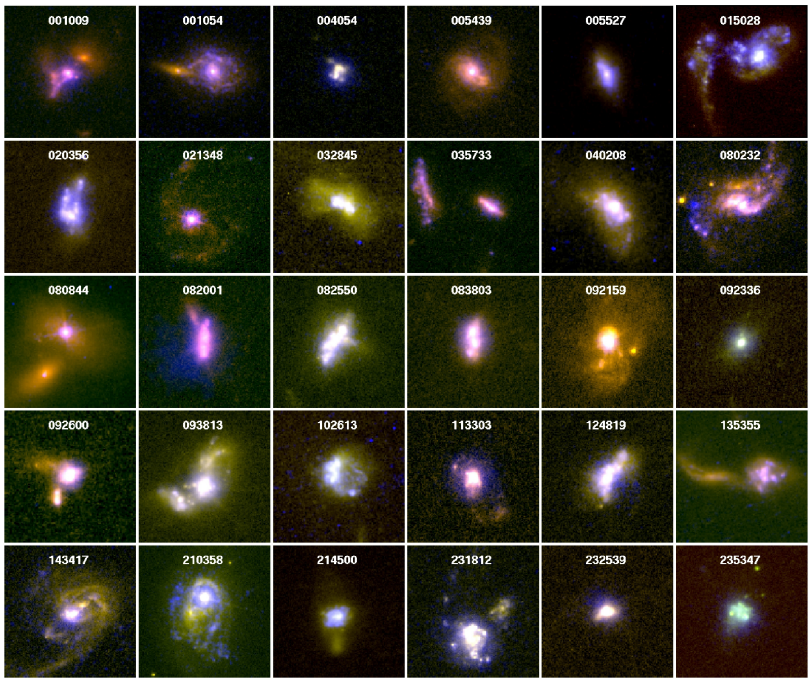

Figure 1.4: False color HST images of the nearby starburst sample showing (rest frame) the UV in blue-purple and optical light in yellow-red. Source: mpa-garhing.mp.de

1.4 Source selection and properties of the sample

The physical properties in the nuclei of the closest galaxies are measured best at sub-millimeter wavelengths, where a rich spectrum of dust continuum an molecular lines allows us to trace the star forming molecular material. In this thesis we will study in detail a sample of three nearby galaxies selected for showing different types of activity: NGC 4945, a starburst with an AGN (Wang et al. 2004); NGC 253, a pure starburst; and the ULIRG Arp220. These sources are the brightest extragalactic infrared and submillimeter galaxies; NGC 253 and NGC 4945 are the closest starbursts and Arp 220 is the nearest ULIRG.

1.4.1 NGC 253

The nuclear starburst galaxy NGC 253, classified as SAB(s)c (de Vaucouleurs et al., 1991) o Sc(s) (Sandage and Tamman, 1987), is one of the brightest extragalactic molecular line sources. At a distance of 3 Mpc in the Sculptor constelation, most of its overall IR luminosity is originated in the regions of intense massive star formation within its central few hundred parsecs. Martin et al. (2006) carried out a 2mm spectral line survey towards this galaxy.

The emission of NGC 253 had been observed from radio to gamma rays (Paglione et al., 1996; Domingo-Santamaria and Torres, 2005). Optical images of this galaxy show spiral arms and a luminous galactic disk (e.g. Pence, 1981) which is observable with high resolution in HI maps (Koribalski et al., 1995).

The FIR luminosity of the galaxy is at least two times larger than that of Galaxy (Cox and Mezger, 1989; Dudley and Wynn-Williams, 1999) and its analysis allows the derivation of the dust temperature of 41K (Negishi et al., 2001). The nucleus of NGC 253 has the second most intense IR extragalactic source in the IRAS catalog, after M82, with a flux at 100 micras of 1860 Jy (Soifer et al., 1989); 70 percent of this luminosity comes from intense massive star formation within a few parsecs. The derived star formation rate (SFR) is 3.6 M$\odot$year$^{(}-1$)(Strickland et al. (2004)).

Observations in the near IR (K,H,J bands) show a prominent bar (Scoville et al., 1985; Forbes et al., 1991; Forbes and DePoy, 1992; Fouque and Bertin, 1995; Engelbracht et al., 1998). Aladro et al. (2011) compared the 3mm and 2mm molecular line survey. Warren et al. (2014) reported, using ALMA, that NGC 253 would exhaust its nuclear star forming gas in 60 to 120 Myr at its current mass loss rate (9 solar M$\odot$/yr).

1.4.2 NGC 4945

NGC 4945, is a nearby edge-on spiral starburst galaxy with a systemic velocity of 563 km/s (Ott et al. 2011). It is one of the three brightest IRAS point sources (686 Jy) beyond the Magellanic clouds. NGC 4945 contains a highly obscured compton thick Seyfert 2 nucleus (e.g. Maiolino et al. 1999) and has been classified as SB(s)cd or SAB(s)cd. It is a member of the Centaurus group, at a distance of 4 Mpc (Bergman et al. 1992, Wang et al. 2004). Wang et al. 2004, studied the environment in NGC 4945 detecting molecules at 3mm, 2mm and 1.3mm.

Numerous studies from radio to hard X-ray wavelenghts have been carried out towards this prominent southern galaxy. It is a strong radio continuum source with a flux of 4.8 Jy (Whiteoak and Bunton, 1985; Ott et al. 2001) and contains the first known megamaser (Dos Santos and Lepine 1979; Batchelor et al. 1982), detected at 22 GHz. Studies of molecular lines were published by Whiteoak and Gardner (1975), Whiteoak and Wilson (1990), Henkel et al. (1990) and Curran et al. (2001). An edge-on nuclear gas ring with a size of 30" was discovered by

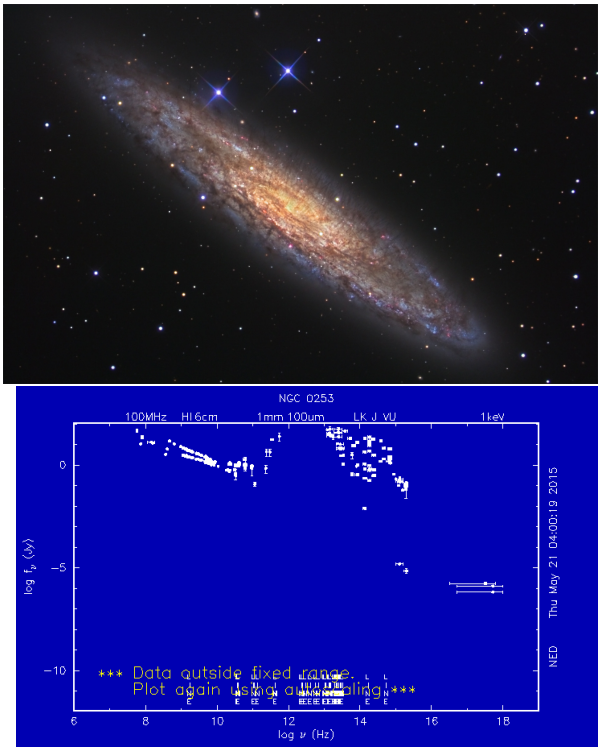

Figure 1.5: Image and SED of NGC 253. Source: Nasa Extragalactic Database: https://ned.ipac.caltech.edu/

Whiteoak et al. (1990) in the transition J=1–0 of CO and $^{(}13)$CO (Bergman et al. (1992). Dahlem et al. (1993) and Mauersberger et al. (1996a) confirmed the presence of this ring. X-ray observations reveal a complex morphology including a strong variable nuclear source at 2–10 keV and a conically shaped 'plume' at 0.3–2 keV (Schurch et al. 2002).

1.4.3 Arp 220

Arp 220 is the closest (z=0.018, d=72 Mpc) ultraluminous infrared galaxy (ULIRG). Arp 220 has a double nuclei observed at radio (Norris et al. 1988), mm (Scoville et al. 1997, Downes et al. 1998, Sakamoto et al.1999), and sub-mm (Sakamoto et al. 2008) wavelengths. Martin et al. (2011) carried out a line survey of this ULIRG using the Submillimeter Array. Arp 220, at 1.3mm, shows an intense starburst, probably triggered by dense and massive galactic merger (Soifer et al. 1984; McDowell et al. 2003). This galaxy has a rotating disk orbiting within a much larger gas disk, potentially with an extended galactic halo (Sakamoto et al. 1999, González et al. 2004). ARP 220 has three distinct stellar populations: a 10 Myr old starburst, a 1 Gyr old population and an emerging 7 Myr old non-starburst component (Engel et al. 2011). Also, Tunnard et al. (2015) showed that the gas traced by SiO(6 to 5) has a complex and extended kinematic signature including a prominent P Cygni profile implying a bipolar outflow. Aladro et al. (2015), studied the most extensive line survey at 3 mm of eight nearby active galaxies including ARP 220.

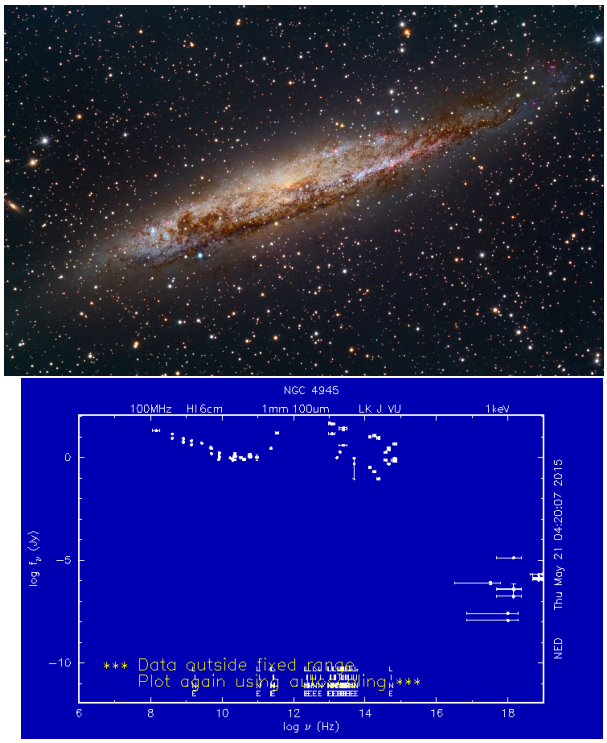

Figure 1.6: Image and SED of NGC 4945. Source: Nasa Extragalactic Database: https://ned.ipac.caltech.edu/

1.5 Extragalactic Astrochemistry

The molecular emission from the central regions of active galaxies is a powerfull tool to understand the physical processes that give rise to the nuclear activity. The study of key molecular tracers and their abundance ratios can be used to establish if the dominant heating mechanism is due to shocks, photodisociation regions (PDR) or X-ray dominated regions (XDRs). Shocks, UV radiation, X rays and cosmic rays play an important rol in the chemistry of molecular clouds in the nuclei of galaxies.

1.5.1 Molecule formation in the ISM

The formation of molecules in the Interstellar medium is possible under the condition of high densities in a given region as the consequence of the occurrence of collisions between atoms. Moreover, a molecule can be dissociated by an UV photon. Interestelar dust can act as a protection against dissociation since it will absorb any UV radiation. Hence the combination of a high particle density and the presence dust grains help the production and maintenence of molecules that are in the dense and cold regions of the Interstellar medium, i.e. the molecular clouds. The photodisociation of the molecular gas by UV fields (PDRs regions) is produced by the emision of OB star groups formed in the starburst.

The basic mechanism of molecular formation in the Interstellar medium is the occurrence of reactions in which one of the particles involved is charged; these are named ion-molecule reactions. This kind of reactions can be produced because in the molecular clouds there are ions, due to cosmic rays inside the molecular cloud. The ion charges exert an atractive force over

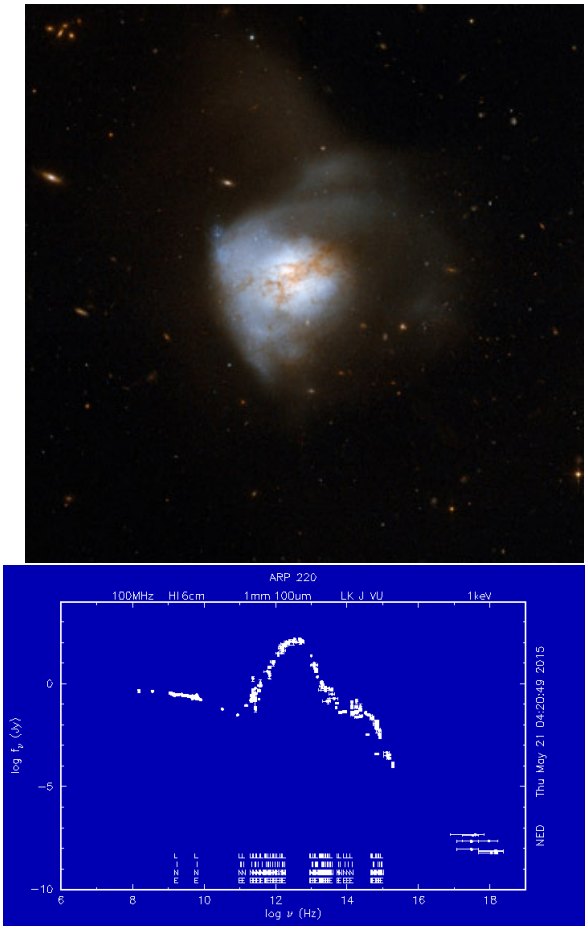

Figure 1.7: Image and SED of Arp 220. Source: Nasa Extragalactic Database: https://ned.ipac.caltech.edu/

the electron cloud of the molecules that helps to the reaction production. The formation of hydrogen molecules takes place in reactions on the surface of dust grains which act as catalysts of the reaction and absorb the excess of free energy during the formation of the H_2 molecule. A hydrogen atom can experience a collision with a dust grain attaching itself onto the grain surface where it can wait for a second H atom, thus forming a H_2. The excess of energy will free the new molecule and convert it to gaseous state.

The structure of a giant molecular cloud (see Fig. 1.8), shows the change from the ISM (very low densities and temperatures of the order of 25K) to the hot regions aroung a young stellar object (YSO). Simple neutral atoms- HI state- are in the outer regions; towards the centre of the cloud the molecular density, temperature and dust particle numbers rise, some of them form ice layer surfaces and are covered by radiation from th stars transforming the molecules on the icy surface. H atoms combine on the surface of dust particles and form H_2 faster than the gas phase recombination reaction takes place. The location of hot young stars are the HII regions where the intense radiation field from the stars is sufficient to remove the electrons from H atoms and a new emission process is observed.

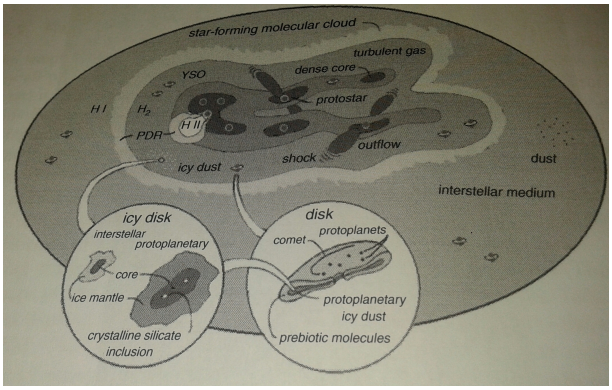

Figure 1.8: Molecular cloud

The gaseous component

The molecular Hydrogen (H_2) is the most abundant molecule in the universe. In the Galaxy H_2 is found in cloud complexes with masses of more than 10^6 M$\odot$. The cloud mass is composed of 63% of H_2, 36% of He and 1% of other atoms.

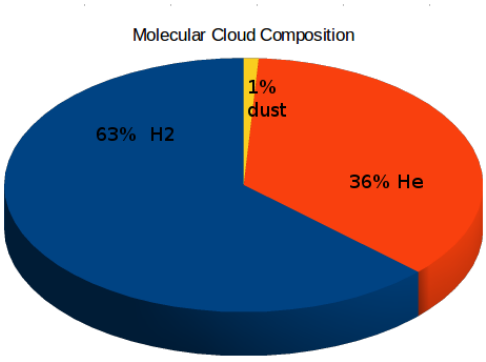

Figure 1.9: Gaseous component

The production of H_2 must occur on dust grains. Grain surfaces act as catalysts for the conversion of H into H_2. The H_2 molecule is dissociated by 11eV photons with the emission of spectral lines. The minimum H_2 column density is 10^{20}cm^{-2}, i.e. corresponding to a visual extinction of Aν=0.1^m. H_2 emission is difficult to observe because of the lack of dipole moment due to its symmetry. The density required to excite it varies over a wide range, from 10^2cm^{-3} to 10^7cm^{-3}.

Most of the clouds have supersonic molecular linewidths, except for the densest cores of dark clouds. Supersonic turbulence in clouds is widespread. It could be due to the outflow of material from embedded objects, such as newly born stars, or to large scale organized motions, such as galactic rotation which converts the kinetic energy into smaller scale turbulence.

Interstellar dust

About 1% of the mass of molecular clouds is in grains. There is one dust grain for every 10^{12} H_2 molecules. The dust is mostly composed of of carbon and/or silicon. The **polycyclic aromatic**

hydrocarbons or PAHs are molecules containing from 20 to 50 carbon atoms or a combination of carbon and hydrogen.

There are strong interactions between dust grains and gas phase molecules, hence there will be a molecule-grain collisions in a time given by the following expression, for a temperature, T_K, of 100K, and a density, $n(H_2)$, of 1 cm^{-3}.

$$t_{mg} = \frac{3x10^9}{n(H_2)} \text{ years}$$

These collisions generate icy mantles of carbon monoxide, water and methanol around dust grains in high extinction regions with densities of higher than 10^4 cm^{-3}. The mantle material could be returned to the gas phase by evaporation or shock waves. Strong shocks can break the grains, and it is thought that the presence of SiO in the gas phase is an indicator of the presence of such shocks.

Inside the clouds, the molecules can survive at radiation, and ions are produced by cosmic rays which can penetrate into the interior of a molecular cloud. The presence of complex molecular species that contain carbon such as formaldehyde H_2CO, cyanoacetylene C_3HN, formamide NH_2CHO and ethyl alcohol CH_3CH_2OH are considered excellent tracers of dust grain chemistry.

1.6 Tracers

In this section we introduce the most common molecular tracers obtained from the literature. Also, using the multiline analysis combining this survey at 1mm with surveys at 1.3mm, 2mm and 3mm it is possible to determine the physical conditions inside clouds, such as densities and abundances.

- Total column densities of molecular gas and kinetic temperature as traced by CO emision and its isotopologues.
- Clear photo-dissociated regions, the edge of the molecular clouds dissociated by OB stars (Martin et al. 2009) of PDR are traced by HOC^+ , CO^+ , HCO and c-C_3H_2. Such molecules are formed by ion-molecule reactions in gas phase (Hollis et al. 1983, Thaddeus et al. 1985).
- Enhanced CN and HCN abundance could be produced in the X-ray and UV field dominated regions expected in AGN and starburst galaxies (Aalto et al. 2002 and 2008, and Aladro et al. 2015). Henkel et al. 2014 reported that CN appears to be the best tracer to find carbon isotope ratios in the closest external galaxies. Comparison of observations and models confirm that the abundances of CN and HCN also increase in the presence of cosmic ray ionisation and X-rays that are predominant in AGNs (Aladro et al. 2015).
- The presence of lower energetic radiation wipe out heavy complex organic molecules, for example, methanol (CH_3OH) and Isocyanic acid (HNCO) (Martin et al. 2006, Martin et

al. 2008). The products of photo-dissociation can drive ion-molecule reactions (Savage et al. 2004, Martin et al. 2009, Aladro et al. 2011).

- HNCO could also be a good indicator of the evolution of nuclear starbursts in galaxies, with abundances decreasing towards the last evolutionary stages of the starburst.

- CH_3C_2H was found to be very abundant in regions with active star formation (Churchwell and Hollis 1983, Miettinen et al. 2006), with abundances higher than those found in dark clouds (Irvine et al. 1981, Markwick et al. 2005). The emission of CH_3C_2H has asimilar morphology to that of C_2H, consistent with the PDR tracers (Meier et al. 2015) and the tracers of dense gas.

- CH_3CN and SiO are tracers of dense gas and shocks. The increase of SiO abundances can be related to X-ray chemistry in AGNs (Garcia-Burillo et al. 2010, Aladro et al. 2013). Also, SiO is a tracer of cosmic rays in the center of the Milky Way and NGC 1068 (Martín-Pintado et al. 2000, Usero et al. 2004, Aladro et al.2013)

- H_3O^+ (hydronium) is a molecular ion with its fundamental transitions in the submillimeter band. The high proton affinity of water makes hydronium a key ion in the oxygen chemistry of dense molecular clouds and can be used to estimate the ionization degree in molecular clouds (Phillips et al. 1992). Observations of the H_3O^+ emission help us to probe the location of dense and warm gas in galactic nuclei, which combined with the H_2O abundance, may be used to trace the ionization rate by cosmic rays from supernovae, starbursts and/or X-rays from an AGN.

- H_2S can be interpreted as a tracer of very early stages of bursts of star formation (Martin et al. 2010 and Hatchell et al. 1998).

- HC_3N is likely tracing the hot cores associated with the massive star formation sites within the nuclear region of a galaxy host (Martin et al. 2010).

- High density tracer molecules like NH_3, CS, HCO^+.

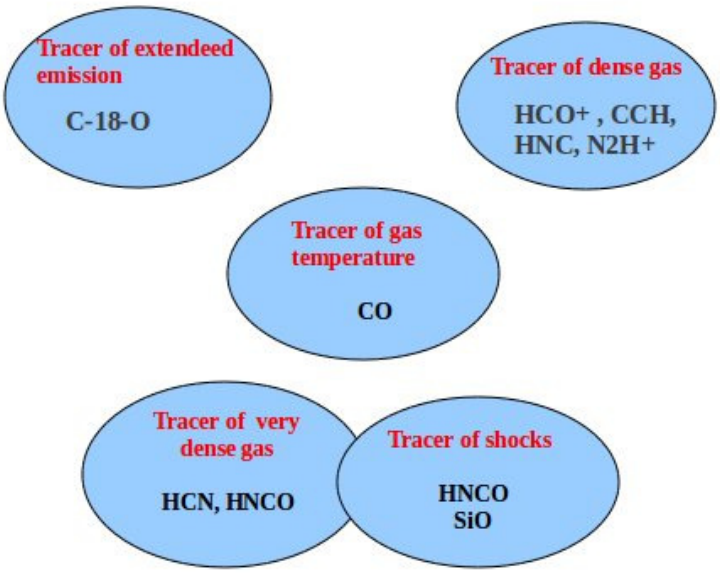

Figure 1.10: Molecular important tracers.

Chapter

2

Observations and Data reduction

2.1 Observations

This section reviews the instruments that were used to carry out the work presented in this thesis.
Main observations were obtained with the APEX telescope using the 345 GHz band of the FLASH receiver (Heyminck et al. 2006). Also, public data from Hershel telescope were used. A brief description of the observations follows.

- Line surveys toward NGC 253, NGC 4945 and Arp220 were obtained over several runs in April, July and November 2010.
- Additional bservations at ν= 307.1924 GHz, ν= 364.7974 GHz, ν= 388.458 GHz para-transitions and ν=396.272 GHz ortho transition of H_3O^+ were obtained in August 2014 towards NGC 253.
- A single observation at ν= 296GHz of the $HCNH^+$ molecule was obtained in September 2014.
- Data from the public archive of the Hershel telescope for transitions at ν= 984711.9070 (ID code 1342210669) and ν=1655248.3850 (ID code 1342212182) for H_3O^+ lines were used.

A description of the instruments as well as details of the observations is presented in the next sections.

2.1.1 APEX Telescope

The APEX (Atacama Pathfinder Experiment; http://www.apex-telescope.org) is a 12m telescope (see fig 1.1) built and operated by a collaboration between Max Planck Institut für Radioastronomie (MPIfR) at 50%, Onsala Space Observatory (OSO) at 23%, and the European

Southern Observatory (ESO) at 27% . APEX is a prototype antenna used as a single dish telescope installed on the high altitude site of Llano Chajnantor, the site of ALMA.

Figure 2.1: APEX telescope over Llano Chajnantor.

We used the PI instrument of the MPIfR (Rolf Guesten), Flash operating as a dual frequency receiver simultaneously on orthogonal polarizations in the 345GHz and the 460GHz atmospheric windows (See fig 1.2).The receiver has been in operation since June 2004. The 2SB mixer was provided by IRAM (D.Maier et al. 2005). The new version of this receiver, FLASH+, now provides continuous sky frequency coverage from 268 to 516 GHz. Since this last upgrade the receiver is operated remote-controlled and tuning is fully automatic. The trasmision (Y axis) has values between 0 and 1.0; such values mean that at 0 the atmosphere is completely opaque, while 1 mean that the atmosphere is clear. The precipitable water vapour is marked in color: the black line corresponds to pwv=0.5, the red line to pwv=1.0, and the blue line pwv=2.0.

Details of the observations

The sideband separating mixer allows to observe 8 GHz instantaneous bandwidths to cover the whole frequency range between 270 GHz and 370 GHz. In our surveys the receiver was turned in blocks of 3.6GHz (see Fig. 1.4) to overlap the 4 GHz bands analyzed by the autocorrelator. Observing mode was doing, that mean that the data was observed by the staff of the telescope. The information regarding calibration procedures is contained in the section concerning data reduction.

The central positions used for the observations are shown in table 1.1.

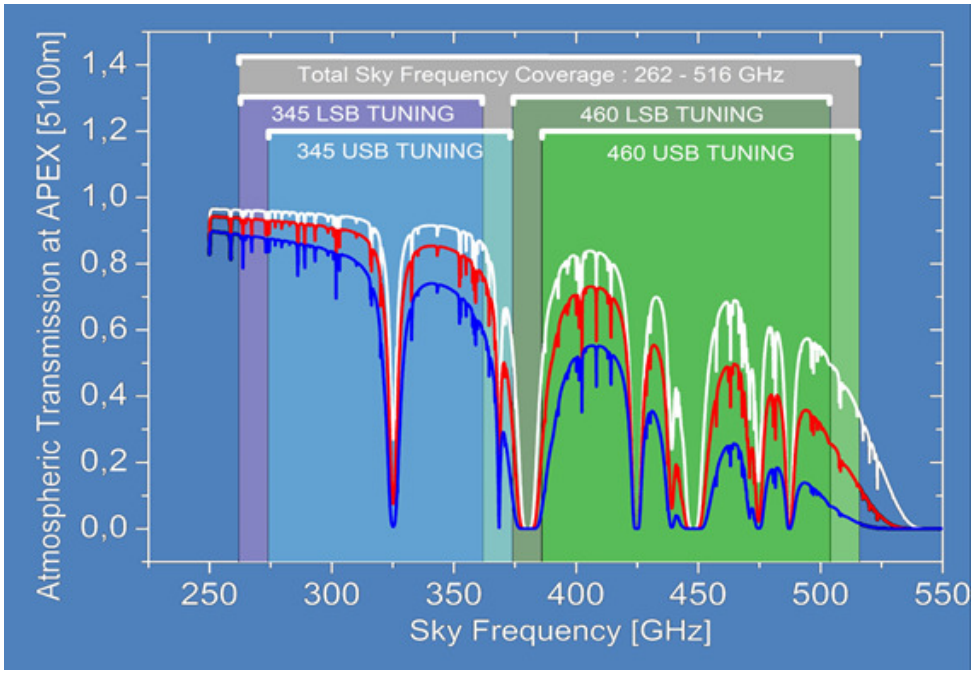

Figure 2.2: The large RF tuning ranges of the FLASH+ channels, the wide IF (intermediate frequency) bandwidths of 4x 4 GHz when both mixers are operated in parallel are perfectly suited for efficient line surveys in these atmospheric windows. Its excellent stability figures have been utilized for numerous line mapping projects, but also for (extragalactic) studies of weak broad lines. source: www3.mpifr-bonn.mpg.de/div/submmtech/heterodyne/flashplus/flashmain.html

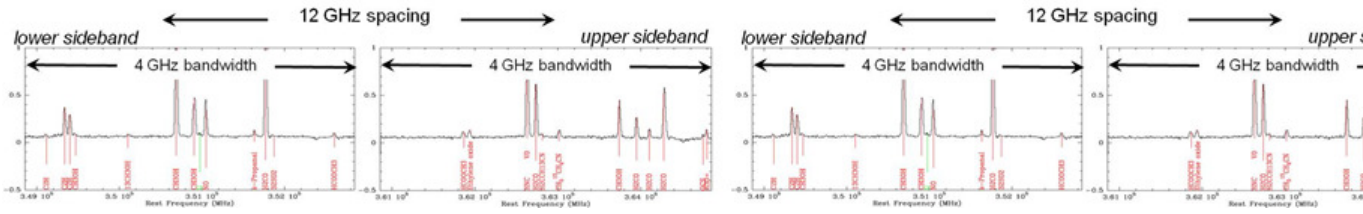

Figure 2.3: A bandwidth of 4 GHz bands in lower sideband, 4 GHz for upper side band are processed simultaneously.

Table 2.1: Galaxy coordinates and radial velocities. Data from SIMBAD and NED. For information about source size see 3.1 section.

Source	Eq Coordinates(J2000) AR(h:m:s); DEC(^{o},‘,”)	Observed position AR(h:m:s); DEC(^{o},‘,”)	VLSR km/s
NGC 253	00:47:33.1 ; -25:17:18.60	00:47:32:98 ; -25:17:15.9	250
NGC 4945	13:05:27.5 ; -49:28:06	13:05:27.47 ; -49:28:05.5	560
Arp 220	15:34:57.8 ; 23:30:11:30	15:34:57.21 ; 23:30:09.5	5434

2.1.2 Hershel and HIFI

The European Space Agency’s Herschel Space Observatory (in the past Far Infrared and Submillimetre Telescope or FIRST) has the largest single mirror ever built for a space telescope.

With a 3.5m in diameter this telescope collected far-infrared and sub-millimter radiation from some of the coldest and most distant objects in the universe. Herschel is the only space observatory so far to cover a spectral range from the far infrared to sub-millimetre.

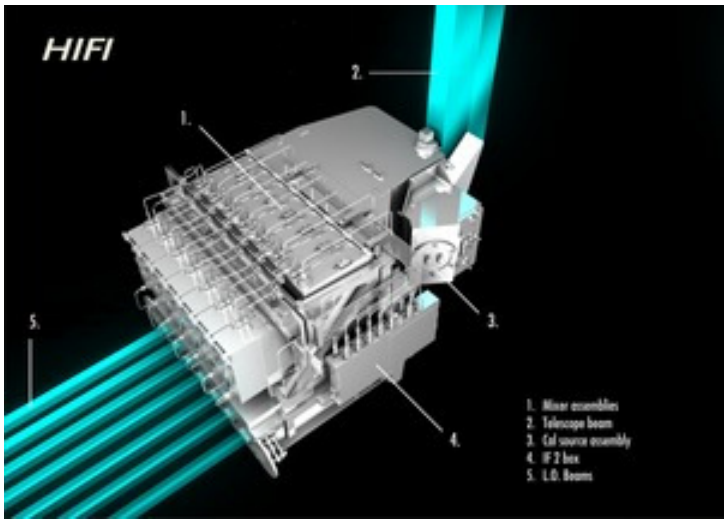

Figure 2.4: HIFI image

The telescope focuses the light onto three instruments: PACS (Photodetector Array Camera and Spectrometer) and SPIRE (Spectral and Photometric Imaging Receiver), which each containing a photometer and a low-to-medium resolution spectrometer, and HIFI (Heterodyne Instrument for the Far Infrared), an extremely high-resolution heterodyne spectrometer. These three instruments were designed to complement each other. SPIRE and PACS have imaging spectrometers that provide spatial information, while HIFI resolves lines with very high resolution, with only one beam on the sky. Together, HIFI, PACS and SPIRE are capable of detecting light from 57-670 μm.

HIFI is a very high resolution heterodyne spectrometer covering the 490-1250 GHz and 1410-1910 GHz bands, corresponding to about 157-625μm) (see Fig. 1.6). It utilises low noise detectors using superconductor-insulator-superconductor (SIS) and hot electron bolometer (HEB) mixers. There are four HIFI backends to carry out the spectral analysis: two Wide-Band acousto-optical Spectrometers (WBS) and two High Resolution autocorrelation Spectrometers (HRS). One of each spectrometer type is available for each vertical and horizontal polarization. All spectrometers can be used either individually or in parallel.
The heterodyne detection principle involves down conversion of the frequency range of the astronomical signal being observed at a lower frequency (known as intermediate frequency, IF) where it is easier to perform the high spectral resolution analisys by the backends. This is done by mixing the incoming signal with a very stable monochromatic signal, generated by a local oscillator, and extracting the difference frequency for further processing. HIFI observes in seven bands covering 480 to 1910 GHz (see Fig. 1.6), or the wavelength range 157-625 μm. Bands one to five, which give continuous coverage from 480 to 1250 GHz, use superconductor-insulator-superconductor (SIS) mixers. Bands six low and six high cover 1410 to 1910 GHz and use hot

electron bolometer (HEB) mixers.
For more references see http://www.herschel.caltech.edu/page/instruments.

2.2 Data reduction

APEX data were initially reduced and calibrated using GILDAS/CLASS software and converted from antenna temperature (TA*) to T_{MB}. We used the main-beam efficiency factor of 0.67 and a forward efficiency (f_{eff}) of the telescope of 0.95, thus we used the relation T_{MB}= f_{eff} /b_{eff}) TA. CLASS has also been used in this work to subtract baselines (mathematical details in Apendix A) from the observed spectra; baselines of order 1 were substracted in all spectra final. The achieved rms was 6.41mK for NGC 253, 6.75mK for NGC 4945, and 4.45mK for ARP 220 across the spectra for a velocity resolution of 10.57km/s. Due to the broad line widths of the molecular lines and the weakness of the emission, the data towards Arp 220 were smoothed to 60 kms^{-1} (with a rms of 3.43mk)
.
The Herschel Science Archive (HSA) was used to obtain the public data from HIFI necessary to complement our study. Examples of the publicly available spectra towards NGC253 can be seen in Fig. 2.5.

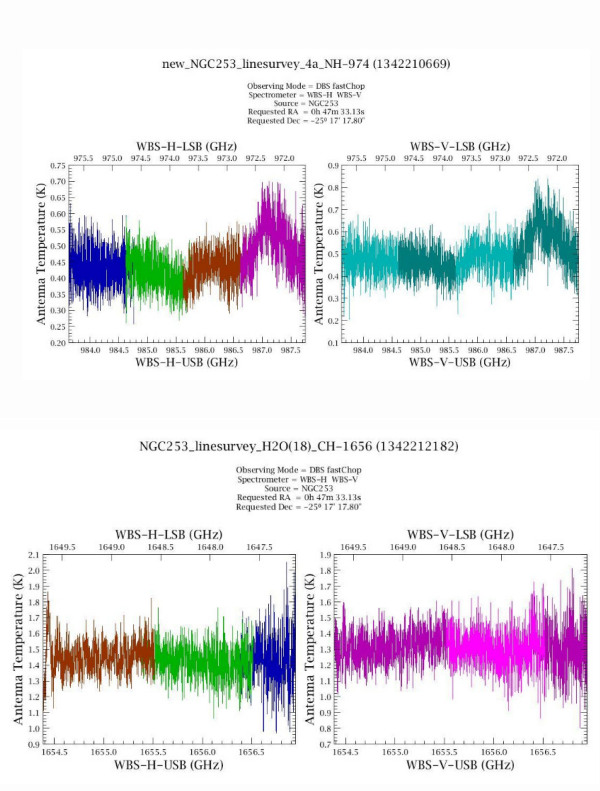

Figure 2.5: Images of the molecule of H_3O^+ toward NGC 253: Top image line at 984711.9070 MHz and correspond to the id code 1342210669; Bottom: Line at 1655248.3850 MHz with id 1342212182. Source: Hershel Science Archive.

Chapter

3

Data analisys

Our data were corrected for beam dilution using the galaxy source size, the beam size and the first source average brightness temperature with the software MADCUBA IJ.

3.1 MADCUBA IJ

MADCUBA (Madrid Data Cube Analysis) is a graphical tool for the analysis of image cubes. The interactive graphical program allows to visualize, examine, reduce and analyze spectroscopic data obtained with single-dish telescopes and interferometers.
With the data properly calibrated it is possible to average all the original spectra obtained by the spectral windows analyzed by the backend. In order to get such average the original spectra are selected and the task average from functions in MADCUBA Plot Window is used (see Fig.3.1).
In this way, the full average of the APEX data for our sources were obtained. The final results are shown in Fig.3.2.

3.1.1 Line identification

The MADCUBAIJ software was used for the line identification in the spectral scans. Different catalogues, such as the Jet Propulsion Laboratory (JPL) line list, the Cologne Database for Molecular Spectroscopy (CDMS) and Lovas can be used on-line. This allows a targeted search of all the molecules contained in the catalogue to match those observed in a given spectrum, or a targeted search for a certain species (See Figs.3.3 and 3.4). Also we can restrict the search in the catalogue by setting limits to the lower energy level and of the lines strength of selected species.
We used the CDMS and the JPL catalogues to identify molecules in the three spectral surveys presented in this thesis. Usually the search was restricted to lines of low energies (less than 100 cm^{-1}) and large strengths, with the exception of light hydrides like H_3O^+ (see Fig. 3.5).

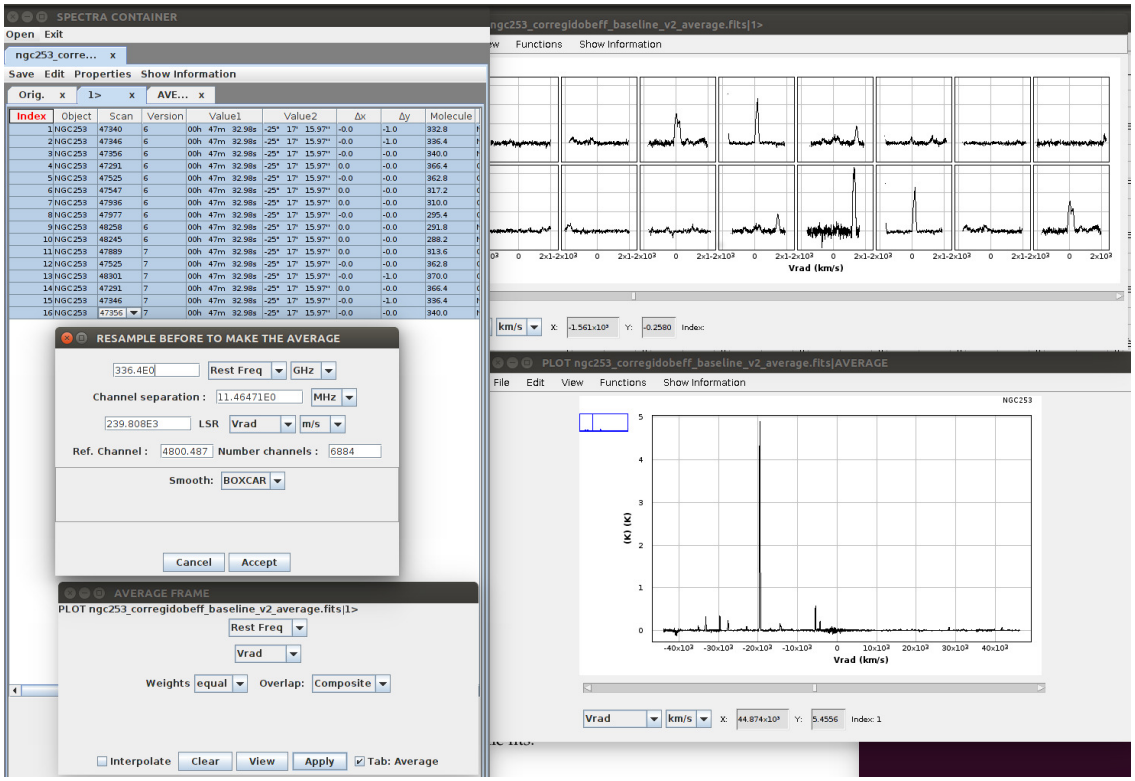

Figure 3.1: The average task. First select all the original subset of partial spectra to be combined in a single full spectra. The task resample the data in the selected spectral axis (velocity or frequency) prepare the resample to get the final average spectra.

3.2 LTE analysis of the line emission

Once one or several lines of a molecule were identified we performed a LTE analysis of its emission. MADCUBAIJ offers two different options for this LTE analysis: Rotational Diagrams (RD; described in detail by Goldsmidth et al. 1999) and the fit of the transfer equation given in Apendix A. Both analyses provide the molecular column density and the excitation temperature if more than one transition is observed. The derived parameters from the Gaussian fit are: Area, FWHM (Full Width at Half Maximum), the observed line profiles derived by Radial Velocity, and also the integrates Intensity.

Using the Gaussian fitting we found the number of velocity component for the most intense lines. For NGC 253, NGC 4945 and Arp 220 we found 2, 3 and 2 velocity components respectively (see Fig. 3.6).

3.2.1 Rotational Diagrams

To derive the RD, we have used the Gauss fit option to obtain the integrated line intensities which can be fitted simultaneously by MADCUBAIJ. As an example of rotational diagrams see Figs. 3.7 and 3.8.

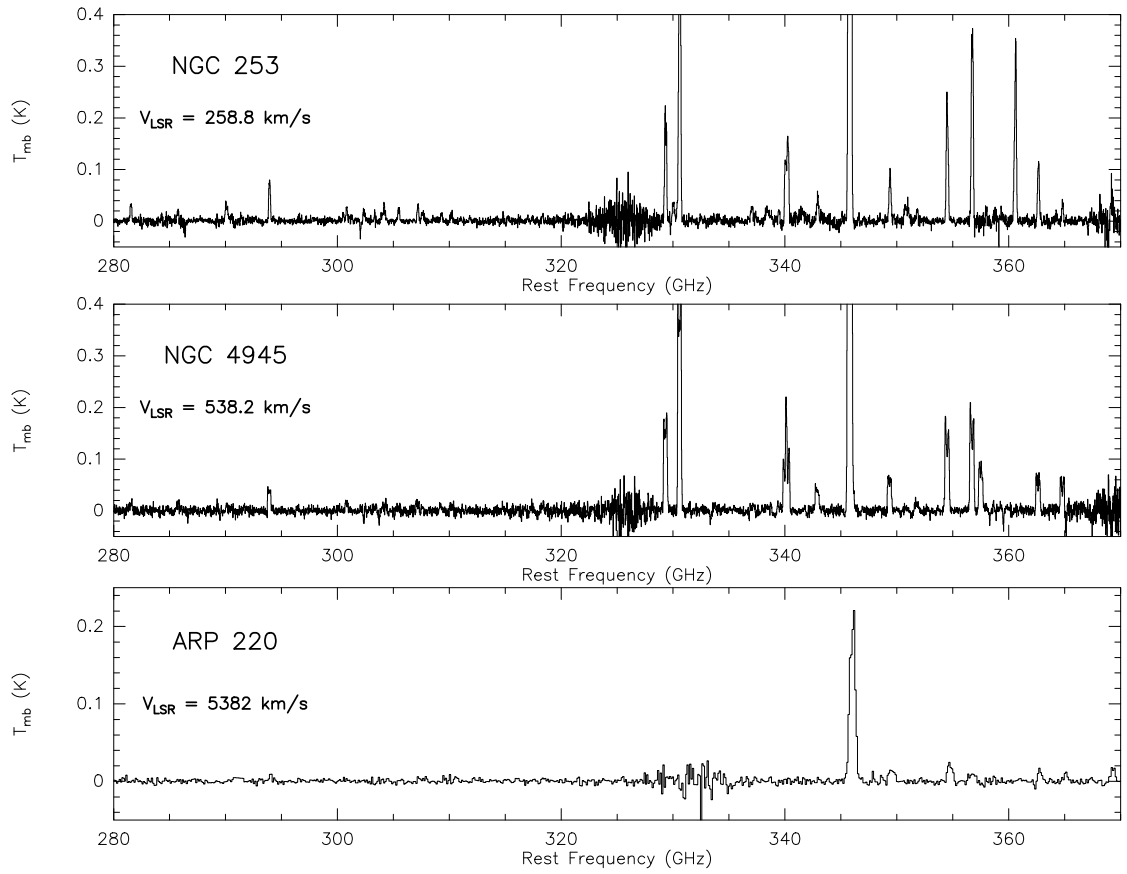

Figure 3.2: Top: NGC 253 averge spectra. Middle: NGC 4945 average spectra. Bottom: Arp 220 average spectra.

3.2.2 Excitation temperatures and molecular column densities

MADCUBAIJ combines the integrated intensities derived from the Gauss fits to generate RD for all species that have more than one transition. From the RD the excitation temperatures and the total column densities can be derived. For the case of NGC 253 we obtained the excitation temperature from the CS molecule using two transitions in our survey. The corresponding derived excitation temperatures were 23(4.2)K and 15(2)K at 163.9 km s^{-1} and 268km s^{-1} respectivelly for each component. Also, for methanol (CH3OH) we have three transitions with low energies clearly detected. Using the methanol lines we derived an excitation temperature of 20K.

In the case of NGC4945 we have also used the data from CS, obtaining 31K, 35K and 48K for each component at velocities of 684.78, 581.643 and 454.137 km s^{-1} respectivelly. In the case of Methanol we derived an average temperature of 20K from the Rotational Diagram since the errors were large.

The lack of more than one line clearly detected for Arp 220 prevented us from determinig the excitation temperature. In this case, we used a value of 15K obtained by Martin et al.(2011)

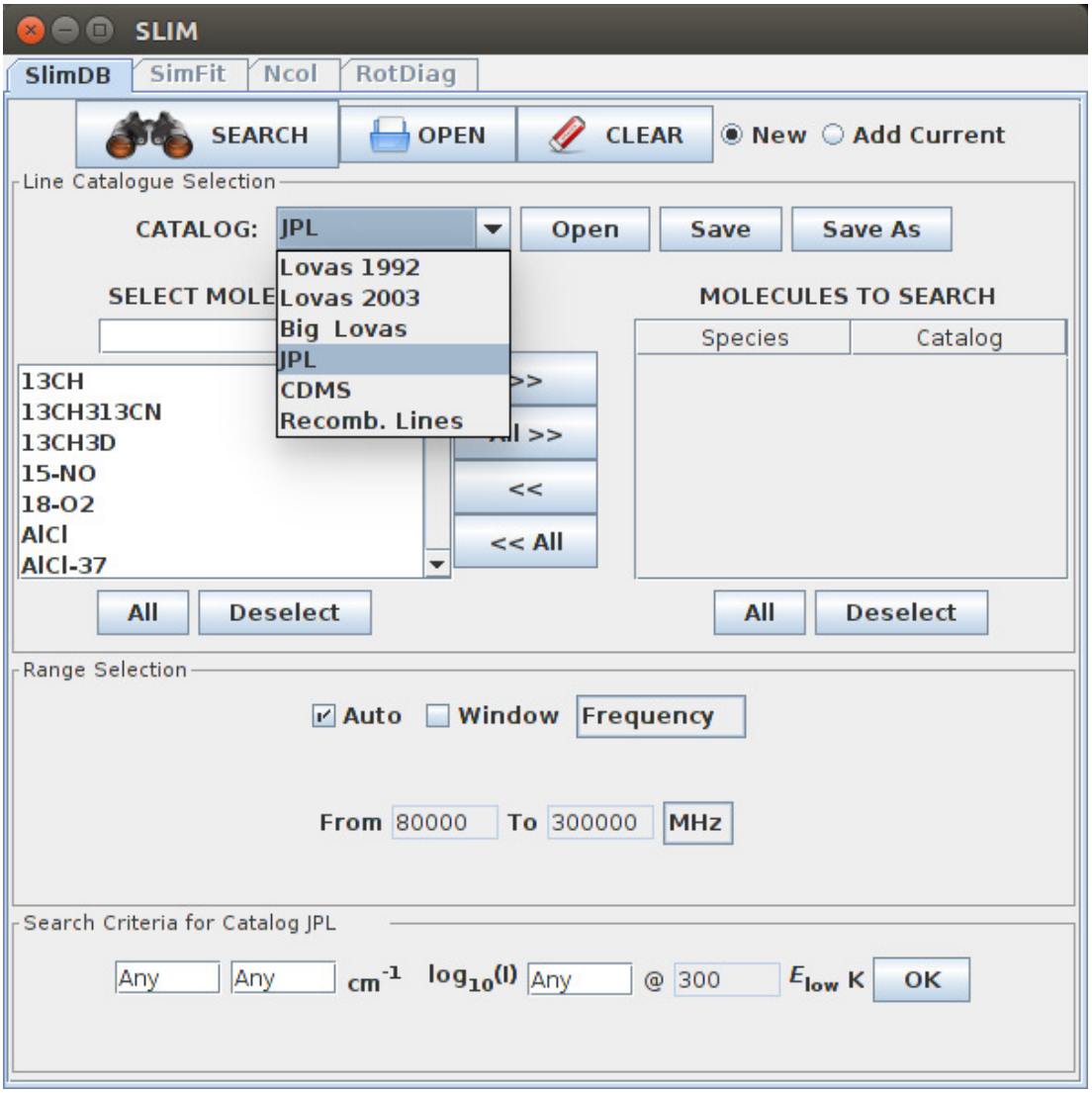

Figure 3.3: Search molecules by Catalogues, including JPL, CDMS and Lovas.

3.2.3 Column density

In the case of optically thin emission for the observed molecular transitions, the column density of the upper level can be derived as:

$$\mathrm{Nu}= \frac{(8\pi k\nu^2)}{(hc^3 Aul)}\ (1-\ \frac{J\nu(T_{BG})}{J\nu(Tex)})^{-1}\ \int\ \mathrm{T}_B\mathrm{dv}$$

where Aul are the Einstein coefficient for a transition connecting the levels u and l. In the Raleigh-Jeans approximation hν $\ll$kT and assuming Tex$\gg$T$_{BG}$ is obtained

$$\mathrm{Nu}= \frac{(8\pi k\nu^2)}{(hc^3 Aul)}\mathrm{W}$$

where W= $\int$ T$_B$dv is the integrated intensity derived from the Gauss fits to the lines.

In the LTE case the population distribution of all levels can be represented by a single temperature, the excitation temperature (T$_{ex}$)

$$\frac{N_u}{g_u}= \frac{N}{Z}\ \mathrm{e}^{-E_u/KT_{ex}}$$

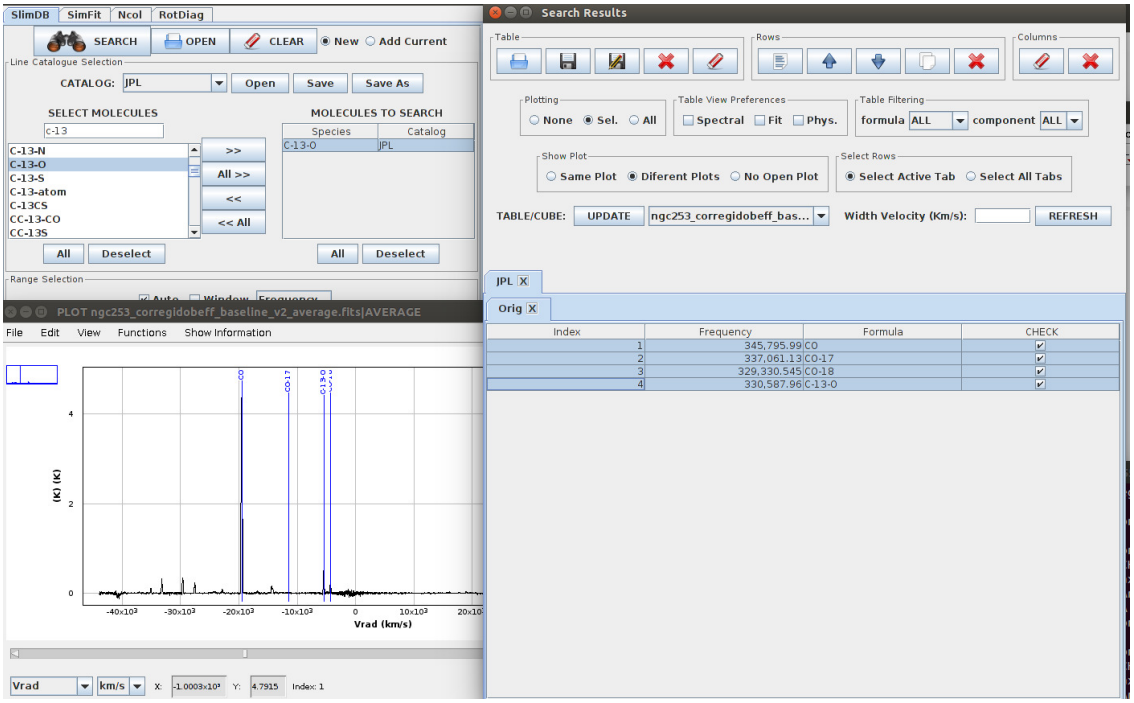

Figure 3.4: Example of search of the CO molecular line and their isotopes toward NGC 253 using MADCUBA

where Z is the partition function

$$\mathrm{Z}= \Sigma_i \ \mathrm{gi} \ \mathrm{e}^{-E_i/KT_{ex}}$$

and g_u is the degeneracy of the upper level

Then the total column density is given by:

$$\mathrm{N}= \frac{(8\pi k\nu^2 Z)}{(hc^3 Aul g_u)} \ (\int \ \mathrm{T}_B \mathrm{dv}) \ \mathrm{e}^{\frac{E_u}{KT_{rot}}}$$

Using the partition function provided by the spectral line catalogues and the derived T_{ex}, MADCUBAIJ calculates the total molecular column densities.

3.2.4 Multiline LTE line profiles simulator.

The large number of broad molecular lines observed in our spectral scans of the three galaxies (see Fig. 3.2) makes highly likely the overlap of molecular lines from different species making very difficult to disentangle the contribution from the different molecules. MADCUBAIJ simulates the expected lines profiles for all the detected molecules by using the predicted LTE emission for the case of a uniform plane parallel cloud with a constant excitation temperature . The simulation use Gaussian profiles with the line widths and radial velocities of the components observed in the corresponding galaxies.

The synthetic Gaussian profile fit of lines which are blended with others, or that show multiple features or hyperfine structure allows us to separate the contribution of each of the observed features. The synthetic fit from MADCUBA IJ has four parameters that can be fixed, or let them: column density, excitation temperature, line position, and line width.

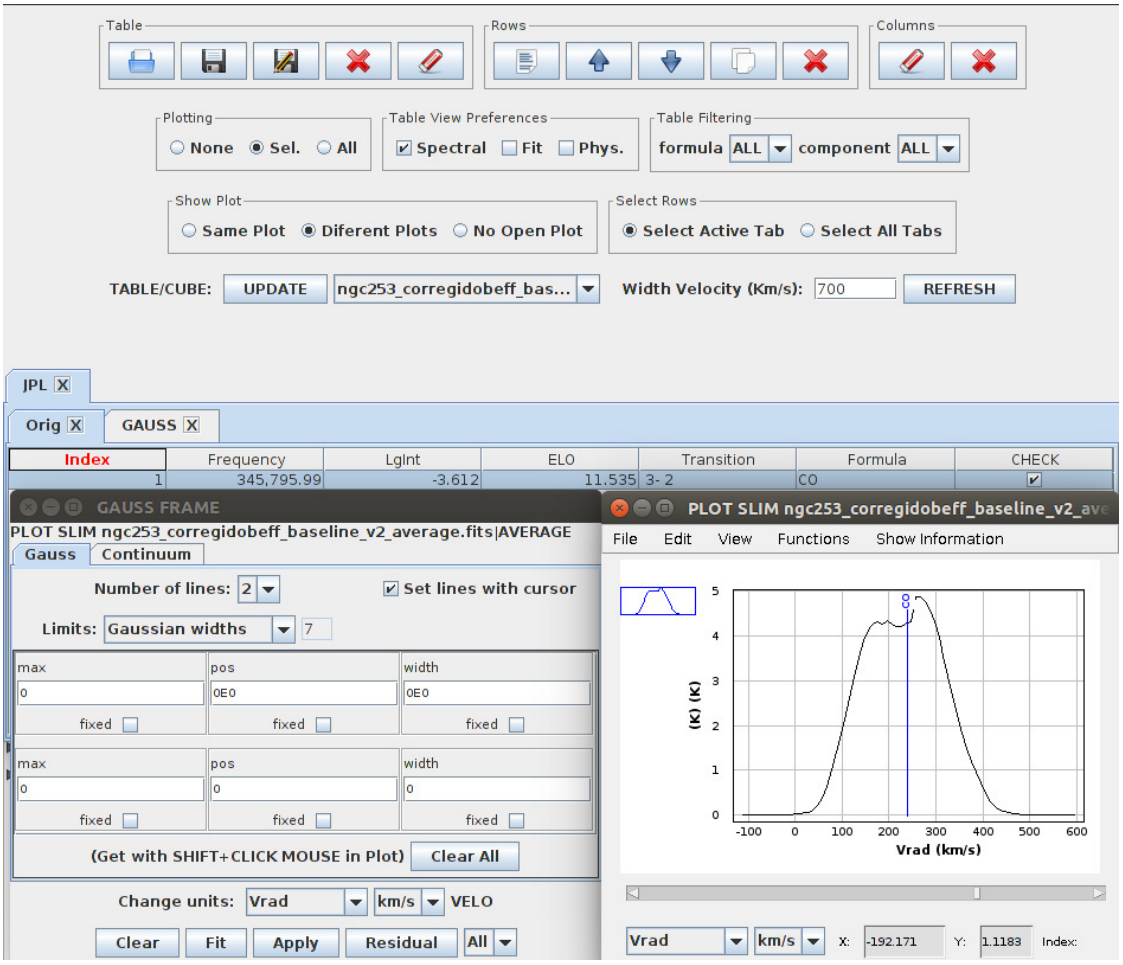

Figure 3.5: Example of the Process to obtain the Gauss fit toward NGC 253 using MADCUBA

3.2.5 Source Sizes

As mentioned in the previous section, the source size of the molecular emission is a key parameter to derive the total column density from our data. Since our data themselves cannot be used to derive source sizes, we used high angular resolution mapping to estimate them in the three galaxies of our study.

For NGC 4945, an averaged source size of $18'' \pm 5''$ was estimated from an elliptical Gaussian fit to the ^{12}CO $J = 2 \rightarrow 1$ map reported by Dahlem et al. (1993), which agrees (within the uncertainties) with the source size reported by them and by Curran et al. (2001).

Similarly an elliptical Gaussian fit to the ^{12}CO $J = 6 \rightarrow 5$ map obtained with CHAMP$^+$ on the APEX telescope by Pérez-Beaupuits et al. (in preparation) gives a CO source size of 20.8"×12.5", which corresponds to an average circular source size of 16.7", for NGC 253. The source size used by Martin et al. (2006) and Aladro et al. (2015) was 20" obtained from data from the IRAM telescope.

For the emission of Arp 220 we assumed a source size of 2" based on the CO J = 2-1 maps by Scoville et al. (1997) and Martin et al. (2011).

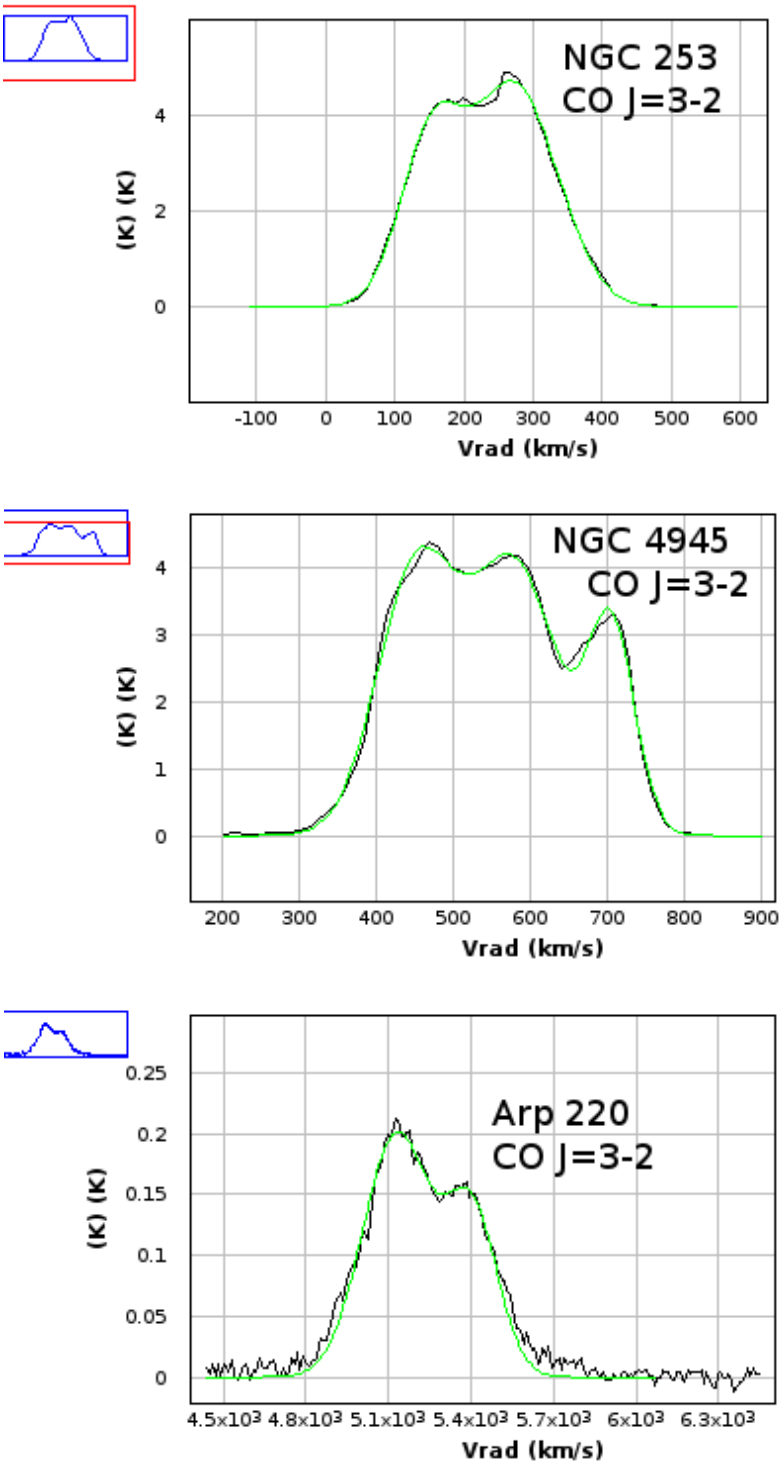

Figure 3.6: Velocity components on the most intense line of CO toward NGC 253, NGC 4945 and ARP 220.

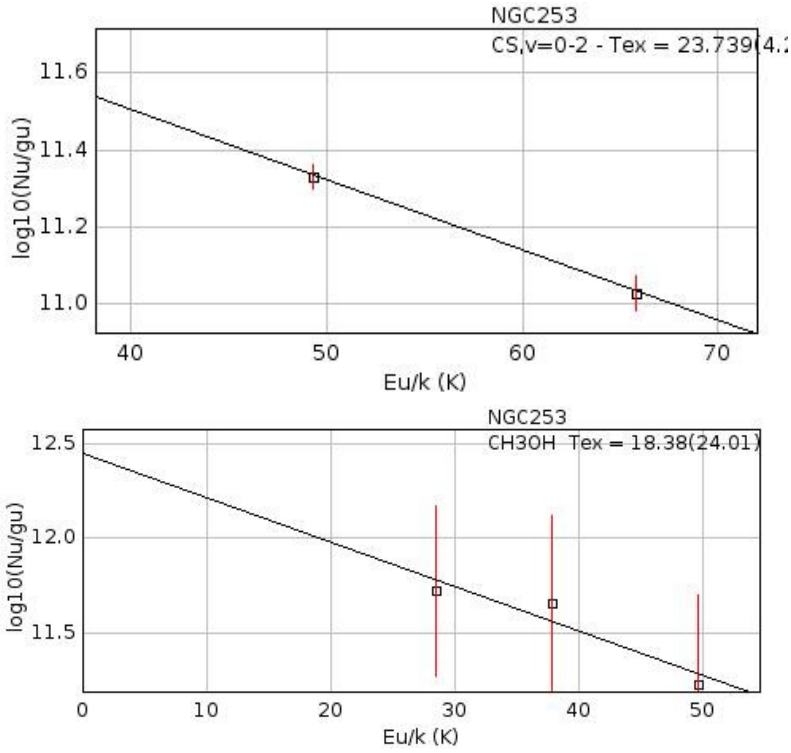

Figure 3.7: Top: Rotational diagram of CS. Bottom: Rotational diagram of CH_3OH, molecules toward NGC 253

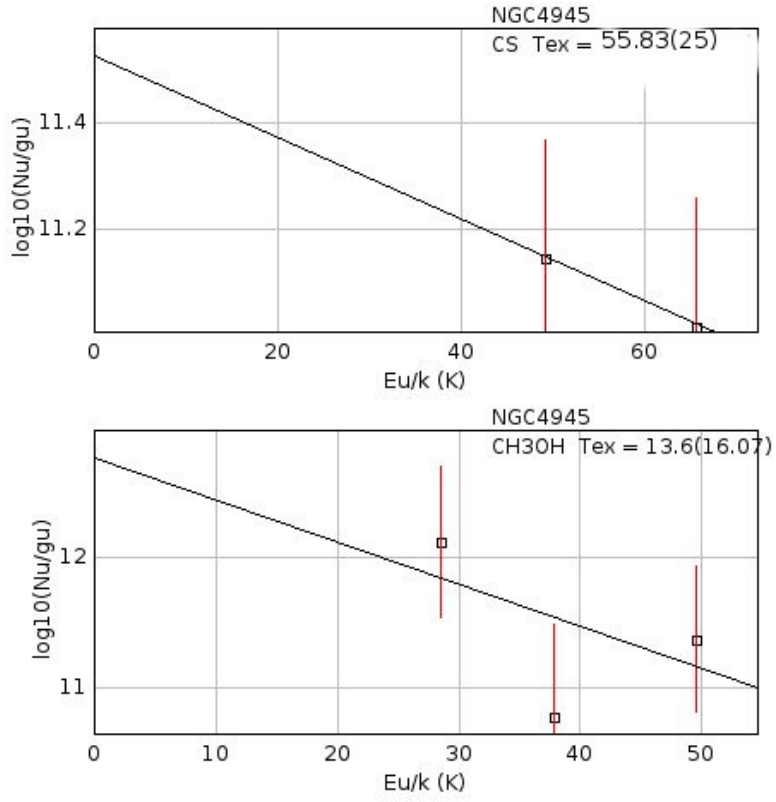

Figure 3.8: Top: Rotational diagram of CS. Bottom: Rotational diagram of CH_3OH, molecules toward NGC 4945

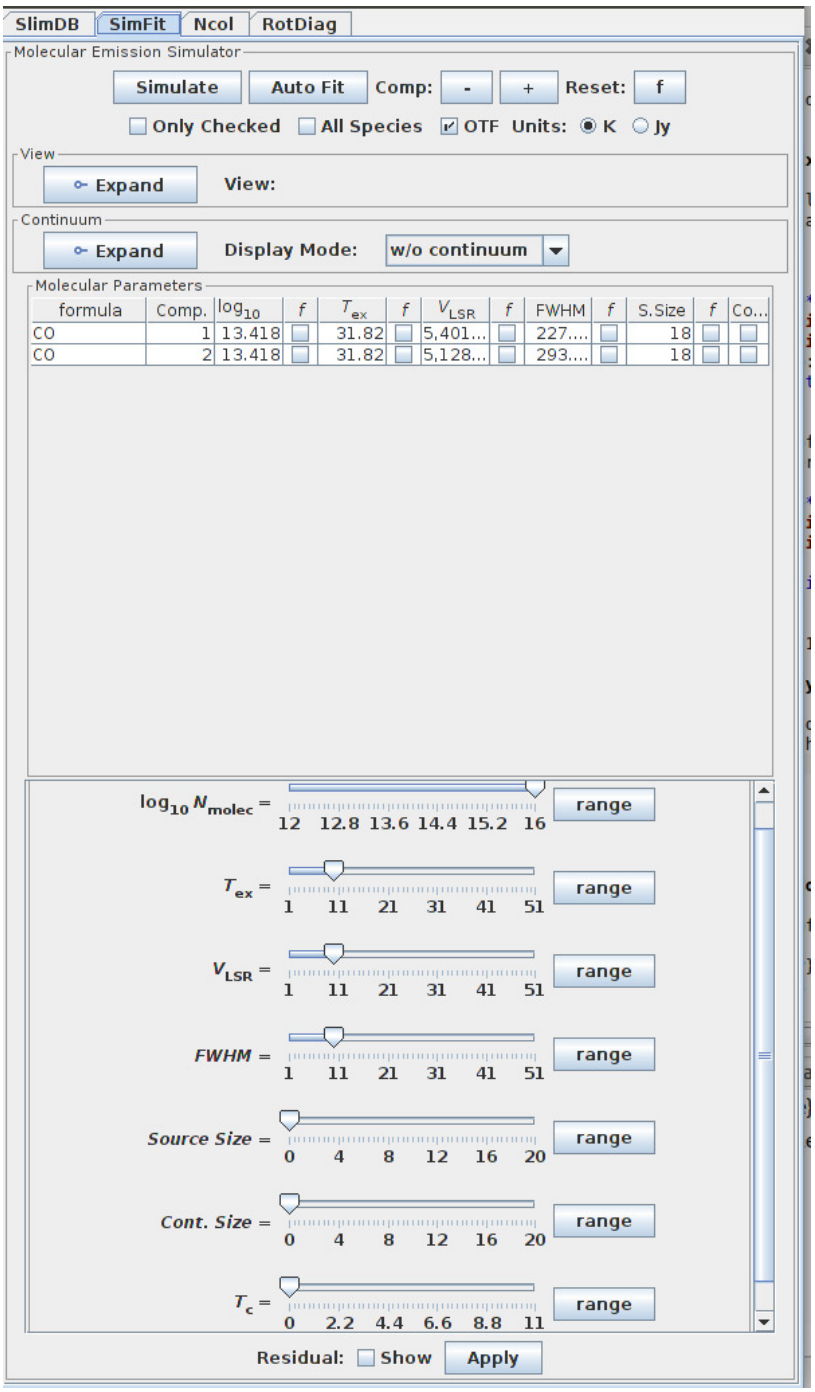

Figure 3.9: Simulate fitting using MADCUBA IJ with CO molecule toward NGC 4945, we can fit multimolecules together using the option "all species" in one line to know the contribution of every molecule in one blended line.

Chapter

4

Multitransitions study of H_3O^+

4.0.6 H_3O^+ (Hydronium)

H_3O^+ (Hydronium) was tentatively detected in OMC1 by (**?**) and subsequently confirmed in OMC1 and in the Sgr B2 molecular cloud near the Galactic center (Wootten et. al (1991)). The high proton affinity of water makes hydronium a key ion in the oxigen chemistry in dense molecular clouds and can be used to estimate their ionization degree (Phillips et al. 1992). It is therefore considered to be an excellent tracer of PhotoDisocciation Regions (PDRs) produced by the UV radiation from stars and X-ray Dominated Regions (XDRs) in the accretion disks around massive black holes. Observations of the H_3O^+ emission probe the location of dense and warm gas in galactic nuclei and have the potential be be used to trace the ionization rate induced by cosmic rays from supernovae, starburst and/or X-rays from an AGN. H_3O^+ can be therefore used to identify and analyze the type of activity in very deeply obscured galactic nuclei including that of the Miky Way.

Mapping of the the para-H_3O^+ transitions $J_k = 3_2\ ^+ - 2_2\ ^-$ at $\nu = 364.7974$ GHz (hereafter the 364 GHz line) and $J_k = 1_1\ ^- - 2_1\ ^+$ at $\nu = 307.1924$ GHz (hereafter the 307 GHz line) has been used, in combination with the H_2O abundances, to claim that cosmic rays dominates the ionization of the Galactic center clouds (Van der Tak 2006). Recently, a number of lines of H_3O^+ from metastable levels were detected in the Far-IR toward Sgr B2 (Lis et al. 2012) where the excitation could be due to pumping by X-rays irradiating the cloud. Aalto et al. 2011 have observed the 364 GHz transition towards the centres of seven active galaxies to investigate the impact of starburst and active galactic nuclei activity on the chemistry of the extragalactic interstellar medium. They found high H_3O^+ abundance, in excess of 10^{-8}, in four galaxies with different type of activity: NGC 253, NGC 1068, NGC 4418 and NGC 6240. Only in IC 342 the H_3O^+ abundance was an order of magnitude lower than in the other galaxies. In this case a standard PDR chemistry could explain such low observed H_3O^+ abundance. While the large H_3O^+ abundances derived towards the other four galaxies are generally consistent with

predictions of XDR models. Aalto et al. 2011 also considered an alternative scenario, in which H_3O^+ could be formed from H_2O evaporating from dust grains and reacting with HCO+ in a warm, dense gas. Shocks would help remove water molecules from grain mantles, resulting in an enhanced gas-phase water abundance.

However, as pointed out by Aalto et al. 2011, the high para-H_3O^+ abundance, which ruled out the PDR scenario even for SB galaxies like NGC253, were derived from the observation of just one line, the 364 GHz line and assuming thermalization. Therefore the derived abundance could be strongly influenced by the assumed excitation conditions. In fact, the multi-transition study by Phillips et al. (1992) showed that the radiative excitation by dust in the Far-IR can play a significant role in the excitation of the sub-millimeter lines of H_3O^+. In the spectral line surveys carried out in this thesis we have detected two para-H_3O^+ lines that can be combined to better constrain the abundance of this molecule toward the nuclei of NGC253, NGC4945 and Arp220. In addition to the two lines detected as part of the spectral survey, we have carried out follow up observations towards NGC253 of two additional submillimeter lines of H_3O^+ with APEX and extracted the Far IR HIFI spectra of the transition arising from the ortho and para ground levels. The additional lines are: the para-H_3O^+ line $J_k= 3_1\ ^+ - 2_1\ ^-$ at 388.458 GHz (hereafter the 388 GHz line), the ortho–H_3O^+ $J_k= 3_0\ ^+ - 2_0\ ^-$ at 396.272 GHz (hereafter the 396 GHz line), the ortho–H_3O^+ $J_k= 1_0\ ^- - 0_0\ ^+$ at 984.6967 GHz (hereafter the 984 GHz line) and the para–H_3O^+ $J_k= 1_1\ ^- - 1_1\ ^+$ at 1655.8136 GHz (hereafter the 1665 GHz line).

4.1 Results and Analysis and the H_3O^+ emission

The profiles of the Hydronium lines extracted from the spectral surveys and the targeted observations with the APEX telescope are presented in Figs 4.8 (NGC253), 4.2 (NGC4945) and 4.3 (Arp220). The spectra clearly show the detection of the transitions of para-H_3O^+ in NGC253. However there is no clear detection of the 396 GHz line. For the other two sources the 364 line is clearly detected, but the 307 GHz line is only marginally detected in Arp 220. Our line profile and intensity of the 364 GHz line in NGC253 agrees within the calibration uncertainties with that reported by Aalto et al (2011) observed with the JCMT. However, our line intensity in Arp220 is a factor of 2 larger than that reported by van der Tak et al. (2007), which might be related to the limited baseline provided by the narrow bandwidth of the backend used at the JCMT.

4.1.1 LTE models

Following the procedure described in Chapter 3 we first analyzed the H_3O^+ emission using the LTE approximation (SLIM tool in MADCUBAIJ, Chapter 3). Unfortunately, as pointed out by Van der Tak (2006) the 307GHz line of H_3O^+ is strongly blended with the 307.16594GHz line ($J_k= 4_1 - 4_0$) of CH_3OH (see below). For NGC253 the 388 GHz ortho-H_3O^+ line is blended with transitions of SO_2 and ^{33}CS, and the 396GHz is blended with $S^{18}O$ and NH_2CN, but their predicted intensities (see Chapter 5) are below our senstivity.

Table 4.1: Derived parameters from the LTE line profile analysis for CH_3OH for the different velocity components. We used two velocity components for NGC253 and Arp220, while three components for NGC4945. The derived parameters are: column density(N), radial velocity and line width (FWHM). We have used a Tex=20K which basically fits, within the noise, all the observed lines. We have used two transitions ν=305.473.52GHz (J_k= 3_1 - 3_0) and 309.2904GHz (J_k= 5_1 - 5_0) because they were the transitions not contaminated by the emission from others molecules.

Galaxy CH_3OH	N (cm^{-2})	Tex (K)	Velocity (km s^{-1})	FWHM (km s^{-1})
NGC 253	14.118	20	172.131	62.296
	14.335	20	266.018	98.393
NGC 4945	14.059	20	457.297	114.671
	13.811	20	624.814	118.895
	14.906	20	680.000	97.142
ARP220	15.32	20	5350	250
	15.609	20	5450	250

CH_3OH

To carry out a multi transition study of H_3O^+ we need first to estimate the H_3O^+ 307.19 GHz intensity from our blended profiles. Fortunately, our spectral surveys provide detections of all the CH_3OH transitions in the wide observed bandwidth. To estimate the 307.16 GHz CH_3OH line intensity we have used the LTE predictions for the two strongest CH_3OH lines which are not contaminated by other species and are the closest in frequency to the H_3O^+. The two lines, J_k= 3_1 - 3_0, at ν=305.473.52 GHz (305 GHz line) and J_k= 5_1 - 5_0 at 309.2904 GHz (309 GHz), arise from levels with lower and larger energies than the 307 GHz CH_3OH transition. For the CH_3OH LTE simulations (see also chapter 3) we used gaussian profiles with 2 velocity components for NGC 253, and Arp 220 and 3 components for NGC4945. Fig. 4.4 illustrates the results from the LTE line profile analysis, as solid line, superimposed on the observed CH_3OH profiles. While the upper and lower spectra of CH_3OH show the uncontaminated lines, the middle panel shows the predicted CH_3OH emission (solid line) which clearly does not fit the observed profile. The excess in emission corresponds to the contribution of the 307 GHz H_3O^+ to be used for the multiline analysis of H_3O^+. The predicted line intensity of the 307 GHz line of CH_3OH for NGC4945 and Arp220 is show in Figs. 4.2 and 4.3, respectively.

para- H_3O^+

Once the intensities of the 307 GHz line of H_3O^+ has been corrected from the contamination of the 307 GHz line of CH_3OH, we can carry out the multiline analysis. Typical excitation temperatures of transitions from high dipole moment molecules are typically 20-50 K (see next chapter). We have made the LTE line profile analysis with the line parameters in Table 2 for the 3 sources. Figs 4.1 , 4.2 and 4.6 show the results of LTE profiles for NGC4945, Arp 220

Table 4.2: Derived parameters from the LTE line profile analysis for H_3O^+ in NGC253 (2 velocity components), NGC4945 (1 velocity component) and Arp 220 (1 velocity component). We have used two extreme Tex of 20 and 800 K to illustrate the effects of the excitation temperature on the line ratios.

Galaxy	log(N) (cm^{-2})	Tex (K)	Velocity (km s^{-1})	FWHM (km s^{-1})
NGC253	13.796	20	168.27	47.8
	13.985	20	258.94	54.86
	14.093	800	168.27	47.8
	14.092	800	258.94	54.86
NGC4945	14.133	20	638.027	158.704
	14.633	800	638.027	158.704
ARP220	15.64	20	5472	354.591
	16.14	800	5472	354.591

and NGC253. One can really see that the typical low excitation temperatures derived for other species of 20-30 K cannot explain all the observed profiles. This applies to the 1655 GHz line of NGC253 (Fig. 4.7).

Let us consider the case of NGC4945 (fig. 4.1). The observed 364 GHz line is stronger than the predicted one by more than two orders of magnitude. Even for unreasonable excitation temperatures of 800K, which increase the ratio of the 364 line with respect to that of the 307 line, the observed 364 GHz line is still one order of magnitude larger than the predicted one. The same behavior is found for the other sources. This would indicate that the 364 GHz line, used in most studies to derive the H_3O^+ abundance, is "overluminous" with respect to LTE analysis. This could lead to an overestimation of the H_3O^+ column densities by more than one order of magnitude if based on this transition alone.

ortho-H_3O^+

For NGC253 we have also observed the ortho lines at 396 GHz and 984 GHz. The ortho lines can be fit with the LTE approximation (Figs. 4.8) for a excitation temperature of 200K and ortho-H_3O^+ column density which is factor of about 5 smaller than the para-H_3O^+ column density. This is not expected in LTE since the ortho-to-para ratio should be 2 for low excitation temperatures and 1 for high excitation temperatures. This confirms that LTE approximation can not explain all the observed transitions.

4.1.2 Non-LTE analysis

Since LTE analysis cannot explain all the observed lines in a coherent way, let us consider if a non-LTE analysis can fit all data. We will concentrate on the source with the most complete set of data, NGC253. The results obtained for this source will be applied to the other two sources. We will first consider the case of collisional excitation alone.

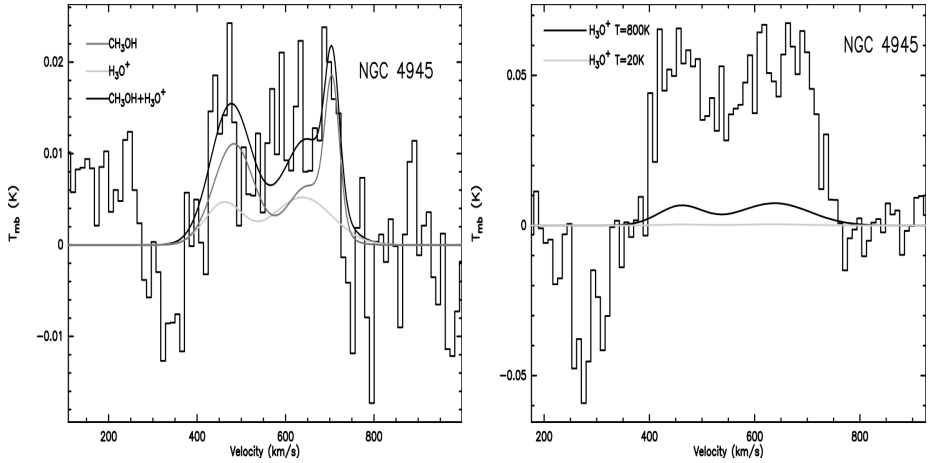

Figure 4.1: Spectra of H_3O^+ in NGC4945 observed with APEX. Top spectra shows ν= 307.1924 GHz and bottom spectra ν= 364.7974 GHz. The fits shows in the top the fits to the overlapped transitions CH_3OH (ν= 307.1924 GHz) and H_3O^+ as fitted in our analysis. In the botton two differetn LTE fits are shown, one for the temperature of 20K (clear line) and another at 800K (solid line).

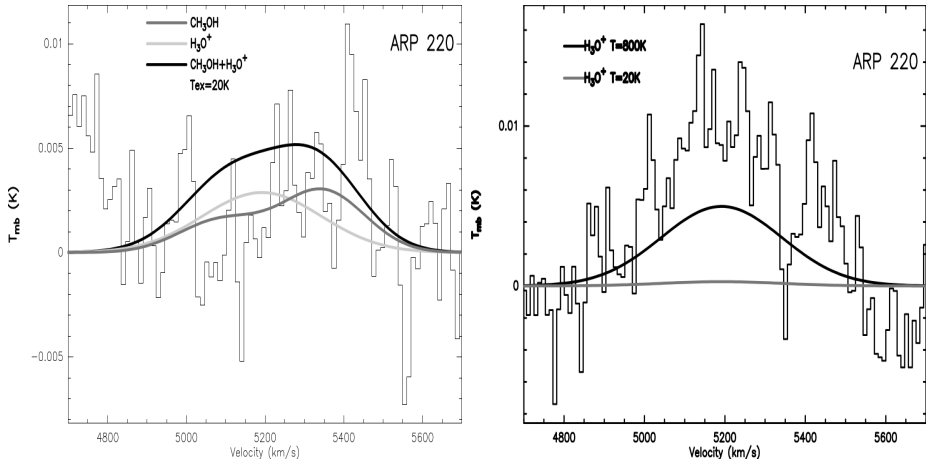

Figure 4.2: Spectra of H_3O^+ in ARP 220 observed with APEX. Top spectra shows ν= 307.1924 GHz and bottom spectra ν= 364.7974 GHz. The fits shows in the top the fits to the overlapped transitions CH_3OH (ν= 307.1924 GHz) and H_3O^+ as fitted in our analysis. In the botton two differetn LTE fits are shown, one for the temperature of 20K (clear line) and another at 800K (solid line).

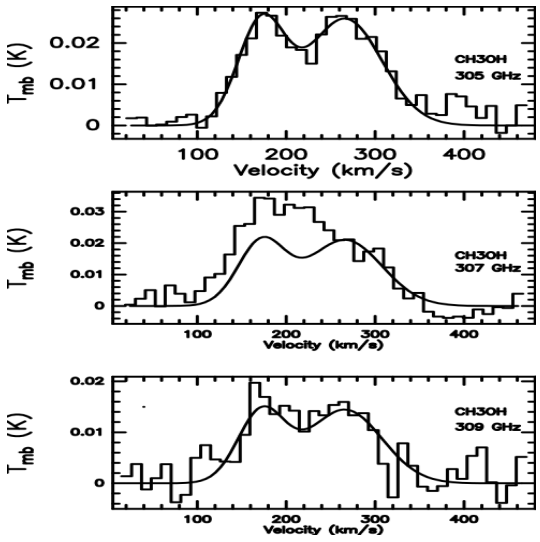

Figure 4.3: Spectra of CH_3OH observed with APEX at ν= 305, 307 and 309 GHz for Tex=20K.

Collisional excitation

To carry out the non-LTE analysis we used the radiative transfer code RADEX which considers the Large Velocity Gradient (LVG) approximation (Van der Tak et al. 2007). We have run RADEX for ortho- and para-H_3O^+ and considered a wide range of kinetic temperatures (20K, 200K, 400K, 600K and 800K), n(H_2) density from 10^5 to 10^8 cm^{-3}, and a temperature of the background radiation field of 2.73K. The results obtained in our calculation are similar to those in Fig.13 of Phillips et al (1992). An inspection to this figure shows that for collisional excitation the detection of the 307 GHz line require high density independently of the kinetic temperature. The three para lines can be fitted with a para column density of 8x10^{13}cm^{-2}, n(H_2) of about 10^7 cm^{-3} and a kinetic temperature of 80-100 K. However, when one considers the excitation of the orto lines with RADEX for these conditions the predicted 396 GHz line is about 10 mK, which is one other of magnitude larger. This is illustrated in Fig 13 of Phillips et al (1992) where the upper plots show that the 394 GHz line in the collisional excitation case is always stronger than the 364 GHz lines. This shows that the collisional excitation cannot explain the observed data in NGC253.

Radiative excitation

The bottom plots in Fig. 13 of Phillips et al (1992), indicate that the observed weakness of the otho 369 GHz line combined with the strong para 364 GHz can only be explained by assuming radiative excitation by dust in the low density regime. For H_2 densities of few 10^4 cm^{-3} and a dust temperature of about 20-40 K and a column density of H_3O^+ of about 10^{14}cm^{-2} one could roughly explain the observed intensities observed in NGC253.

For the other two sources in our sample NGC4945 and Arp220 we do not have enough data to distinguish between collisional (high density) and radiative (low density) excitation. As we will discussed in the next section, the results from the PACs Herschel data for Arp220 from Gonzalez-Alfonso et al (2013) suggest for this source also the low density solution. Assuming

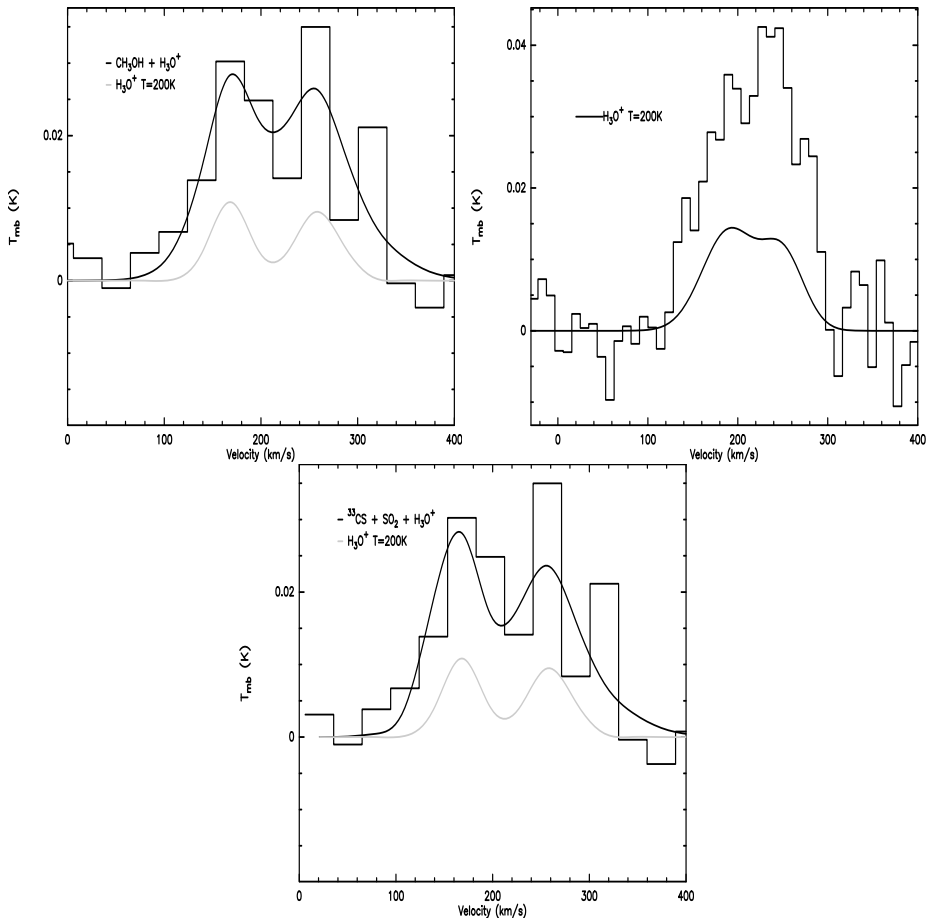

Figure 4.4: Spectra obtained with APEX at 200K. Top figure: 307GHz transition of H_3O^+ blended with CH_3OH dark line, while grey line is H_3O^+ molecule without blended; Center figure: 364GHz transitions of H_3O^+ without blended; Bottom figure: 388GHz transition of H_3O^+ blended with SO_2 (right) and ^{33}CS (left) in dark line, while, grey line is the H_3O^+ molecule contribution.

the low density solution with high kinetic temperature and dust temperatures of 20-60 K, we obtain column densities of about 10^{16}cm^{-2} for Arp 220 and about 5x10^{14}cm^{-2} for NGC4945.

4.2 Discussion

Our study of the excitation of H_3O^+ shows "overluminous emission" in the 364GHz transition in galaxies when a simple LTE analysis is considered which assuming high densities. A reliable determination of the H_3O^+ abundance from submillimeter lines needs the observation of several, at least two, lines of para-lines and one ortho line. Although the 307 GHz line is affected by blending with CH_3OH, the observation of other transitions of this molecule in the band allows to accurately account for its contribution to the observed profile. The 307 GHz line of H_3O^+ is crucial to derive the H_2 density from the ratio between the 364 GHz and the 307 GHz lines. The ortho 396 GHz line is also fundamental to establish the role of the radiative excitation by dust emission.

It has been proposed that the abundance of H_3O^+ can be used to derive the ionization rate in

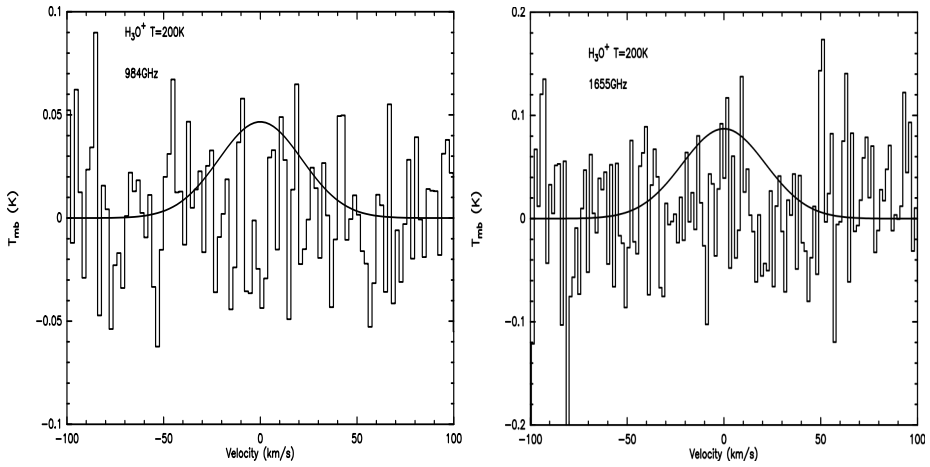

Figure 4.5: Image obtained from public archieve of HIFI Hershel in NGC 253 using 200K. Top figure: 984GHz: Bottom: 1655GHz. The column density obtained with temperature of 200K is Log(N)= 13.698 cm^{-2}, the rest of the parameters are the same obtained with APEX.

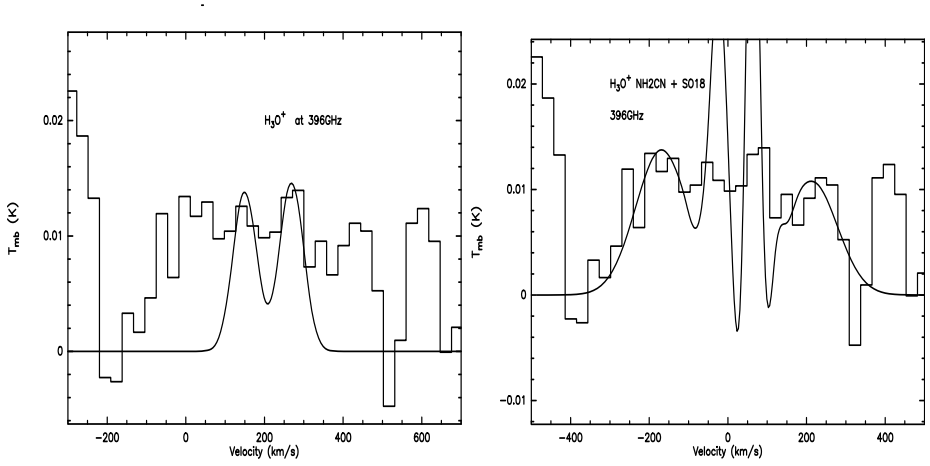

Figure 4.6: Fitting obtained for 396GHz ortho-transition. We have two clear components, using syntetic fitting at 200K: Log(N)= 13.35(12.929)cm^{-2}, with a FWHM of 71.524km/s and a velocity of 269km/s for the firs component; Log(N)=13.31(12.89)cm^{-2}, with FWHM of 70.469km/s and a velocity of 150km/s. The fit using the same parameters than para- transitions, The right side is the contribution of ^{18}SO and NH_2CN.

molecular clouds and to discriminate the origin of the main ionization source (UV radiation, cosmic rays, X-rays and shocks). The H_3O^+ column densities derived from our multiline analysis for Arp220 and NGC253 are 10^{16}cm^{-2} and 10^{14}cm^{-2}, respectively. The column densities derived for Arp220 are similar to those of previous submmillimteer studies by van der Tak et al (2007) and Far-IR Herschel PACS lines Gonzalez-Alfonso et al (2013). The resulting derived H_3O^+ abundance in Arp220 is of $\sim 10^{-8}$. Gonzalez-Alfonso et al (2013) has argued that the H_3O^+ is most likely dominated by production of H^+ by X-ray/cosmic ray ionization as indicated by chemical models. Our observations also support the idea that the molecular ions arise in a relatively low density ($\leq 10^4$cm^{-3}) interclump medium. The required ionization rate would be $> 10^{13}$s^{-1}, two orders o magnitude higher than those estimated for the Galactic regions. However the required cosmic ray energy density is smaller than the one previously from the supernova rate and synchrotron radio emission. For Arp220 we conclude that the H_3O^+ abundance of 10^{-8} could be explained by the effects of the starburst through the production of this molecule by ion-molecule reactions in relatively low density envelopes which are irradiated by the cosmic rays produced in supernova remnants.

Our H_3O^+ column densities for NGC253 is a factor 25 smaller than those of Aalto et al (2011). This would indicate that the H_3O^+ abundance is about 10^{-9} . Aalto et al. (2011) have claimed that a large abundance of H_3O^+ of about 10^{-8} in NGC253 could no be explained by its formation due to the ionization produced by the UV photons from the starburst and suggested the possibility that X-rays played a key role. However, an abundances of 10^{-9} could be explained by the formation in the PDRs surrounding the molecular clouds generated by the UV radiation from the starburst. This would be consistent with the models presented in van der Tak et al. (2008) in which the H_3O^+ cannot not exceed 3x10^{-9} in PDRs. The emerging scenario from our results is that NGC253 is a relatively evolved starburst with molecular clouds with substantial low density envelopes which are irradiated by the UV photons from the starburst (see eg. Aladro et al 2015).

NGC4945 has not been previously observed in H_3O^+. From the H_2 column density derived in the next Chapter of 8x10^{22} cm^{-2} we estimate an H_3O^+ abundance abundance of 8x10^{-9}. It was claimed by Aalto et al (2011) that H_3O^+ abundances of 10^{-8} or larger are more likely to occur in X-ray dominated regions and formation of this molecule will be mainly initiated by X-rays, favoring the XDR scenario. It is well know that NGC4945 is a strong X-ray emitter and harbor a black hole in its center. Although a more careful analysis is needed to confirm the relatively high abundance of H_3O^+ by observing more transition of this molecules, the XDR like in NGC1068 will be the preferred scenario to explain the emission of this molecular ion. Observations of the H_3O^+ emission with ALMA will help to probe the location of the warm gas in galactic nuclei, which can be used to trace the ionization rate and establish its origin, i.e. cosmic rays from supernovae, starburst and/or X-rays from an AGN..

4.3 Conclusions

We have detected the emission from para-H_3O^+ toward the nuclei of NGC253, NGC4945 and Arp220 in two submillimeter lines, the 307 GHz and the 364 GHz. We also observed another

submillimeter transition of para-H_3O^+, the 388 GHz line, and one ortho-H_3O^+ transition, the 396 GHz line toward NGC253. HIFI Herschel observations of the ground state lines in the Far-IR are also presented.

We carried out a multiline transition analysis of the H_3O^+ emission toward NGC253. We first corrected the 307 GHz line of H_3O^+ for the blending of the 307 GHz line of CH_3OH using other methanol transitions observed in our surveys. Our LTE excitation analysis of H_3O^+ of NGC253 shows that all line cannot be properly fitted and that the364 GHz line seems to be over-luminous, suggesting that the derived column densities using only this line could result in severe overstimations.

From our non-LTE analysis of H_3O^+ in NGC253 with RADEX we found that the collisional excitation cannot explain the observed intensity of the ortho 396 GHz line. Excitation by radiation from the dust in the Far-IR can roughly explain the observations if the H_2 densities are relatively low (a few 10^4 cm^{-3}).

Our derived column densities agree well with that derived previously using submillimeter and Far-IR lines for Arp220, but is a factor of 25 smaller from that derived towards NGC253.

From the derived H_3O^+ column densities we conclude that the chemistry of this molecule is dominated by ionization produce by the starburst in NGC253 (UV radiation from the O stars) and Arp 220 (cosmic rays from the supernovae) and likely from the AGN in NGC4549 (X-rays).

Chapter

5 APEX submm extragalactic line surveys

5.1 Data Analisys

In this chapter we present the analysis of the first submillimeter spectral lines surveys of galaxies. We will derive the physical conditions and the chemical complexity of the galaxies NGC253, NGC4945 and Arp 220.

5.1.1 Line identification

The spectral scans observed with the APEX telescope were presented in chapter 2. In this section we will proceed to the identification of the molecular lines in the spectra of the three galaxies. We used MADCUBA_IJ ((described in chapter 3) that was created as plugin for spectra/cube analysis within the Image_J image processing program (http://arsbweb.nih.gov/ij/). Within this frame, MADCUBA_IJ is intended as a graphical tool to visualize and analyze astronomical data cubes and from spectra both extracted from cubes or single dish telescopes. We used the rest frequencies from the JPL (Picket et al. 1998) and observe with the CDMS (Mueller et al. 2001, 2005) catalogs to identify each molecular feature in the surveys.

Before proceeding to the line identification we checked for the possible contaminations from the image band expected for strongest lines in the survey when the image ejection was below 10 dB. We used the CLASS from GILDAS to check lines coming from the image band of the spectra. The only spectra affected by features coming from the image band was NGC 253 at 360GHz that correspond to image band of the very strong line of CO.

We found for NGC253 150 transitions of 26 molecules and 4 nidentified (hereafter U) lines; for NGC 4945 136 transitions of 24 molecules and 1 U line; in Arp 220 64 transitions of 17 molecules and 6 U lines including isotopologues.For many molecules we have detected several transitions, but for others the identification is uncertain as we have only one molecular transition on the sur-

veys. When possible (for NGC253 and Arp 220) we check our identifications with the molecules already reported from previos surveys at mm wavelengths. The results of the identifications are shown for the three galaxies in figures 6.2 to 6.6.

5.1.2 Spectral line fitting

The blending of lines affects direcly to the line profile making the analysis based on fitting of Gaussian to individual profiles very inefficient and uncertain. Spectra features What is needed is to consider the line profile of all relevant transitions from all the detected molecules simulateneously.

Is needed to fit synthetic spectra of each molecular species in the spectrum. Syntethic spectra of each molecule was calculated with spectroscopic parameters from the catalogues mentionated before. Using LTE(mentioned before) excitation and we calculated the molecular column density (N) and excitation temperature (Tex). An example of a blended line discussed in the previous chapter is shown in Fig. 6.1. the combination of the emission from the two molecules clearly fit the observed profile.

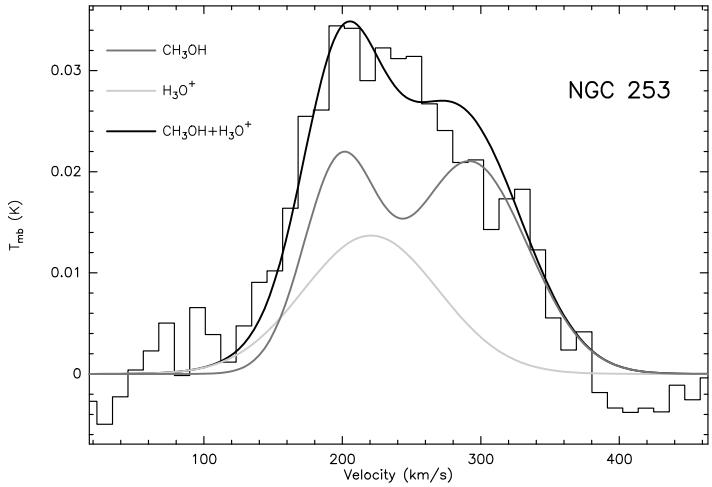

Figure 5.1: Blended lines discussed in detailed in the previous chapter toward NGC 253 at 307.19GHz. The figure shows H_3O^+ molecule blended with CH_3OH, to obtain the contribution of the blended molecule

In this thesis we used the Slim simulator from MADCUBA IJ to identify the different molecular transitions and to derive the physical conditions and abundances of the different molecules. In order to have a first iteration of the identification we use energy levels 100 cm^{-1} and intense.

An average source size of $18'' \pm 5''$ was estimated for NGC4945 from an elliptical Gaussian fit of the ^{12}CO $J = 2 \rightarrow 1$ map reported by Dahlem et al. (1993), which agrees (within the uncertainties) with the source size reported by them and by Curran et al. (2001).

Similarly an elliptical Gaussian fit of the ^{12}CO $J = 6 \rightarrow 5$ map obtained with CHAMP$^+$ on the

APEX telescope (Pérez-Beaupuits et al., in preparation) gives a CO source size of 20.8"×12.5", which correspond to an average circular source size of 16.7" for NGC 253.

For the extended emission of Arp 220 we assumed a source size of 2" based on the CO J = 2-1 maps by Scoville et al. (1997) and Martin et al. (2011).

The final transition used in our analysis were interatively tuned as a function of the spectrospcopic properties of the identified molecules. To obtained the synthetc spectra we considered 2 velocity components for NGC253, 3 velocity components for NGC4945, and two velocity components for Arp 220.

A description of the excitation temperature used for fitting each molecule is in tne section Details on the fitting of individual species.

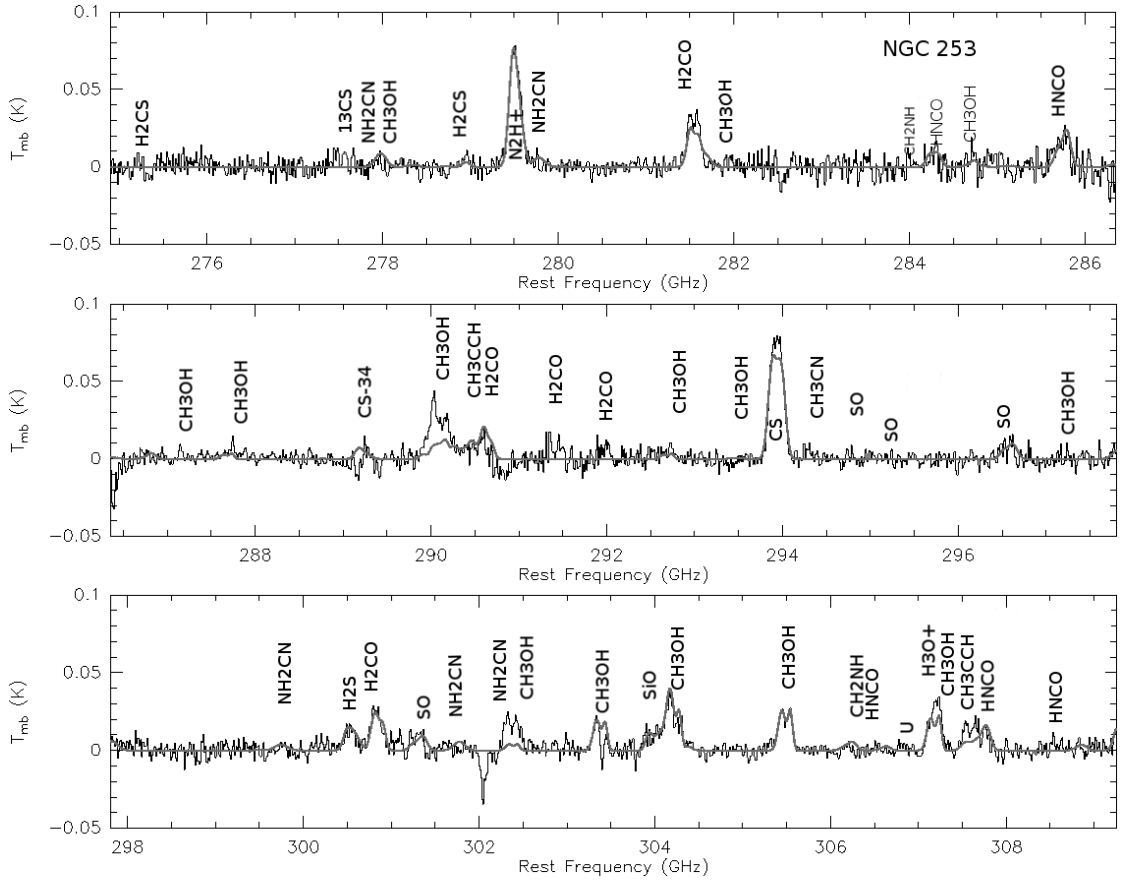

Figure 5.2: Identification lines toward the nuclear region NGC 253 from 270GHz to 308GHz.

5.2 Results

This section is divided in three subsections: the information about the column density and fitted molecules. The results of the fitting are shown in Figs. 6.2 to 6.6 and in Tables; the ratios between some molecules; and the comparation with others frecuencies.

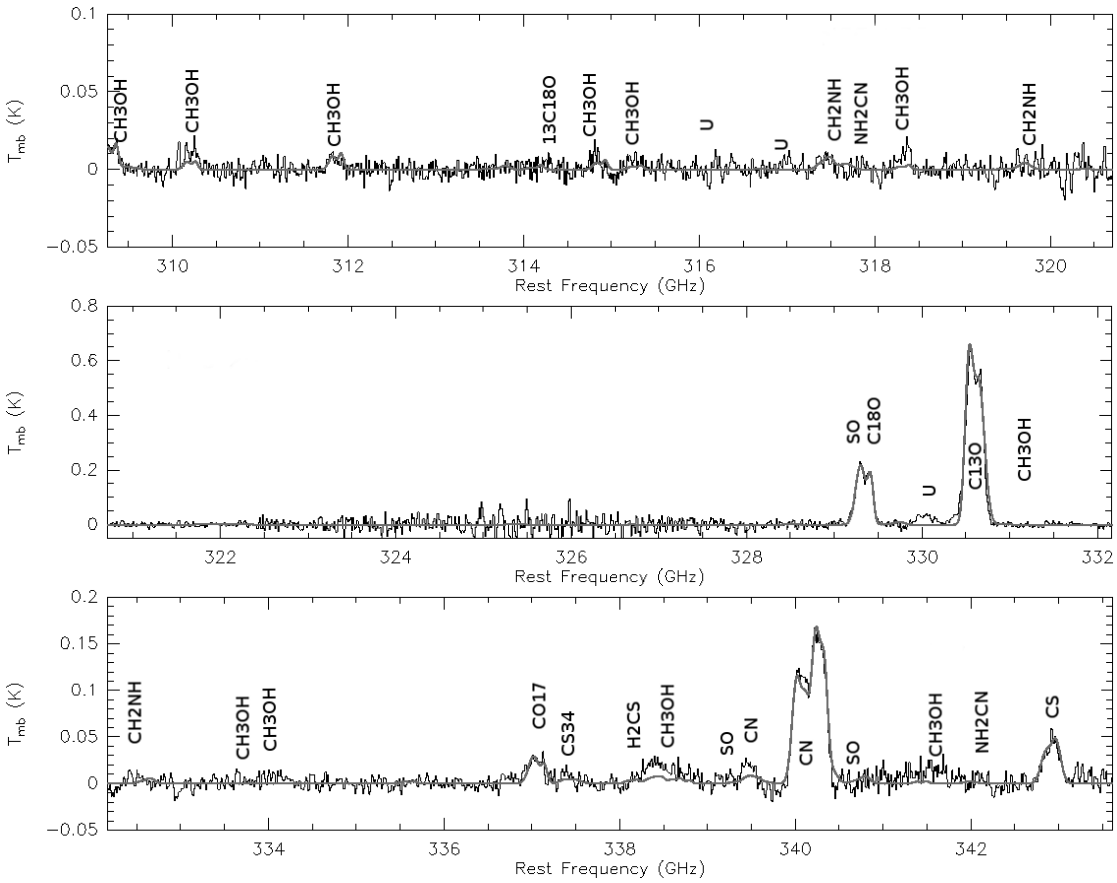

Figure 5.3: Identification lines toward the nuclear region NGC 253 from 308GHz to 342GHz.

5.2.1 Derived excitation temperatures

For NGC 253 was obtained the excitation temperature using the only simple molecule with two transition, CS. We first used the rotational diagram and find 23K and 15K for each component. We have column densities and abundaces similar of Martin et al. 2006, Aladro et al. 2015 and Wang et al. 2004. On another hand, we use 15K for ARP 220 similar to Martin et al. 2011. In the case of NGC 4945 we use the same consideration of NGC 253 taking the data from CS, we obtain 31K, 35K and 48K for each component. In all the galaxies we have also three clear transitions for CH_3OH.

5.2.2 Derived Column density

The column densities we derived from the simulation for the derived excitation temperatues when available or from the assumed values. Using the observed main beam brightness temperature we can obtain column densities (N) and rotation temperature (Trot) for each species. We used similar parameters velocity and FWHM than **?** for NGC253,**?** for NGC4945, and **?** for ARP220, and use synthetic model autofit in MADCUBA in order to get the error in the fit.

Assuming $\tau < 1$, using the column density in the upper level (Nu), the Raleigh-Jeans approximation (h $\ll$ KT) and Tex$\ll$T$_{BG}$, using Local Termodinamical Equilibrium (LTE). We shown the ecuation to obtain the column density N in LTE condition. Z is the partition function, Aul

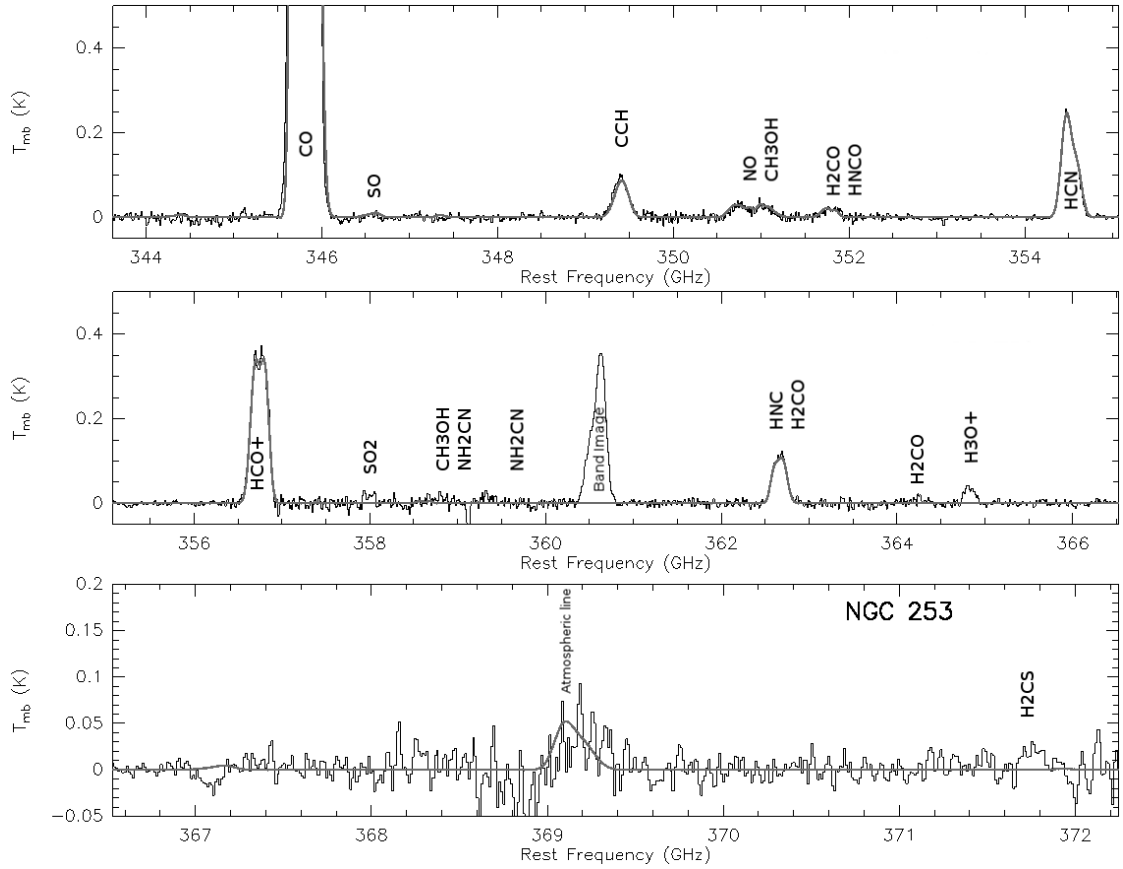

Figure 5.4: Identification lines toward the nuclear region NGC 253 from 343GHz to 372GHz

is the Einstein coefficient for a transition connecting the levels u and l, gu is the degeneracy of the upper level, Trot is the rotational temperature, Eu is the energy of the upper level.

$$\mathrm{N}= \frac{(8\pi k\nu^2 Z)}{(hc^3 Aulgu)} \left(\int \mathrm{T}_B \mathrm{dv}\right) \mathrm{e}^{\frac{Eu}{KTrot}}$$

5.2.3 Details of individual species.

In this section we explain all details about the molecules in our survey. Details like excitation temperatures, the column density for every velocity component, (if the case) of every molecule in each galaxy, comparation between the galaxies of the abundance and the case of blendind lines.We also include the the rms of the molecules that were not detected for one galaxy.

**HCN*: It is detected in the galaxies with one transition, it is most abundant in Arp 220, shows a negligible blended with c-C_3H_2 in NGC 4945 and it is blended with CH_3NH_2 in ARP 220.

**C_2H*: We found this molecule toward all galaxies, abundant is in Arp 220, NGC 253 and NGC 4945. C_2H has hiperfine structure clear and intense line, transitios J= $4_{5,4}$-$3_{4,3}$, J=$4_{4,4}$-$3_{3,3}$ and J=$4_{4,3}$-$3_{3,2}$ for NGC 253 and Arp 220. In the case of NGC 4945 and Arp 220, also we have

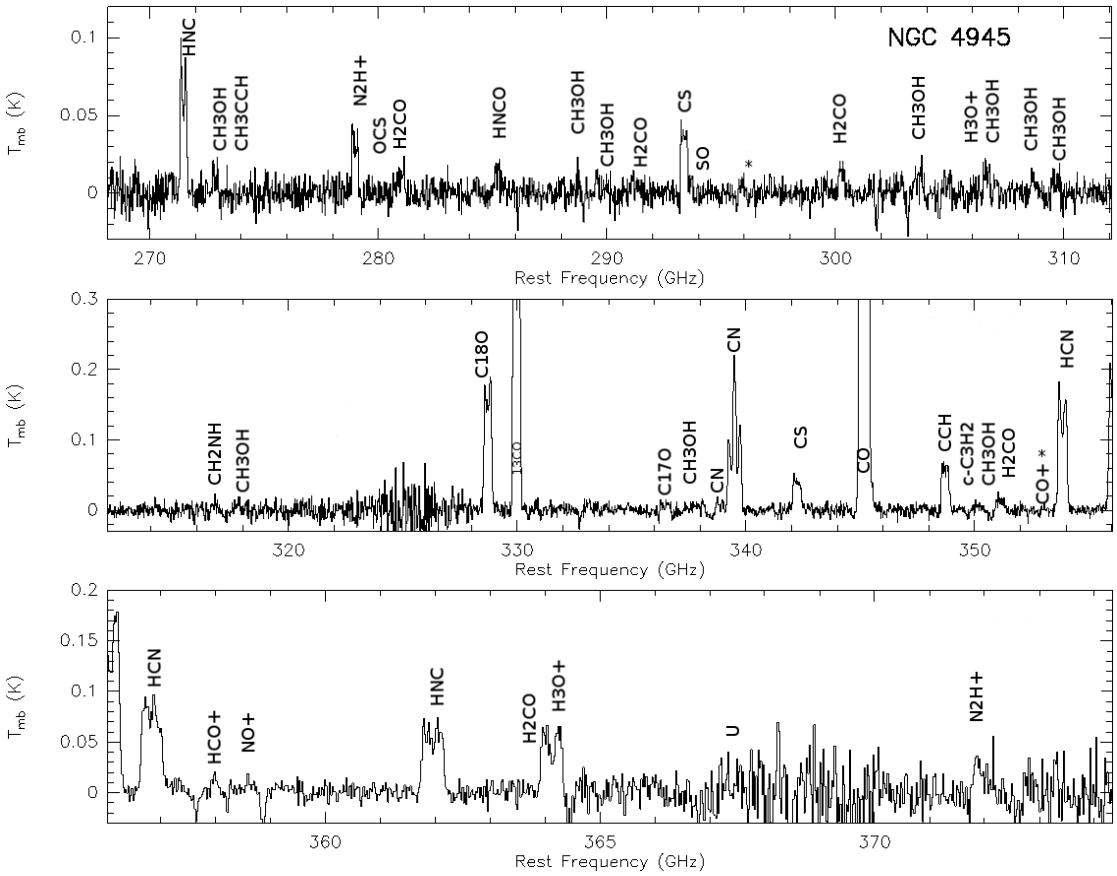

Figure 5.5: Identification lines toward NGC 4945.

J=$4_{5,5}$-$3_{4,4}$.

**CN*:It was in all galaxies, shows a hiperfine structure. This molecule is more abundant in Arp 200 than the others galaxies.

**^{13}CN*: It was only detected in Arp 220 and it was close of noise signal, thus it is considered tentative. One clear component is observed with an intensity of 0.008K and a second component but not clear with intensity of 0.004K, at a Tex of 15K (Martin et al. 2011) we got a Column density of 6.22(2.53)X10^{14}cm^{-2} has a rms of 0.025K in NGC 253, and 0.021K for NGC 4945.

**CS*: We found this molecule in all galaxies and has two clear transitions by consecuence we got a rotational temperature. For NGC 253 we got a Trot of 23.48(2)K and 14.83(1)K; for NGC 4945 we found a Trot of 31.82(3)K, 35.89K and 48.4(4)K; while for Arp 220 we have 15K from Martin et al. 2011.

**C^{34}S*: We found it three galaxies with one transition except for NGC 253. Present the most abundant case in Arp 220. The rotational temperature for this feature is the same than for CS except in the case of NGC 4945 for which has velocity component, for Arp 220 we used 15K because the same velocity component of CS. The isotope is most abundant in Arp 220.

**^{13}CS*: This isotope is only detected in NGC 253 with only one transition (J=6-5) and one

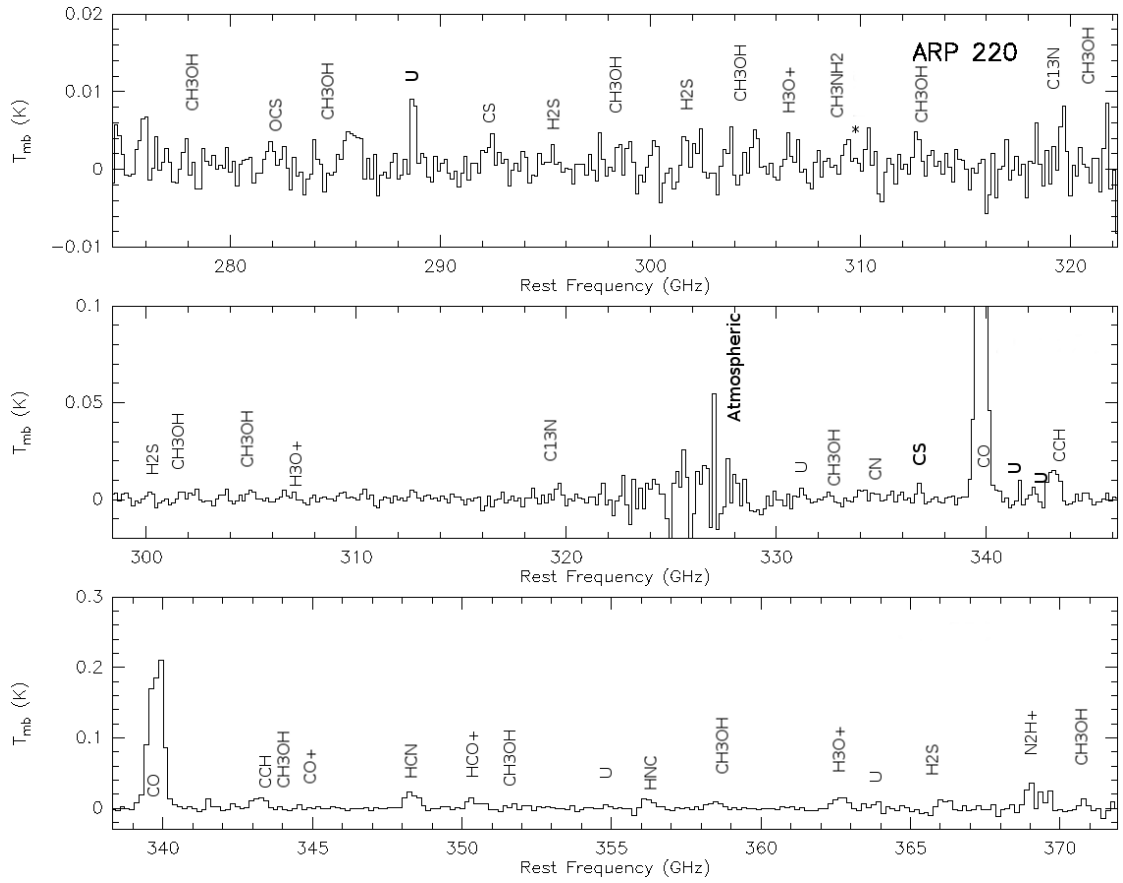

Figure 5.6: Identification lines toward ARP220.

component. The temperature was the same than the central component of CS. Column density is N= 1.34(0.25)x10^{13}cm^{-2}. The rms in Arp 220 8.64x10^{-3}K, and NGC 4945 4.09x10^{-3}K.

*HCO^+: We found the molecula in all the galaxies. The most abundant of this molecule was in Arp 220. It clearly shows 2 velocity components for NGC 253 and Arp 220, while 3 for NGC 4945.

*HNC: We found this molecule in all galaxies. There a small blending with H_2CO toward NGC 253.

*CO: The CO molecule was in all galaxies, it is the most intense of all the molecules, show only one transition in this study. Also, CO has 2 clear velocity components for NGC 253 and Arp 220, while three components for NGC 4945.

*^{13}CO: We found the isotope in NGC 253 and NGC 4945 but not in Arp 220 because it transition fall in atmospheric region which has a rms is 19.9x10^{-3}K. In the case of NGC 4945 and NGC 253 have closest abundances.

*$C^{18}O$: The line of this this isotope is inside of the atmospheric line of Arp 220. A rms of 14.8x10^{-3}K .C^{18}O was clearly observable in NGC 253 and NGC 4945 and have similar abundances.

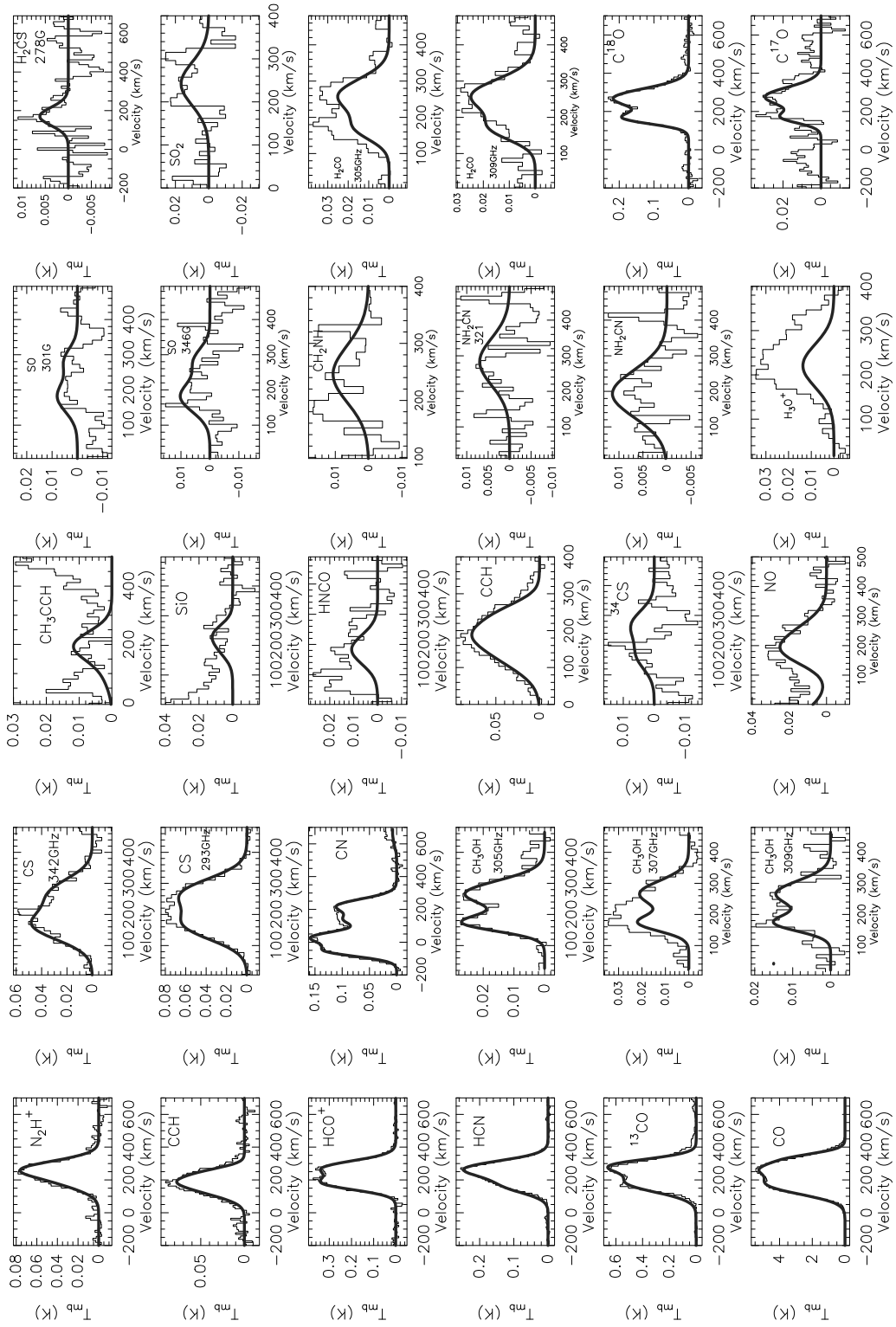

Figure 5.7: NGC 253 Fit of the most intense molecular lines founded in this survey.

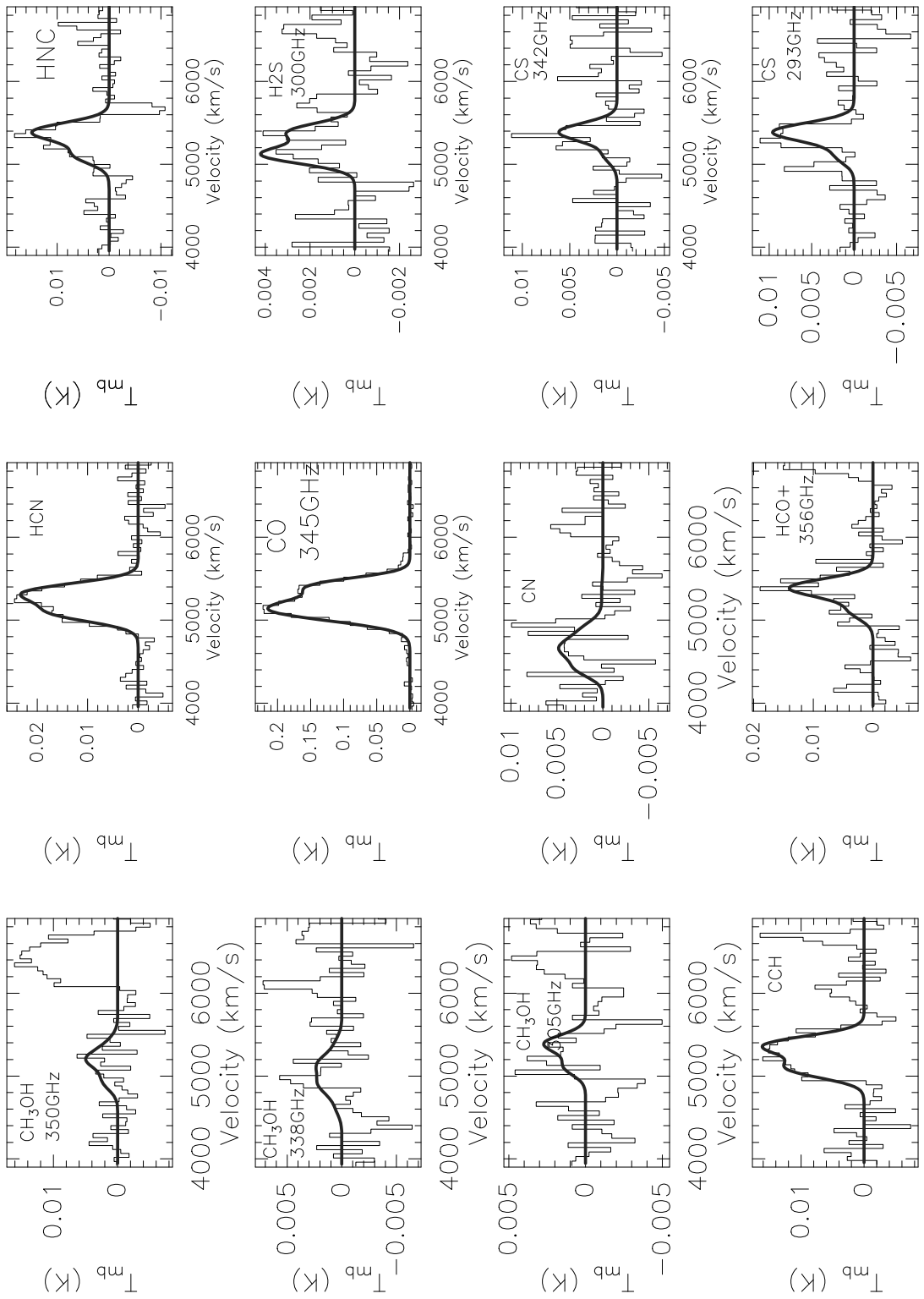
HNC
H2S 300GHz
CS 342GHz
CS 293GHz
HCN
CO 345GHz
CN
HCO+ 356GHz
CH3OH 350GHz
CH3OH 338GHz
CH3OH 305GHz
CCH
Tmb (K)
Velocity (km/s)

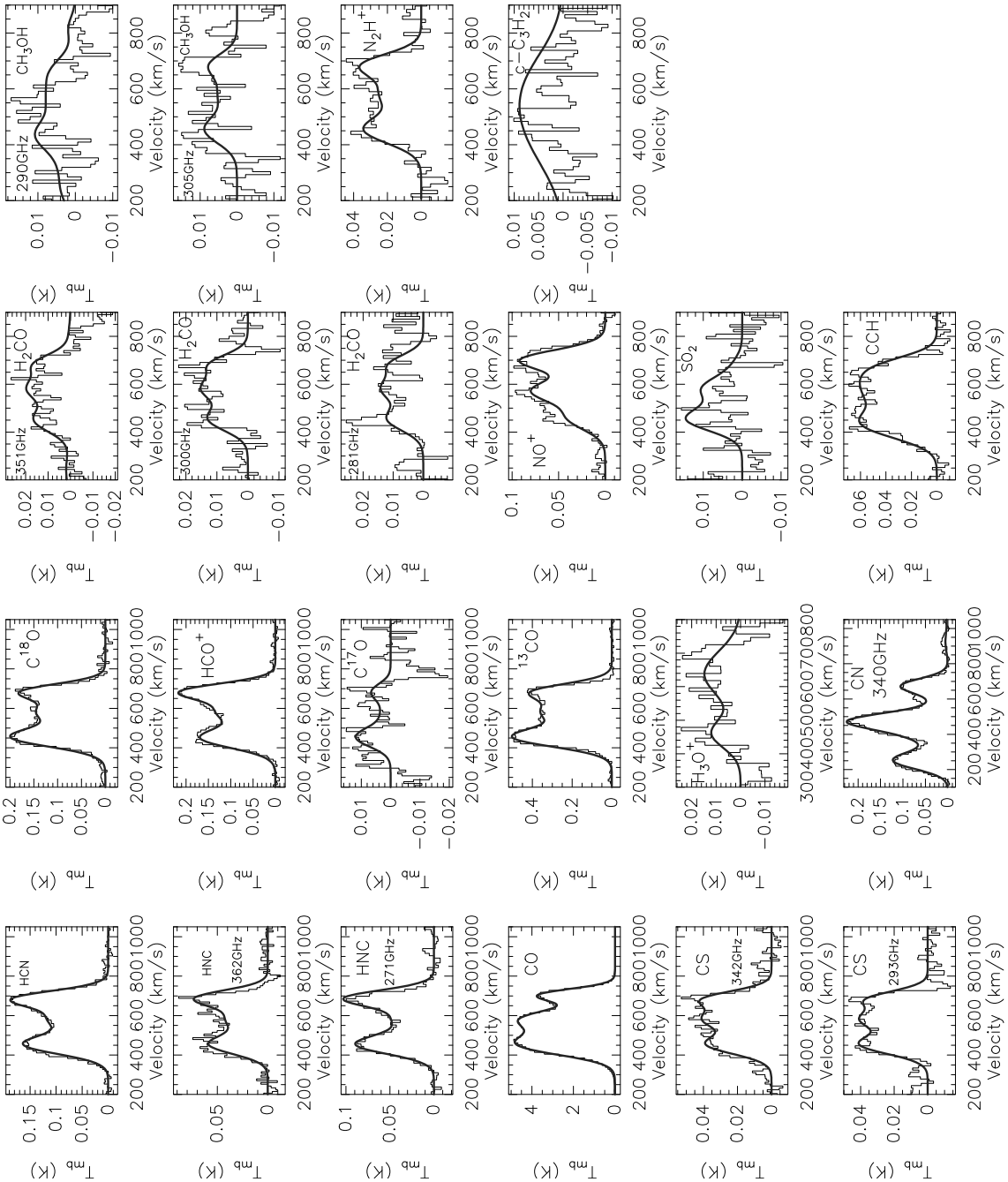

Figure 5.9: NGC 4945 Fit of the most intensity molecular lines founded in this survey.

*$C^{17}O$:The isotopologue has a low signal to noise because it is in the atmospheric region in Arp 220, the rms is 3.86x10^{-3}K. A Column density for NGC 253 and NGC 4945 of the order or 10^{15}cm^{-2}.

*N_2H^+: Diazenylium was observed in all galaxies. The most abundant amount of this molecule was in Arp 220, follow by NGC 4945 and NGC 253.

*CH_3OH: Methanol is present in all galaxies, is the molecule with 104 transitions (including hiperfine) in the spectra, there are three clear lines not blended that was used to fit H_3O^+ in all galaxies with any other lines .

*CO^+: The ion-molecule has a tentative detection only in Arp 220 with one velocity component, show two transitions J=3_3-2_2, J= 3_4-2_3 and has a column density of 6.69(1)X10^{13}cm^{-2}. An rms 3.05x10^{-3}K was obtained toward NGC 253, while for NGC 4945 we got 5.27 x10^{-3} and was measured from the most intense transition J=3_4-2_3.

*OCS: We found a tentative Carbonyl sulfide molecule in Arp 220 at 279GHz J=23-22, has other transition at 291GHz (J=24-23) but fall in a low transmision atmospheric area, The particular characteristic is that is neccesary a high temperature (98K) to excite it, also we fit 2 velocity components. The rms 4.6x10^{-3}K in NGC 253 and 5.3x10^{-3}K in NGC 4945.

*H_2S: We found Hidrogen sulfide molecule only in Arp 220, there are two transitions and one velocity component, one at 300GHz(J=$3_{3,0}$-$3_{2,1}$) and the second at 369GHz(J=$3_{2,1}$-$3_{1,2}$), the last one fall in atmospheric region, thus the column density fitted over the observed transition is 5.75(0.1)X10^{15}cm^{-2} . The rms in NGC 253 is 4.04x10^{-3}K and NGC 4945 is 5.50x10^{-3}K for J=$3_{3,0}$-$3_{2,1}$.

*$HNCO$: Isocyanic acid was detected in NGC 253 and NGC 4945. Three clear transitions were observed toward NGC 4945 at 285GHz (J=$13_{0,13}$-$12_{0,12}$), 307GHz(J=$14_{0,14}$-$13_{0,13}$) and 351GHz ($16_{0,16}$-$15_{0,15}$), while in NGC 253 at 351GHz was not detected, instead we detected 329GHz (J=$15_{0,15}$-$14_{0,14}$) The rms for Arp 220 is 4.25x10^{-3}K.

*CH_2NH: Methanimine was detected toward NGC 253 and NGC 4945, shows three transitions at 340GHz(J=$3_{1,3}$-$2_{0,2}$), 284GHz(J=$2_{1,2}$-$1_{0,1}$), and 317GHz (J=$5_{0,5}$-$4_{0,4}$); The rms for Arp 220 is 3.18x10^{-3}K.

*CH_3C_2H: We detect this molecule toward NGC 253 and NGC 4945, is blended with H_2CO in NGC 253 and we fit only one velocity component. The rms in Arp is 2.89x10^{-3}K for J=18_0-17_0 transition.

*H_2CO: We found Formaldehyde toward NGC 253 (7 transitions) and it is blended with methanol

and CH_3C_2H, while for NGC 4945 was detected in 10 transitions and it is blended with c-C_3H_2. The rms in Arp 220 is 3.25x10^{-3}K.

*H_2CS: Thioformaldehyde was detected only in NGC 253 with one velocity component in 14 transitions. The rms in Arp 220 IS 7.2x10^{-3}K, while 4.14x10^{-3}K for NGC 4945.

*NH_2CN: Cyanamide was detected only toward NGC 253, also, we fitted only 1 velocity component and 12 transitions . The rms in NGC 4945 is 3.68x10^{-3}K, while for Arp 220 is 3.23x10^{-3}K.

*SiO: The Silicon monoxide molecule was finded only in NGC 253 with a column density of 6.57(3)x10^{12}cm^{-2} , in the case of Arp 220 we found an rms of 3.15x10^{-3}K. The same situation happen with NGC 4945 with an rms of 8.23x10^{-3}K.

*SO: Sulfur monoxide was detected toward NGC 253 and NGC 4945 (blended with methanol). We fitted 10 transitions of SO toward NGC 253 and one velocity component, while 5 transitions in NGC 4945 in one component too. The rms for Arp 220 is 4.27x10^{-3}K.

*c-C_3H_2: Cyclopropenylidene molecule was detected only toward NGC 4945 in 28 transitions. An rms of 3.58x10^{-3}K was measured toward NGC 253, while for Arp 220 we obtain a rms noise of 3.37x10^{-3}K.

*NO: Nitric oxide was detected in NGC 253 and NGC 4945, we detected 8 hiperfine transitions and fitted in 1 velocity component for NGC 253 and three velocity components in NGC 4945. A rms of 3.73x10^{-3}K was found toward Arp 220.

*SO_2: Sulfur Dioxide was detected in NGC 253 and fitted with 1 component, also, detect in NGC 4945 but it is blended. An rms of 4.8x10^{-3}K was measured from Arp 220.

Molecule Transition	ν (MHz)	AREA (mK Km s^{-1})	$\Delta V_{1/2}$ (km s^{-1})	V_{LSR} (km s^{-1})	T_{MB} K	Log(N) (cm^{-2})
CO (3- 2)	345795.9899	685.130	136.12	182.67	4.231	17.912
CO (3- 2)	345795.9899	437.634	95.24	300.22	3.351	17.985
$C^{17}O$ (3- 2)	337061.1298	1.164	48.04	184.82	0.023	15.089
$C^{17}O$ (3- 2)	337061.1298	3.702	140.89	286.06	0.025	15.685
$C^{18}O$ (3- 2)	329330.5453	10.750	66.87	164.48	0.151	16.05
$C^{18}O$ (3- 2)	329330.5453	24.679	113.68	266.30	0.202	16.552
^{13}CO (3- 2)	330587.9601	61.758	122.29	186.72	0.469	16.84
^{13}CO (3- 2)	330587.9601	45.246	93.42	288.31	0.445	16.85
CS (6- 5)	293912.244	5.485	95.95	171.02	0.054	13.757
CS (6- 5)	293912.244	6.401	105.28	259.98	0.057	14.136
CS (7- 6)	342883	4.438	95.95	171.02	0.043	13.757
CS (7- 6)	342883	3.561	105.28	259.98	0.032	14.136
$C^{34}S$ (6- 5)	289209.23	0.875	95	214.34	0.009	12.860
$C^{34}S$ (6- 5)	289209.23	0.063	105	159.67	0.001	12.860

$C^{34}S$ (7- 6)	337396.6901	0.862	95	214.34	0.009	12.860
HCO^+, v=0 1 2 (4 0,0- 3 0,0)	356734.134	24.680	87.31	176.76	0.264	13.419
HCO^+, v=0 1 2 (4 0,0- 3 0,0)	356734.134	31.247	101.05	267.96	0.287	13.792
HCN 4- 3	354505.4759	11.561	96.75	171.98	0.112	13.314
HCN 4- 3	354505.4759	24.401	107.42	267.34	0.211	13.914
HNC 4- 3	362630.303	10.109	94.83	185.60	0.100	13.22
HNC 4- 3	362630.303	5.236	73.96	263.50	0.066	13.198
HNCO (13 0,13-12 0,12)	285722.0543	0.485	90	185.89	0.005	14.959
HNCO (14 0,14-13 0,13)	307694.0342	0.227	90	185.89	0.002	14.959
HNCO (15 0,15-14 0,14)	329664.535	0.112	90	185.89	0.001	14.959
SO_2 (6 4,2- 6 3,3)	357925.96	1.173	115	250.93	0.010	14.766
SO_2 (5 4,2- 5 3,3)	358013.09	1.200	115	250.93	0.010	14.766
SO_2 (4 4,0- 4 3,1)	358038.08	0.886	115	250.93	0.007	14.766
NO (4 -1,4- 3 1, 3)	350689.494	1.155	135.58	225.67	0.008	15.46
NO (4 1, 4- 3 -1, 3)	351043.524	1.155	135.58	225.67	0.008	15.46
SO (7 6- 6 5)	296550.045	0.602	100.90	181.09	0.006	13.832
SO (7 7- 6 6)	301286.124	0.535	100.90	181.09	0.005	13.832
SO (3 3- 2 3)	339341.459	0.142	84.61	283.08	0.002	14.072
CH_3OH (3 1-3 0) +	305473.491	0.818	62.30	172.13	0.012	14.118
CH_3OH (3 1-3 0) +	305473.491	1.544	98.39	266.02	0.015	14.335
CH_3OH (4 1-4 0) +	307165.924	0.771	62.30	172.13	0.012	14.118
CH_3OH (4 1-4 0) +	307165.924	1.345	98.39	266.02	0.013	14.335
CH_3OH (5 1-5 0) +	309290.36	0.639	62.30	172.13	0.010	14.118
CH_3OH (5 1-5 0) +	309290.36	1.010	98.39	266.02	0.010	14.335
CN v=0 1 (3 0,3- 2 0,2)	340031.544	2.727	74.88	168.87	0.034	13.957
CN v=0 1 (3 0,3- 2 0,2)	340031.544	5.296	100.93	254.55	0.049	14.407
CN v=0 1 (3 0,3- 2 0,2)	340035.408	3.343	100.93	254.55	0.031	14.407
SiO (7- 6)	303926.96	0.422	100	238	0.004	13.000
H_2CS (9 1,8- 8 1,7)	313714.9072	0.439	110.7	170	0.004	13.31
H_2CS (11 1,11-10 1,10)	371844.2411	0.546	110.7	170	0.005	13.31
CH_2NH (2 1,2- 1 0,1)	284254.2754	0.407	123.23	240.47	0.003	13.558
CH_2NH (3 1,3- 2 0,2)	340354.3146	0.520	123.23	240.47	0.004	13.558
CH_2NH (5 1,5- 4 1,4)	306172.4223	0.233	123.23	240.47	0.002	13.558
H_2CO (5 1,5- 4 1,4)	351768.645	1.121	68.67	172.97	0.015	13.01
H_2CO (5 0,5- 4 0,4)	362736.048	0.575	68.67	172.97	0.008	13.01
H_2CO (4 1,4- 3 1,3)	281526.929	2.057	112.85	291.73	0.017	13.59
H_2CO (4 0,4- 3 0,3)	290623.405	1.698	112.85	291.73	0.014	13.59
H_2CO (4 1,3- 3 1,2)	300836.635	1.008	68.67	172.97	0.014	13.01
CH_3CCH (17 0-16 0)	290502.0809	2.577	120.6	674.43	0.020	15.561
CH_3CCH (17 1-16 1)	290496.543	2.064	120.6	674.43	0.016	15.561
CH_3CCH (18 0-17 0)	307583.0459	1.977	120.6	674.43	0.015	15.561
CH_3CCH (17 2-16 2)	290479.9316	1.059	120.6	674.43	0.008	15.561
C_2H (4 5,5- 3 4,4)	349337.4558	2.870	112.37	182.98	0.024	14.34
C_2H (4 5,5- 3 4,4)	349337.4558	1.419	75.89	251.25	0.018	14.299
C_2H (4 5,4- 3 4,3)	349338.7284	2.294	112.37	182.98	0.019	14.34
C_2H (4 5,4- 3 4,3)	349338.7284	1.134	75.89	251.25	0.014	14.299
C_2H (4 4,4- 3 3,3)	349398.9061	2.249	112.37	182.98	0.019	14.34

C_2H (4 4,4- 3 3,3)	349398.9061	1.112	75.89	251.25	0.014	14.299
C_2H (4 4,3- 3 3,2)	349400.2918	1.678	112.37	182.98	0.014	14.34
NS v=0 (7- 1,7- 6 -1,6)	299699.781	0.184	180	200	0.001	13.500
NS v=0 (7 -1,7- 6 1,6)	300097.098	0.183	180	200	0.001	13.500
NS v=0 (7 -1,7- 6 1,6)	300098.611	0.156	180	200	0.001	13.500
NH_2CN (14 1,14-13 1,13)	278019.6584	0.750	148.43	283	0.005	13.746
NH_2CN (15 1,15-14 1,14)	297868.8474	0.494	148.43	283	0.003	13.746
NH_2CN (16 1,15-15 1,14)	321930.3198	0.292	148.43	283	0.002	13.746
OCS (23-22)	279685.318	2.248	200	250	0.011	14.69
OCS (24-23)	291839.673	2.291	200	250	0.011	14.69
N_2H^+ (3- 2)	279511.701	2.471	79.19	178.42	0.029	12.591
N_2H^+ (3- 2)	279511.701	6.944	107.99	263.12	0.060	13.04

Table 5.2: NGC 253 synthetic model.

Molecule Transition	ν (MHz)	AREA (mK Km s^{-1})	$\Delta V_{1/2}$ (km s^{-1})	V_{LSR} (km s^{-1})	T_{MB} K	Log(N) (cm^{-2})
CS (6- 5)	293912.244	4.298	114.671	237.74	0.035	13.504
CS (6- 5)	293912.244	4.325	118.895	482.681	0.034	13.482
CS (6- 5)	293912.244	2.984	97.142	673.215	0.029	13.295
CS (7- 6)	342883	4.115	114.671	237.74	0.034	13.504
CS (7- 6)	342883	4.391	118.895	482.681	0.035	13.482
CS (7- 6)	342883	3.411	97.142	673.215	0.033	13.295
CO (3- 2)	345795.9899	538.648	114.671	295.302	4.11	17.729
CO (3- 2)	345795.9899	549.111	120.306	515.999	4.045	17.727
CO (3- 2)	345795.9899	248.911	72.717	695.102	3.123	17.385
HNC (3- 2)	271981.142	9.524	114.671	217.714	0.078	13.397
HNC (3- 2)	271981.142	4.755	118.895	378.283	0.038	12.997
HNC (3- 2)	271981.142	9.031	97.142	647.645	0.087	13.35
HNC (4- 3)	362630.303	6.396	114.671	217.714	0.052	13.397
HNC (4- 3)	362630.303	4.405	118.895	378.283	0.035	12.997
HNC (4- 3)	362630.303	6.528	97.142	647.645	0.063	13.35
HCN (4- 3)	354505.4759	17.716	114.671	425.735	0.145	13.416
HCN (4- 3)	354505.4759	12.133	118.895	553.655	0.096	13.236
HCN (4- 3)	354505.4759	16.327	97.142	696.124	0.158	13.36
HCO^+, v=0 1 2 (4 0,0- 3 0,0)	356734.134	19.206	120	367.013	0.15	13.22
HCO^+, v=0 1 2 (4 0,0- 3 0,0)	356734.134	13.847	118.895	511.591	0.109	13.062
HCO^+, v=0 1 2 (4 0,0- 3 0,0)	356734.134	18.927	97.142	668.467	0.183	13.192
$C^{18}O$ (3- 2)	329330.5453	21.401	114.671	417.363	0.175	16.315
$C^{18}O$ (3- 2)	329330.5453	15.332	118.895	558.953	0.121	16.171
$C^{18}O$ (3- 2)	329330.5453	14.659	93.372086	698.444	0.147	16.18
$C^{17}O$ (3- 2)	337061.1298	2.518	114.671	454.137	0.021	15.365
$C^{17}O$ (3- 2)	337061.1298	1.487	118.895	581.643	0.012	15.137
$C^{17}O$ (3- 2)	337061.1298	1.601	97.142	684.78	0.015	15.195
^{13}CO (3- 2)	330587.9601	54.238	114.671	358.576	0.441	16.719

^{13}CO (3- 2)	330587.9601	37.67	118.895	522.507	0.296	16.56
^{13}CO (3- 2)	330587.9601	34.541	97.142	688.879	0.333	16.55
SiO (7- 6)	303926.96	0.728	200	548.9928	0.0034	12.38
SiO (8- 7)	347330.631	0.679	200	548.9928	0.0032	12.38
CN v=0 1 (3 0,4- 2 0,3)	340247.77	4.112	114.671	378.288	0.0337	14.089
CN v=0 1 (3 0,4- 2 0,3)	340247.77	1.59	118.895	431.607	0.0126	13.676
CN v=0 1 (3 0,4- 2 0,3)	340247.77	4.205	97.142	691.905	0.0407	14.124
CN v=0 1 (3 0,3- 2 0,2)	340031.544	4.171	114.671	378.288	0.0342	14.089
CN v=0 1 (3 0,3- 2 0,2)	340031.544	1.613	118.895	431.607	0.0127	13.676
CN v=0 1 (3 0,3- 2 0,2)	340031.544	4.264	97.142	691.905	0.0412	14.124
CN v=0 1 (3 0,4- 2 0,3)	340248.5764	2.985	114.671	378.288	0.0244	14.089
CN v=0 1 (3 0,4- 2 0,3	340248.5764	1.154	118.895	431.607	0.0091	13.676
CN v=0 1 (3 0,4- 2 0,3)	340248.5764	3.052	97.142	691.905	0.0295	14.124
SO_2 (5 3,3- 4 2,2)	351257.224	1.585	114.671	635.66	0.013	14.1
SO_2 (6 3,3- 5 2,4)	371172.452	1.569	114.671	635.66	0.0129	14.1
SO_2 (3 3,1- 2 2,0)	313279.7183	1.478	114.671	635.66	0.0121	14.1
H_2CO (5 1,5- 4 1,4)	351768.645	1.511	114.671	377.44	0.0124	13.101
H_2CO (5 1,5- 4 1,4)	351768.645	1.914	118.895	537.42	0.0151	13.187
H_2CO (5 1,5- 4 1,4)	351768.645	1.324	97.142	716.22	0.0128	13.026
H_2CO (4 1,3- 3 1,2)	300836.635	1.354	114.671	377.44	0.0111	13.101
H_2CO (4 1,3- 3 1,2)	300836.635	1.629	118.895	537.42	0.0129	13.187
H_2CO (4 1,3- 3 1,2)	300836.635	1.014	97.142	716.22	0.0098	13.026
H_2CO (4 1,4- 3 1,3)	281526.929	1.261	114.671	377.44	0.0103	13.101
H_2CO (4 1,4- 3 1,3)	281526.929	1.505	118.895	537.42	0.0119	13.187
H_2CO (4 1,4- 3 1,3)	281526.929	0.922	97.142	716.22	0.0089	13.026
SO (7 6- 6 5)	296550.045	0.587	200	418.885	0.0028	13.868
SO (7 7- 6 6)	301286.124	0.507	200	418.885	0.0024	13.868
SO (7 8- 6 7)	304077.844	0.978	200	418.885	0.0046	13.868
C_2H (4 5, 5- 3 4,4)	349337.4558	2.237	114.671	454.137	0.0183	14.188
C_2H (4 5, 5- 3 4,4)	349337.4558	2.054	118.895	581.643	0.0162	14.137
C_2H (4 5, 4- 3 4,3)	349338.7284	1.788	114.671	454.137	0.0146	14.188
C_2H (4 5, 4- 3 4,3)	349338.7284	1.281	97.142	684.78	0.0124	14.026
C_2H (4 4, 4- 3 3,3)	349398.9061	1.61	118.895	581.643	0.0127	14.137
C_2H (4 4, 4- 3 3,3)	349398.9061	1.256	97.142	684.78	0.0121	14.026
c-C_3H_2 (8 1,8- 7 0,7)	284805.2056	1.444	300	621.094	0.0045	13.418
c-C_3H_2 (5 5,0- 4 4,1)	349263.9776	1.638	300	621.094	0.0051	13.418
c-C_3H_2 (7 1,6- 6 2,5)	284998.0002	1.162	300	621.094	0.0036	13.418
N_2H^+ (3- 2)	279511.701	3.496	114.671	454.137	0.0286	12.736
N_2H^+ (3- 2)	279511.701	3.347	118.895	581.643	0.0264	12.718
N_2H^+ (3- 2)	279511.701	2.941	97.142	684.78	0.0284	12.662
N_2H^+ (4- 3)	372672.509	3.296	114.671	454.137	0.027	12.736
N_2H^+ (4- 3)	372672.509	3.156	118.895	581.643	0.0249	12.718
N_2H^+ (4- 3)	372672.509	2.773	97.142	684.78	0.0268	12.662
CH_3OH (2 1-2 0)	304208.348	1.252	114.671	454.137	0.0103	14.059
CH_3OH (3 1-3 0	305473.491	0.949	114.671	454.137	0.0078	14.059
CH_3OH (4 1-4 0)	307165.924	0.77	114.671	454.137	0.0063	14.059
CH_3OH (5 1-5 0)	309290.36	0.529	114.671	454.137	0.0043	14.059

CH_3OH (1 1-0 0)	350905.1	1.302	114.671	454.137	0.0107	14.059
CH_3OH (1 1-0 0)	350905.1	0.736	118.895	581.643	0.0058	13.811
CH_3OH (1 1-0 0)	350905.1	0.915	97.142	684.78	0.0088	13.906
CH_3OH (3 1-3 0)	305473.491	0.949	114.671	454.137	0.0078	14.059
HNCO (13 0,13-12 0,12)	285721.951	0.576	114.671	454.137	0.0047	13.675
HNCO (13 0,13-12 0,12)	285721.951	1.491	118.895	581.643	0.0118	14.015
HNCO (13 0,13-12 0,12)	285721.951	0.678	97.142	684.78	0.0066	13.566
HNCO (14 0,14-13 0,13)	307693.905	0.458	114.671	454.137	0.0037	13.675
HNCO (14 0,14-13 0,13)	307693.905	1.247	118.895	581.643	0.0099	14.015
HNCO (14 0,14-13 0,13)	307693.905	0.631	97.142	684.78	0.0061	13.566
HNCO (16 0,16-15 0,15)	351633.257	0.246	114.671	454.137	0.002	13.675
HNCO (16 0,16-15 0,15)	351633.257	0.753	118.895	581.643	0.0059	14.015
HNCO (16 0,16-15 0,15)	351633.257	0.482	97.142	684.78	0.0047	13.566
NO (4 -1,4- 3 1,3)	350689.494	0.219	112	600	0.0018	14.69
NO (4 -1,4- 3 1,3)	350689.494	0.169	114	700	0.0014	14.6
NO (4 1,4- 3 -1,3)	351043.524	0.219	112	600	0.0018	14.69
NO (4 1,4- 3 -1,3)	351043.524	0.169	114	700	0.0014	14.6
OCS 23-22	279685.318 1.911	483	669	0.0037	15.46	
OCS 24-23	291839.673 1.467	483	669	0.0029	15.46	

Table 5.3: NGC 4945 synthetic model.

Molecule Transition	ν (MHz)	AREA (mK Km s^{-1})	$\Delta V_{1/2}$ (km s^{-1})	V_{LSR} (km s^{-1})	T_{MB} K	Log(N) (cm^{-2})
HCN (4- 3)	354505.4759	5.33904	250	5092.5117	0.0193	14.865
HCN (4- 3)	354505.4759	5.60592	249.368	5332.5654	0.0203	14.889
C_2H (4 5,5- 3 4,4)	349337.4558	0.95343	250	5116	0.0036	15.763
C_2H (4 5,5- 3 4,4)	349337.4558	1.39878	250	5390	0.0052	15.933
C_2H (4 5,4- 3 4,3)	349338.7284	0.76368	250	5116	0.0029	15.763
C_2H (4 5,4- 3 4,3)	349338.7284	1.1216	250	5390	0.0042	15.933
C_2H (4 4,4- 3 3,3)	349398.9061	0.74865	250	5116	0.0028	15.763
C_2H (4 4,4- 3 3,3)	349398.9061	1.09961	250	5390	0.0041	15.933
C_2H (4 4,3- 3 3,2)	349400.2918	0.55967	250	5116	0.0021	15.763
C_2H (4 4,3- 3 3,2)	349400.2918	0.82293	250	5390	0.0031	15.933
CN v=0,1 (3 0,3-2,0 2)	340031.544	0.33466	250	5390	0.0013	14.81
CN v=0,1 (3 0,3-2,0 2)	340035.408	0.21125	250	5390	0.0008	14.81
CN v=0,1 (3 0,4-2 0,3)	340247.77	0.32969	250	5390	0.0012	14.81
CN v=0,1 (3 0,4-2 0,3)	340247.77	0.44782	250	5390	0.0017	14.81
CN v=0,1 (3 0,4-2 0,3)	340248.5764	0.23954	250	5390	0.0009	14.81
CS (6- 5)	293912.244	0.46807	250	5116	0.0018	14.664
CS (6- 5)	293912.244	2.15568	250	5390	0.0079	15.34
CS (7- 6)	342883	0.29071	250	5116	0.0011	14.664
CS (7- 6)	342883	1.35646	250	5390	0.005	15.34
HCO^+v=0,1,2 (4 0,0- 3 0,0)	356734.134	1.53897	250	5116	0.0057	14.075
HCO^+v=0,1,2 (4 0,0- 3 0,0)	356734.134	3.84301	250	5390	0.0141	14.485

HNC (4- 3)	362630.303	2.0746	250	5116	0.0077	14.411
HNC (4- 3)	362630.303	7.68349	250	5390	0.0274	15.01
OCS (23-22)	279685.318	1.52781	250	5230	0.0057	16.161
OCS (23-22)	279685.318	3.54816	250	5540	0.0133	16.53
OCS (24-23)	291839.673	1.65088	250	5230	0.0062	16.161
OCS (24-23)	291839.673	3.82208	250	5540	0.0143	16.53
H_2S (3 3,0- 3 2,1)	300505.56	1.12236	250	5116	0.0042	15.76
H_2S (3 3,0- 3 2,1)	300505.56	1.1203	250	5390	0.0042	15.76
H_2S (3 2,1- 3 1,2)	369101.45	2.48542	250	5116	0.0093	15.76
H_2S (3 2,1- 3 1,2)	369101.45	2.48086	250	5390	0.0093	15.76
CH_3OH (2 1- 2 0)	304208.348	0.48682	250	5116	0.0018	15.32
CH_3OH (2 1 - 2 0)	304208.348	0.94126	250	5390	0.0035	15.609
CH_3OH (3 1 - 3 0)	305473.491	0.37053	250	5116	0.0014	15.32
CH_3OH (3 1 - 3 0)	305473.491	0.71716	250	5390	0.0027	15.609
CH_3OH (4 1 - 4 0)	307165.924	0.30223	250	5116	0.0011	15.32
CH_3OH (4 1 - 4 0)	307165.924	0.58534	250	5390	0.0022	15.609
CH_3OH (5 1 - 5 0)	309290.36	0.20918	250	5116	0.0008	15.32
CH_3OH (5 1 - 5 0)	309290.36	0.40545	250	5390	0.0015	15.609
CH_3OH (1 1 - 0 0)	350905.1	0.57932	250	5116	0.0022	15.32
CH_3OH (1 1 - 0 0)	350905.1	1.12033	250	5390	0.0042	15.609
CO (3- 2)	345795.9899	66.93822	299.18	5138	0.1958	17.87
CO (3- 2)	345795.9899	29.47334	213.915	5420	0.1241	17.493
CO^+ (3 3- 2 2)	353741.262	0.19873	205	5380	0.0009	13.625
CO^+ (3 4- 2 3)	354014.247	0.28389	205	5380	0.0013	13.625
SiO (7- 6)	303926.96	0.98022	363	5350	0.0025	14.79
SiO (8- 7)	347330.631	0.55342	363	5350	0.0014	14.79
$C^{34}S$ (6- 5)	289209.23	0.79481	450	5350	0.0017	14.9
$C^{34}S$ (7- 6)	337396.6901	0.50251	450	5350	0.001	14.9
N_2H^+ v=0, (3- 2)	279511.7348	7.97901	519.35693	5353	0.0139	14.86
N_2H^+ v=0, (4- 3)	372672.4645	7.8416	519.35693	5353	0.0138	14.86

Table 5.4: Arp 220 synthetic model.

5.3 Ratios

5.3.1 Isotopic ratios

In this section we show some ratios for discusion and explain about the interpretation.

In Table 5.2, we derived 12C/13C, 32S/34S, 16O/18O and 18O/17O isotopic ratios for Arp 220, NGC 4945 and NGC 253 by using molecular column densities ratios. For comparison typical isotopic ratios for the Galactic Center (GC) are also included in Table 5.3. As seen in Table 5.2 The 12C/13C ratios for galaxies ranges from ∼11 to ∼15, which are much lower than the

Table 5.1: Column densities and abundances from fits to the observed sources: For Arp 220: the value for H_2 is 2.1x10^{22}; For NGC4945 The value for H_2 is 8.24x10^{22}; the value for NGC 253 is 9.58x10^{22}, N(H_2) assuming a H_2/CO ratio of 10^{-4} from Martin et al. (2011) and Harrison et al. (1999). Molecules with * mark in the column density are tentative detections, for more details see section 4.1. The species not detected in one galaxy we put ..., instead we obtain the rms for each of them and it is described in the details for each molecule

Source	Arp 220		NGC 4945		NGC 253	
Molecule	N(cm^{-2})	[X]/[H_2]	N (cm^{-2})	[X]/[H_2]	[N (cm^{-2})	[X]/[H_2]
HCN	1.50(0.081)x10^{15}	1.81x10^{-8}	5.41(0.20)x10^{13}	7.93x10^{-10}	1.016(0.015)x10^{13}	1.06x10^{-9}
C_2H	1.43(0.22)x10^{16}	6.84x10^{-7}	2.89(1.15)x10^{14}	3.52x10^{-9}	4.11(0.94)x10^{14}	4.29x10^{-9}
CN	7.45(3.9)x10^{14}	3.55x10^{-8}	2.96(0.24)x10^{14}	3.61x10^{-9}	2.93(0.088)x10^{14}	3.06x10^{-9}
^{13}CN	*6.22(2.53)X10^{14}	7.54x10^{-9}	...	...	...	...
CS	2.56(0.62)x10^{15}	1.26x10^{-7}	6.05(1.54)x10^{13}	7.36x10^{-10}	2.038(0.062)x10^{14}	2.13x10^{-9}
$C^{34}S$	4.4(3)x10^{14}	2.12x10^{-8}	2.41(1.5)^{12}	2.9x10^{-11}	1.88(0.62)x10^{13}	1.95x10^{-10}
^{13}CS	...	...	...	...	1.34(0.25)x10^{13}	1.4x10^{-10}
HCO^+	4.23(0.74)x10^{14}	2.0x10^{-8}	4.3(0.15)x10^{13}	5.28x10^{-10}	8.73(0.14)x10^{13}	9.11x10^{-10}
HNC	1.25(0.16)X10^{15}	6.1X10^{-8}	5.41(0.24)x10^{13}	6.56x10^{-10}	3.24(0.18)x10^{13}	3.39x10^{-10}
CO	1.37(0.026)X10^{18}	6.53X10^{-5}	1.3(0.029)x10^{18}	1.57x10^{-5}	1.76(0.041)x10^{18}	1.84x10^{-5}
^{13}CO	...	...	1.21(0.1)X10^{17}	1.45x10^{-6}	1.43(0.035)x10^{17}	1.50x10^{-6}
$C^{18}O$	...	...	5.11(0.21)X10^{16}	6.22x10^{-7}	5(0.094)X10^{16}	5.22x10^{-7}
$C^{17}O$	...	...	5.24(1.07)X10^{15}	6.37x10^{-8}	6.48(0.682)X10^{15}	6.77x10^{-8}
N_2H^+	1.84(0.46)x10^{14}	8.37x10^{-9}	1.56(0.13)x10^{13}	1.88x10^{-10}	1.50(0.121)X10^{13}	1.57x10^{-10}
CH_3NH_2	2.21(0.583)X10^{16}	1.05x10^{-6}	...	...	...	...
CH_3OH	6.15(1.90)x10^{15}	7.46x10^{-8}	2.08(0.72)x10^{14}	2.51x10^{-9}	4.23(0.995)x10^{14}	4.41x10^{-9}
CO^+	*6.69(1)X10^{13}	3.18x10^{-9}	...	...	...	...
OCS	*4.8(0.7)x10^{16}	2.30X10^{-6}	...	...	...	...
H_2S	*5.75(0.1)X10^{15}	2.47X10^{-7}	...	...	...	...
HNCO	...	...	1.876(0.57)X10^{14}	2.27X10^{-9}	1.822(0.24)X10^{15}	1.90x10^{-8}
CH_2NH	...	...	3.89(1)X10^{13}	5.8x10^{-10}	9.77(1.40)X10^{13}	1.02x10^{-9}
CH_3C_2H	...	...	7.19(3.74)X10^{13}	8.7x10^{-9}	2.93(1.39)X10^{16}	3.06x10^{-7}
H_2CO	...	...	3(1.14)X10^{13}	3.6x10^{-10}	4.56(0.29)X10^{13}	4.77x10^{-10}
H_2CS	*...	...	...	...	1.21(0.54)X10^{14}	1.17x10^{-9}
NH_2CN	*...	...	...	...	4.32(0.4)X10^{13}	4.51x10^{-10}
SiO	...	...	...	...	6.57(3)X10^{12}	6.86x10^{-11}
SO	...	...	7.38(1)X10^{13}	8.95x10^{-10}	4.92(1.5)X10^{13}	5.13x10^{-10}
c-C_3H_2	...	...	1.95(0.66)X10^{13}	2.39x10^{-10}	...	...
NO	...	...	...	...	1.47(0.38)X10^{15}	1.54x10^{-8}
SO_2	...	...	2.57(0.01)x10^{14}	3.84x10^{-9}	1.86(0.562)x10^{14}	1.94x10^{-9}

12C/13C ratio of more than 81 and ∼50 found in NGC 253 (Martin et al. 2010) and NGC 4945 (Henkel and Mauersberger 1993, Henkel et al. 1994), indicating that lines from main

Table 5.5: Ratios between molecules

Molecular radio	NGC 4945	NGC 253	Arp220
$CH_3OH/C^{18}O$	$4x10^{-3}$	$8.4x10^{-3}$	
$SiO/C^{18}O$		$1.3X10^{-4}$	
$CH_3CCH/C^{18}O$	$1.4x10^{-2}$	$5.8x10^{-1}$	
$SO/C^{18}O$	$1.4x10^{-3}$	$9.8x10^{-4}$	
c-$C_3H_2/C^{18}O$	$3.82x10^{-4}$		
$C_2H/C^{18}O$	$5.6x10^{-3}$	$8.2x10^{-3}$	
$N_2H^+/C^{18}O$	$3.05x10^{-4}$	$3.0x10^{-4}$	
$HNC/C^{18}O$	$1x10^{-3}$	$6.4x10^{-4}$	
$HCN/C^{18}O$	$1.2x10^{-3}$	$2x10^{-3}$	
$CN/C^{18}O$	$5.7x10^{-3}$	$5.8x10^{-3}$	
HCN/HCO^+	1.504	1.16	3.56
CN/HCN	4.53	2.88	0.753
HCN/CS	1.079	$4.9x10^{-1}$	0.58
$HNCO/C^{18}O$		$3.6x10^{-2}$	
$^{12}C/^{13}C$	10.69	12.32	
$^{12}C/^{18}C$	25.4	35.3	
$^{32}CS/^{34}CS$		10.91	5.81
$CN/^{13}CN$			1.38
CO^+/HCO^+			0.158

isotopologues are optically thick. In our study, we also found 16O/18O ratios of 118.4 (10.9) for NGC 4945 and of ¿232 for NGC 253. These ratios are likely strongly affected by opacity effects in the 13CO lines. On the other hand, the 32S/34S ratio of ¿58 and 18O/17O ratio of 7.7 (0.8) found in NGC 253, and the 18O/17O ratio of 9.8 (2.9) toward NGC 4945 probably less affected by optical depth effects since in their estimations we used the less abundant species 13CS, C34S, C18O and C17O.

Isotopic ratios can be used to estimate the degree of gas processing since usually there is a relation of primary to secondary products of nucleosynthesis (Wilson and Rood et 1994). As seen in Table 5.3 the 32S/34S ratio found in NGC 253 is a factor of ∼3 higher than that in the GC. In addition the 18O/17O ratios in NGC 4945 and NGC 253 are also factors of 2.4-3 higher compared to that of the GC. The differences in the 32S/34S and 18O/17O ratios between the GC and the starburst galaxies NGC 4945 and NGC 253 suggest that the gas is less processed in the latter than in the GC, consistent with previous studies (Martin et al. 2010, Armijos-Abendaño et al. 2015). The high 18O/17O ratios in the galaxies NGC 4945 and NGC 253 with material less processed compared with the GC gas are also consistent with the suggestion that 17O has more representative products than 18O in stellar nucleosynthesis (Wilson and Rood 1994).

Table 5.6: Isotopic ratios between molecules and comparation of Galactic Center. *Ratio derived by using the 12C/13C more than 81 ratio for NGC 253 from Martin et al. (2010) and the 12C/13C 50 for NGC 4945 from Henkel et al. (1994)

Isotopic ratio	Molecular column Density ratio	Arp220	NGC 4945	NGC 253	GC
	CN/13CN	0.9 0.6	...	...	
12C/13C	CS/13CS	...	...	15.2 2.9	20
	CO/13CO	...	10.7 0.9	12.3 0.4	
32S/34S	13CS/C34S	...	...	57.7	22
16O/18O	13CO/C18O		118.4 10.9	231.7	250
18O/17O	C18O/C17O	...	9.8 2.0	7.7 0.8	3.2 0.2

5.3.2 Molecular abundance ratios

Table past shows the derived molecular abundances relative to that of C18O for the tree galaxies. Unfortunately we have not detected C18O in Arp 220. We used C18O since it is an opically thin tracer and its column density would be a direct measure of the total molecular column density. We can see that basically all the abundace ratios are very similar, whtin a factor of 3, between NGC253 and NGC4949. For those molecules that have been detected in Arp 220, we find that the abundance ratios in this source show larger variations relative to the other galaxies.

Since this is the first spectral line survey of NGC4945, our results suggest a simimilar chemistry to that found in NGC253. From the chemical complexity observed in NGC253 it has been proposed (Sergio et al. 2006, **?**) the this galaxy is a starburst in an intermidate stage of evolution. This would indicate that the chemistry and to large extent also the heating in NGC4945 is dominated by the starburst with little influence of the AGN.

This results is somewhat in contradiction with the conclusion of the previous chapter derived from the abundance of H_3O^+, which was considered to be dominated by the AGN. Very likely the H_3O^+ emission arises from a different region that the other molecules detected in the survey. A posible scenrario would be that while H_3O^+ is mainly concetrated around the black hole, the other molecules are extended over a larger region where star formation is taken place. This is supported by the excitation of the H_3O^+ in low density gas. High angular resolution observation of key molecules like H_3O^+, SiO, HNCO, with ALMA will confirm the different spatial distribution of the AGN and starburst tracers.

The difference between the molecular abundance ratios between the ULIRG Arp200 and the starburst galaxies in our sample migh be due to the higher density gas in Arp 220 which makes the excitation of high dipole moments easier at 345 GHz the this galaxy than in the other two galaxies.

5.3.3 Excitation of the molecular gas. H2 densities

For NGC253 and NGC4945 we have detected several transitions of CS and CH3OH, which allow carrying out excitation studies from this high density, traces. To derive the H2 densities required for explaining the derived excitation temperature for these molecules. like for H_3O^+, we have used the non-LTE RDADEX code for collisional excitation. We have used a kinetic temperature of 120 K for NGC253 (Aladro et al. 2010) and 100 K (Wang et al 2004).

For NGC253 we found that a H2 density of 10^6 cm^{-3} will explain the observed line ratios (Tex of 15-23 K). This density is similar to that derived by Aladro et al (2010) for the high density component using the J=2-3 and J=5-4 line. Since the J=6-5 and J=7-6 lines have critical densities larger than that of the J=5-4 line by of factor of 10, this would indicate that any component with larger H2 density will have a very low column density. This suggests that H2 density of the bulk of the molecular clouds is basically dominated by gas with densities below few 10^6 cm^{-3}.

For NGC4945 we found that a H2 density of 10^6 cm^{-3} will explain the observed line ratios (Tex of 30-50 K). This density is more tan one order of magnitude of that derived by Wang et al (2004) from the J=2-3 and J=5-4 line. The larger H2 densities derived from the J=6-5 and J=7-6 are expected due to the larger critical densities of these lines than the J=5-4 lines.

Although the derived H2 densities in both starburst galaxies are very similar, the trends of the derived densities as a function of the quantum numbers of the transitions are different. For NGC253, the data suggest that density cores with H2 densities larger the 10^6 cm^{-2} will have low column densities. This might no be the case for NGC4945 for which clumps with larger H2 densities can still significantly contribute to the total column densities. Observation of higher J lines of CS will allow establishing the presence of a significant very high-density core tin both galaxies. The presence of such high-density cores would indicate the evolutionary state of the star formation processes in the starburst. The lack of very high-density cores in NGC345 is consistent with the scenario of an relatively evolved starburst, started to be dominated by the feedback of the star formation. NGC4549 might still be in an early stage, in the process of forming new stars.

5.4 Comparation with other frequencies: Line identification.

The molecules detected in this survey and in previous surveys (2mm and 3mm) were detected in this range (1mm) except H_3O^+, 5 in NGC4945 and 4 molecules for Arp220, probably the physical conditions do not excite this transitions.

Table 5.7: Comparations for the detected molecules in each galaxy 2mm and 3mm. 1) Martin et al. (2006); 2) Wang et al. (2004); 3)Martin et al (2011); 4)Aladro et al. (2015); 5) Present work at 0.8 mm. The detected molecules are marked with V, The boldface mean molecule only in this survey.

Molecule	NGC253 (4) 3mm	NGC 253 (1) 2mm	NGC 253 (5) 1mm	NGC4945 (2) 3mm	NGC4945 (2) 2mm	NGC4945 (2) 1.3mm	NGC4945 (5)1mm	Arp220 (4) 3mm	Arp220 (3) 1.3mm	Arp220 (5) 1mm
CO	V		V	V		V	V	V	V	V
^{13}CO	V		V	V		V	V	V	V	
C^{17}O	V		V	V		V	V			
C^{18}O	V			V		V	V	V	V	
CS	V	V	V	V	V	V	V	V		
C^{34}S	V	V	V		V		V	V	V	V
^{13}CS	V		V		V			V	V	
CN	V		V	V		V	V	V	V	V
^{13}CN	V			V						V
NS	V								V	
NO		V	V				V			
SO	V	V	V	V	V	V	V		V	
^{34}SO									V	
SiO	V	V	V					V	V	
^{29}SiO									V	
CO$^+$									V	V
H$_3$O$^+$			V				V			V
N$_2$H$^+$	V		V	V			V	V		V
C$_2$S	V	V								
HCN	V	V	V	V		V	V	V		V
H^{13}CN	V			V		V				
HC^{15}N				V						
HNC	V	V	V	V			V	V		V
HN^{13}C	V			V				V		
HCO	V			V						
OCS	V	V	V		V					V
C$_2$H	V	V	V	V			V	V		V
H$_2$S		V	V						V	V
SO$_2$	V	V	V				V			
DNC		V			V					
HCO$^+$	V	V	V	V		V	V	V		V
H^{13}CO$^+$	V			V				V		
HOC$^+$	V		V							
N$_2$D$^+$		V								
HNCO	V	V	V	V	V	V	V	V	V	
HOCO$^+$	V	V								
H$_2$CO		V	V		V	V	V		V	
H$_2$CS	V	V	V							
NH$_2$CN	V	V	V							
HC$_3$N	V	V		V	V	V		V	V	
CH$_2$NH		V	V				V			
H^{13}C$_3$N									V	
C$_3$H$_2$	V	V		V	V		V		V	
HC$_5$N	V									
CH$_3$OH	V	V	V	V	V	V	V	V	V	V
HC^{18}O$^+$	V		V							
CH$_3$CN	V	V			V			V	V	
^{13}CH$_3$CN									V	
CH$_3$CCH	V	V	V		V		V	V	V	
CH$_3$CHO	V									

Chapter

6 Detection of a new Molecular ion in the Extragalactic Medium:$HCNH^+$

One of the potential of spectral line surveys is the serendipity detection of molecules. In this chapter we present the tentative detection, for the first time, of the molecular ion HCNH+ in a galaxy, NGC4945.

6.0.1 Introduction. $HCNH^+$ in the Interstellar Medium

The $HCNH^+$ spectrum was first measured in the laboratory (Altman et al.1984a, 1984b) by infrared spectroscopy, and later its pure rotational spectroscopy was published by Bogey et al. (1985). Subsequently, Ziurys and Turner et. al (1986) detected $HCNH^+$ (protonated HCN), for the first time, in the interstellar medium of the Galaxy toward Sgr B2. They detected the J = 1-0, 2-1, and 3-2 rotational transitions of this species. Using a large velocity gradient (LVG) code, they derived a column density of $HCNH^+$ of about 4×10^{14} cm^{-2}, yielding an abundance of 3×10^{-10}. This high abundance was surprising, since it is several orders of magnitude greater than the values predicted by ion-molecule models of interstellar chemistry. The high observed abundance of this species, relative to theoretical calculations, suggests that the destruction of $HCNH^+$ by dissociative recombination is slower than expected, or that the formation rate of the ion has been underestimated.

6.1 The origin of HNC overabundance: The $HCNH^+$ precursor.

The HNC/HCN abundance ratio in cold dark clouds is usually larger than 1, it is 1.55 in TMC-1 (Irvine and Schloerb 1984) and even 4.4 in L134 (Wootten et al. 1978). This is contrast with the low ratios measure in warm and hot regions. In Orion-KL the ratio is 0.012, 0.2 in L1498 (Schilke et al. 1992), and 0.45 in L1521E (Hirota et al. 1998). These results indicate a strong temperature dependence of the HNC/HCN abundance ratio (Semaniak 2001). The most likely hypotheses suggests that an unusually high HNC abundance in interstellar medium can be produced through dissociative electron recombination of $HCNH^+$, which is considered as the

precursor of both HNC and HCN (Watson 1974). Such hypotheses has been confirmed by the quantum mechanical calculations (Keisaku Ishii et al 2006).

6.2 First tentative detection of HCNH$^+$ in the extragalactic ISM

Our spectral survey contains two transitions of HCNH$^+$, one, the J=4-3, at 296 GHz and the other, J=5-4, at 370 GHz. We have searched for these transitions in our surveys and found a very tentative detection only in NGC4945 right at the sensitivity level. This is consistent with the sensitivity achieved in our surveys and the results from previous line surveys at mm wavelengths of NGC253 and Arp 220. Unfortunately, the transition at 370GHz is in the atmospheric region with low transmission, making very difficult any confirmation of this weak line. To confirm the presence of the spectral feature at the frequency of the HCNH$^+$ 296 GHz line, we decided to make a more sensitive observation with APEX. We observed this line with much better sensitivity in September 2014. Fig. 6.1 show the final profile obtained after averaging all data. The line is clearly detected but the derived radial velocity is blushifted and the linewidth is broader compared with all other species measured in this galaxy (see chapter 5).
However, there is a line of SO which marginally overlaps with the HCNH$^+$ line. Based on the fit to the other transitions of this species detected in the survey, in the upper left panel of Fig. 6.2 we show the simulated LTE spectrum of the SO line superimposed on the observed profile. In the upper right panel, the simulated LTE spectrum of the HCNH$^+$ line is shown, This time the velocity and linewidth of the line profile is consistent with all other molecular species in this galaxy. The lower middle panel of 6.2 show that the combination of the LTE simulated spectra of both molecules nicely fits the observed profile.
Though the identification needs to be confirmed at other frequencies, the correct line profile after subtraction of the SO contamination strongly supports the identification.

6.3 Column densities and abundance

From the LTE simulation and the rms noise of the 370GHz transition (4.9×10^{-3} K) we set an upper limit to the excitation temperature of 35 K, consistent with those derived from other molecules in chapter 5. For this excitation temperature we derived a LTE column density from 296GHz transition of 2.41×10^{14} cm^{-2} using a single component. For the H_2 column densities in chapter 5, we estimate an abundance of about 3×10^{-9} which is an order of magnitude larger than that found in Sgr B2. However, we need to measure another line both to firmly confirm this identification and to constrain the excitation of this species.

6.4 Discussion

Since the 296 GHz line is tentatively assigned to HCNH$^+$ we will briefly mentioned the most far reaching implications of the observed large abundance in an AGN. As already mentioned in the introduction, HCNH$^+$ is the precursor of HCN and HNC. A large abundance of HCNH$^+$ in an

AGN would imply that HCN could be enhanced in AGN. Indeed, it has been proposed that the large HCN/HCO^+ ratios found in AGN is due to the enhancement of HCN abundance due the X-rays (see e.g. Izumi et al. 2015). The enhancement of the $HCNH^+$ abundance due to a larger ionization rate induced by x-rays would be naturally explained by the ion-molecule chemistry. The AGN dominated chemistry fully consistent with scenario proposed in chapter 4 from the H_3O^+ abundance. Before drawing any firm conclusion, we need to confirm the identification of $HCNH^+$ by observing other transitions at mm wavelengths.

6.5 Conclusions

We report, for the first time, the tentative detection of the molecular ion $HCNH^+$ toward a galaxy, NGC4945.

We have only detected only one transition, the 296 GHz. Unfortunately, the other transition, at 370 GHz, lies in an atmospheric window with low transmission. Confirmation of the identificacion need the observation of other lines.

From the upper limit to the intensity of the 370 GHz line and the 296 GHz line we derive an upper limit to the excitation temperature of 35 K. The estimated LTE $HCNH^+$ column density is 2.41×10^{14} cm^{-2} which corresponds to an abundance of abundances of 3×10^{-9}, much larger than that estimated of the Galactic center in the Milky Way.

The large abundance of HCNH+, the precursor of HCN and HNC, would naturally explain the claimed enhancement of HCN abundance in the AGN, due to the enhancement of the ionization rate by X-rays. This supports the scenario proposed in chapter 4 for the large abundance of H3O^+.

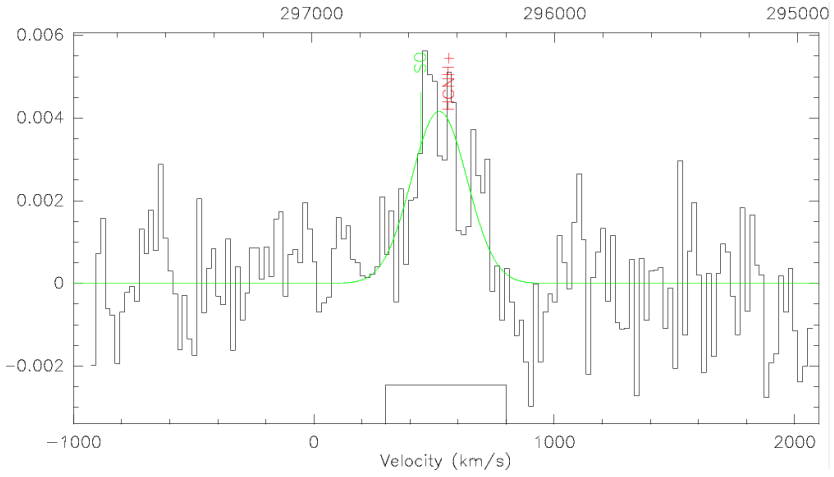

Figure 6.1: Spectra of $HCNH^+$ observed toward iNGC 4945 with APEX in September 2014. We have fitted the $HCNH^+$ 396GHz line with a gaussian, but is slightly blended with the SO emission (see next Figure)

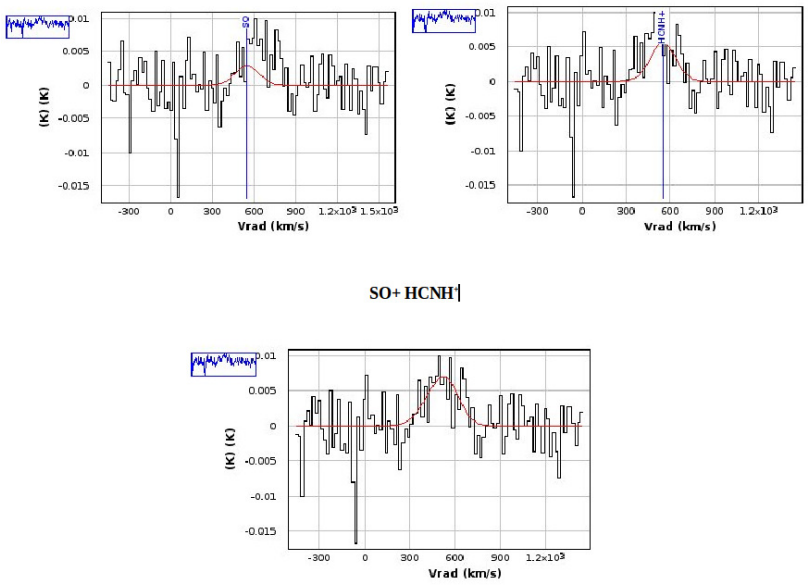

Figure 6.2: LTE spectral simulation of the contribution of the SO (upper left panel), $HCNH^+$ (rupper right panel) , and the combination of $HCNH^+$ and SO (in NGC 4945.

Chapter

7

Discusion

7.1 Discusion of the chapter 4

Our study of the excitation of H_3O^+ shows an overluminous emission of the 364GHz transition which is observed in all the three detected galaxies. Though the para-transition H_3O^+ line is affected by blending with CH_3OH, the other methanol transitions observed in our survey allow us to accurately account for its contribution to the observed profile, thus the residual was attributed to the 307 GHz H_3O^+; 388GHz para-transition is blended with SO_2 and ^{33}CS.

Past studies of H_3O^+ did not study transition at 388GHz and the effect of the dust under para-transitions (using data of Hershel), which is helpful to have a better estimation of the kinetic temperature and the opacity of the interestelar medium. Also, we have the first study of H_3O^+ molecule toward NGC4945

The observed H_3O^+ line radio can be fitted with a Tex of 100K for Galactic Center(Van der Tak et al 2006), in comparation, we need use a Tex of 200K for extragalactic sources. The column density N(para H_3O^+)=1.83(0.27)x10^{15} cm^{-2} for Sgr B2 (Envelope) and Sgr B2 (Core)= 6.81(1.01)x10^{15}. The ortho/para(o/p) ratio tends to 1 at high temperatures. For SgrA assuming Tex=100K and N(H_3O^+) less than 6x$10^{13}cm^{-2}$ (Van der Tak et al 2006), in comparation we found a column density of 2.6(0.39)x$10^{13}cm^{-2}$ for NGC253, we see a similar magnitud for SgrA, and assume the same bearing for NGC4945 and ARP220 because have a similar fitting for LTE-conditions.

Phillips et al. (1992) studied toward different sources including Sgr B2 H_3O^+ line ratios under high density (10^6 to 10^7) at high temperatures (more than 50K), they found that the 396GHz line is about a factor of 2 stronger than the 364GHz line, with 307GHz line much weaker, also, they found a lower column density that Van der Tak using H_3O^+ line at 396GHz line and a

density of $10^5 cm^{-3}$ for SgrB2(Envelope) By contrast in our study we have a column density of 2.13x$10^{13} cm^{-2}$ for ortho-transition (396GHz) and 2.6x10^{13} for 364GHz transition (not complete fitted) using transitions at 307GHz and 388GHz. The 364GHz line is stronger than 396GHz line in the present study, opposite to the result of Phillips toward the rest of sources in the Galactic Center (except SgrB2). In adittion The same authors found a ratio of $N(HCO^+)/N(H_3O^+)= 10^{-8}$, in comparation of the present stdudy we found $N(HCO^+)/N(H_3O^+)= 1.55$ for NGC253 considering column density founded in $N(HCO^+)$=4.03x$10^{13} cm^{-2}$; with $N(HCO^+)$= 1.43x$10^{13} cm^{-2}$ for NGC4945 we have $N(HCO^+)/N(H_3O^+)= 0.079$; In the case of ARP220 we have $N(HCO^+)/N(H_3O^+)=$ 0.065 using a $N(HCO^+)$= 1.9x$10^{14} cm^{-2}$ (Villicaña-Pedraza 2015 in prep.). An abundance of 6.01^{-10} for HCO^+ and 3.88^{-10} for NGC253 for NGC253 were finded; We found an abundance of 2.14^{-10} for HCO^+ and 2.6^{-9} for H_3O^+ toward NGC4945; Finally, we have an abundance of 9.5x10^{-9} for and HCO^+ and 1.45x10^{-7} for H_3O^+ in Arp220. In all the cases the ratio finded by Phillips is higher that the present study, except for Arp220.

Aalto et al. (2011) made some supposition, they used the critical density of the H_3O^+ molecule, and found that the low reduced mass of the H_3O^+ molecule makes its excitation very sensitive to radiative pumping by dust. Some galaxies have black holes which a disk of molecular material is falling. Excitations of these molecules in the disk or in a jet can result in megamasers with large luminosities. Hydroxyl, water, and formaldehyde masers are known to exist in these conditions (Lo et al. 2005). Water and methanol masers are also typical with environments of star forming regions. Some of the masers in that regions can get luminosities sufficient for detection from external galaxies, masers observed from distant galaxies generally result in entirelly different conditions.

7.2 Discusion of the chapter 5

The $^{12}C/^{13}C$ ratios for galaxies ranges from ∼11 to ∼15, which are much lower than the $^{12}C/^{13}C$ ratio of less of 81 and ∼50 found in NGC 253 (Martin et al. 2010) and NGC 4945 (Henkel and Mauersberger 1993, Henkel et al. 1994), indicating that lines from main isotopologues are optically thick.

In our study of the survey, we also found $^{16}O/^{18}O$ ratios of 118.4 (10.9) for NGC 4945 and of more than 232 for NGC 253. These ratios are likely strongly affected by opacity effects in the ^{13}CO lines. On the other hand, the $^{32}S/^{34}S$ ratio of more than 58 and $^{18}O/^{17}O$ ratio of 7.7 (0.8) found in NGC 253, and the $^{18}O/^{17}O$ ratio of 9.8 (2.9) toward NGC 4945 probably are less affected by optical depth effects since in their estimations we used the less abundant species ^{13}CS, $C^{34}S$, $C^{18}O$ and $C^{17}O$.

The $^{32}S/^{34}S$ ratio found in NGC 253 is a factor of ∼3 higher than that in the GC. In addition the $^{18}O/^{17}O$ ratios in NGC 4945 and NGC 253 are also factors of 2.4-3 higher compared to that of the GC. The differences in the $^{32}S/^{34}S$ and $^{18}O/^{17}O$ ratios between the GC and the starburst

galaxies NGC 4945 and NGC 253 suggest that the gas is less processed in the latter than in the GC, consistent with previous studies (Martin et al. 2010, Armijos-Abendaño et al. 2015). The high $^{18}O/^{17}O$ ratios in the galaxies NGC 4945 and NGC 253 with material less processed compared with the GC gas are also consistent with the suggestion that ^{17}O is more secondary than ^{18}O in stellar nucleosynthesis (Wilson and Rood 1994).

^{13}CN was only detected in Arp220 near of noise signal, thus it is tentative. This isotope was predicted by Henkel et al. (2014).

7.3 Discusion of the chapter 6

We found a new extragalactic molecule $HCNH^+$, a first observation showed a weak line blended. A specific observation in 2014 show in NGC 4945 a clear line and the contribution in the line together with SO. We observe in Arp 220 and a tentative feature in NGC 253. The transition at 370GHz is over the atmospheric region, and we have been working to observe transitions at 444GHz but we found the same problem with the atmospheric region.

Chapter

8

Conclusions

We present the first submm line survey of extragalactic sources carried out by APEX. The surveys cover the 1mm atmospheric The survey covers the 1mm atmospheric window from 270 to 370GHz toward NGC253, NGC4945 and Arp220. Derived from our study we found the next points:

8.1 Conclusion of the chapter 4

- We have detected the emission from para-H_3O^+ toward the nuclei of NGC253, NGC4945 and Arp220 in two submillimeter lines, the 307 GHz and the 364 GHz. We also observed another submillimeter transition of para-H_3O^+, the 388 GHz line, and one ortho-H_3O^+ transition, the 396 GHz line toward NGC253. HIFI Herschel observations of the ground state lines in the Far-IR are also presented.

- We carried out a multiline transition analysis of the H_3O^+ emission toward NGC253. We first corrected the 307 GHz line of H_3O^+ for the blending of the 307 GHz line of CH_3OH using other methanol transitions observed in our surveys. Our LTE excitation analysis of H_3O^+ of NGC253 shows that all line cannot be properly fitted and that the364 GHz line seems to be over-luminous, suggesting that the derived column densities using only this line could result in severe overstimations.

- From our non-LTE analysis of H_3O^+ in NGC253 with RADEX we found that the collisional excitation cannot explain the observed intensity of the ortho 396 GHz line. Excitation by radiation from the dust in the Far-IR can roughly explain the observations if the H_2 densities are relatively low (a few 10^4 cm^{-3}).

- Our derived column densities agree well with that derived previously using submillimeter and Far-IR lines for Arp220, but is a factor of 25 smaller from that derived towards

NGC253.

- From the derived H_3O^+ column densities we conclude that the chemistry of this molecule is dominated by ionization produce by the starburst in NGC253 (UV radiation from the O stars) and Arp 220 (cosmic rays from the supernovae) and likely from the AGN in NGC4549 (X-rays).

8.2 Conclusion of the chapter 5

We did a survey of three galaxies from 270GHz to 370GHz from them we derivate the next results:

- We found in NGC 253, 150 transitions of 26 molecules; For NGC 4945, 136 transitions of 24 molecules, and 64 transitions of 17 molecules for Arp 220.

- In addition,we checked for image band image, and we found a strong band image from CO at 360GHz for NGC253.

- Column densities and rotation temperatures have been determinated by Local Thermodinamical Equilibrium(LTE) using MADCUBA_IJ software.

- We did a comparison between the chemistry of NGC 253 from Martin et al. (2006) at 2mm, Martin et al. (2011) for Arp220 at 1.3mm, and Wang et al. 2004 for NGC4945 at 3mm. The comparison show the detection of N_2H^+, CN, H_3O^+ for NGC253 in the present work that were not detected before by Martin et al. (2006), SO2, H_3O^+ for NGC4945 that were not detected for Wang et al. 2004.

- The differences in the $^{32}S/^{34}S$ and $^{18}O/^{17}O$ ratios between the GC and the starburst galaxies NGC 4945 and NGC 253 suggest that the gas is less processed in the latter than in the GC, consistent with previous studies (Martin et al. 2010, Armijos-Abendaño et al. 2015).

- The high 18O/17O ratios in the galaxies NGC 4945 and NGC 253 with material less processed compared with the GC gas are also consistent with the suggestion that 17O has more representative products than 18O in stellar nucleosynthesis (Wilson and Rood 1994).

- From the chemical complexity observed in NGC253 it has been proposed (Martin et al. 2006, Aladro et al. 2010) the this galaxy is a starburst in an intermidate stage of evolution. This would indicate that the chemistry and to large extent also the heating in NGC4945 is dominated by the starburst with little influence of the AGN.

- The H_3O^+ emission arises from a different region that the other molecules detected in the survey. A posible scenrario would be that while H_3O^+ is mainly concetrated around the black hole, the other molecules are extended over a larger region where star formation is taken place. This is supported by the excitation of the H_3O^+ in low density gas.

- The difference between the molecular abundance ratios between the ULIRG Arp200 and the starburst galaxies in our sample migh be due to the higher density gas in Arp 220 which makes the excitation of high dipole moments easier at 345 GHz the this galaxy than in the other two galaxies.

8.3 Conclusion of the chapter 6

- We report, for the first time, the tentative detection of the molecular ion $HCNH^+$ toward a galaxy, NGC4945.

- We have only detected only one transition, the 296 GHz. Unfortunately, the other transition, at 370 GHz, lies in an atmospheric window with low transmission. Confirmation of the identificacion need the observation of other lines.

- From the upper limit to the intensity of the 370 GHz line and the 296 GHz line we derive an upper limit to the excitation temperature of 35 K. The estimated LTE $HCNH^+$ column density is 2.41×10^{14} cm^{-2} which corresponds to an abundance of abundances of 3×10^{-9}, much larger than that estimated of the Galactic center in the Milky Way.

- The large abundance of $HCNH^+$, the precursor of HCN and HNC, would naturally explain the claimed enhancement of HCN abundance in the AGN, due to the enhancement of the ionization rate by X-rays. This supports the scenario proposed in chapter 4 for the large abundance of $H3O^+$.

8.4 Conclusiones del capitulo 4

- Hemos detectado la emision desde para-H_3O^+ en el nucleo de NGC253, NGC4549 y Arp220 en dos lineas submilimetricas, a 307 GHz y 364 GHz. Ademas, nosotros hemos observado otra transicion submilimetrica de para-H_3O^+, una linea a 388 GHz, y una ortho-H_3O^+ transicion, la linea a 396 GHz en NGC253. Observaciones de lineas en el estado base de HIFI Herschel en el Far-IR son ademas presentadas.

- Hemos llevado a cabo un analisis multilinea de transiciones de emision de H_3O^+ en NGC 253. Primero corregimos la linea a 307GHz de H_3O^+ para la linea mezclada con CH_3OH usando otras transiciones de metanol observadas en nuestro sondeo. La excitacion en nuestro analisis LTE de H_3O^+ de NGC 253 muestra que todas las lineas no pueden ser ajustadas adecuadamente y que la linea de 364 GHz parece ser mas luminosa, sugiere que la columna de densidad derivada usando solo esta linea podria resultar sobrestimado.

- De nuestro analisis non-LTE de H_3O^+ en NGC 253 con RADEX encontramos que la excitacion colisional no puede explicar la intensidad observada de la linea otro 396GHz . Excitacion por radiacion proveniente del polvo en el Far-IR puede explicar aproximadamente las observaciones si la densidad de H_2 son relativamente bajas (unos pocos 10^4 cm^{-3}).

- Nuestra densidad de columna derivada esta de acuerdo con con aquella derivada previamente usando lineas submilimetricas y de Far-IR para Arp 220, pero es un factor 25 mas pequeño que el derivado para NGC 253.

- De la densidad de columna derivada de H_3O^+ concluimos que la quimica de la molecula esta dominada por ionizacion producida por el brote de formacion estelar en NGC 253 (radiacion UV desde estrellas O) y Arp 220 (rayos cosmicos desde supernovas, y probable para la AGN NGC4945 (rayos-x))

8.5 Conclusiones del capitulo 5

Se ha realizado un sondeo de tres galaxias de 270GHz a 370GHz de lo cual se derivan los siguientes resultados:

- Se encontro en la galaxia NGC 253, 150 Transiciones de 26 moleculas. Para NGC 4945, 136 transiciones de 24 moleculas, mientras que 64 transiciones de 17 moleculas de Arp220.

- Adicionalmente se revisaron los efectos de banda imagen y encontramos una fuerte linea de banda imagen de CO a 360GHz para NGC253.

- Se obtuvieron densidades de columna y temperaturas de rotacion determinadas a Equilibrio Termodinamico Local (LTE) usando el software MADCUBA_IJ.

- Se realizo una comparacion entre la quimica de NGC253 obtenida por Martin et al. (2006) a 2mm, Martin et al. (2011) para Arp220 a 1.3mm, y Wang et al. (2004) para NGC4945

at 3mm. La comparacion mostro la deteccion de N_2H^+, CN, y H_3O^+ para NGC253 en el presente trabajo y no fueron detectados antes en esa misma fuente; SO2, H_3O^+ para NGC4945 que no fueron detectadas por Wang et al. (2004).

- La diferencia entre los cocientes $^{32}S/^{34}S$ y $^{18}O/^{17}O$ entre el Centro Galactico (CG) y las galaxias de brotes de formacion estelar NGC 4945 y NGC 253 sugieren que el gas esta menos procesado en el ultimo que en el CG, lo cual es consistente con estudios previos (Martin et al. 2010, Armijos-Abendaño et al. 2015).

- El alto cociente $^{18}O/^{17}O$ en las galaxias NGC 4945 y NGC 253 con material menos procesado comparado con el gas del CG es consistente con la sugerencia que ^{17}O es mas representativo que ^{18}O en nucleosintesis estelar (Wilson and Rood 1994).

- De la complejidad quimica observada en NGC 253 se ha propuesto (Martin et al. 2006, Aladro et al. 2010) que esta galaxia es starburst en una etapa intrmedia de evolucion. Esto podria indicar que la quimica y gran extension del calentamiento en NGC 4945 esta dominada por la starburst con un poco de influencia de el AGN.

- La emison de H_3O^+ surge de diferente region que las otras moleculas en el censo. Un posible escenario podria ser que mientras H_3O^+ esta principalmente concentrado alrededor de el agujero negro, las otras moleculas estan extendidas en una gran region donde la formacion de estrellas esta teniendo lugar. Esto es apoyado por la excitacion de H_3O^+ en gas con baja densidad.

- La diferencia entre los cocientes en la abundancia molecular entre ULIRG Arp220 y las galaxias starburst en nuestra muestra podria ser debido a la alta densidad de gas en Arp 220 el cual hace la excitacion del momento dipolar alto mas facil a 345 GHz en esta galaxia que en las otras dos galaxias.

8.6 Conclusiones del capitulo 6

- Se reporta, por primera vez, la deteccion tentativa del ion molecular $HCNH^+$ en la galaxia NGC4945.

- Tenemos solo detectada una transicion, a 296GHz. Desafortunadamente, la otra transicion, a 370 GHz, se encuentra en una ventana atmosferica con baja transmision. Confirmacion de la identificacion necesita observacion de otras lineas.

- Del limite superior a la intensidad de la linea de 370 GHz y la de 296 GHz derivamos un limite superior a la tempertura de excitacion de 35 K. La densidad de columna estimada en LTE para $HCNH^+$ es 2.41×10^{14} cm^{-2}, la cual corresponde a una abundancia de 3×10^{-9}, mucho mas grande que la estimada en el Centro Galactico de la Via Lactea.

- La gran abundancia de $HCNH^+$, el precursor de HCN y HNC, podria naturalmente explicar el aumento de la abundancia de HCN en el AGN, debido al aumento de la taza de ionizacion por rayos-x. Esto soportaria el escenario propuesto en el capitulo 4 para explicar la gran abundancia de $H3O^+$.

Part I

APPENDIX A: BASICS AND RADIATIVE TRANSFER

8.6.1 Radiative Transfer

In free space the specific intensity Iν is independent of the distance along a ray. Iν will change only if radiation is absorbed or emitted. The change of Iν is described by radiative transfer equation. For a change in Iν along the line of sight , a loss term dIν_- and a gain term dIν_+ are introduced taking the form

$$\mathrm{dI}\nu_- = -\kappa_\nu \mathrm{I}\nu \mathrm{ds}$$
$$\mathrm{dI}\nu_+ = \epsilon_\nu \mathrm{ds}$$

The change of intensity in a sheet of material of thickness ds will be

$$[\mathrm{I}\nu(\mathrm{s+ds}) - \mathrm{I}\nu(\mathrm{s})]\mathrm{d}\sigma\mathrm{d}\Omega\mathrm{d}\nu = [-\kappa_\nu \mathrm{I}\nu + \epsilon_\nu] d\sigma \; d\Omega \; d\nu$$

We obtain from the past expression the **transfer equation**(see Fig. 4)

$$\frac{dI\nu}{ds} = -\kappa_\nu \mathrm{I}\nu + \epsilon_\nu$$

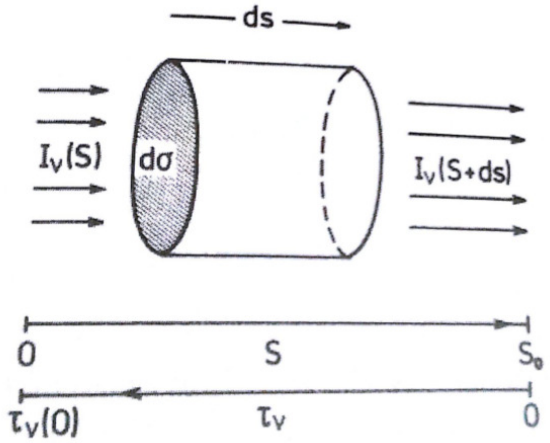

Figure 8.1: The quantities used in the equation of transfer

The absortion coefficient κ_ν of the medium is independent of the intensity Iν leading to the form dIν_-. In a similar way for the emissitivity ϵ_ν.
For some cases the solution of the differential equation of transfer is straightforward

1. Emission only: κ_ν=0

$$\frac{dI\nu}{ds} = \epsilon_\nu$$

2. Absortion only: ϵ_ν=0

$$\frac{dI\nu}{ds} = -\kappa_\nu \mathrm{I}\nu$$

3. Thermodynamic equilibrium

$$\frac{dI\nu}{ds} = 0$$

8.6.2 Basic Definitions

The electromagnetic radiation in the radio range can be considered to travel in straight lines called rays. The infinitesimal power DW intercepted by an infinitesimal surface dσ is the brightness(Iν) defined as (see Fig. 1):

$$dW = I\nu \cos\theta d\Omega d\sigma d\nu$$

Where

dW= infinitesimal power, in watts.
dσ= infinitesimal area of surface, in cm^2
dν= infinitesimal bandwidth, in Hz
θ= angle between the normal to dσ and the direction to dΩ
Iν= brightness or specific intensity, in W $m^{-2}Hz^{-1}sr^{-1}$

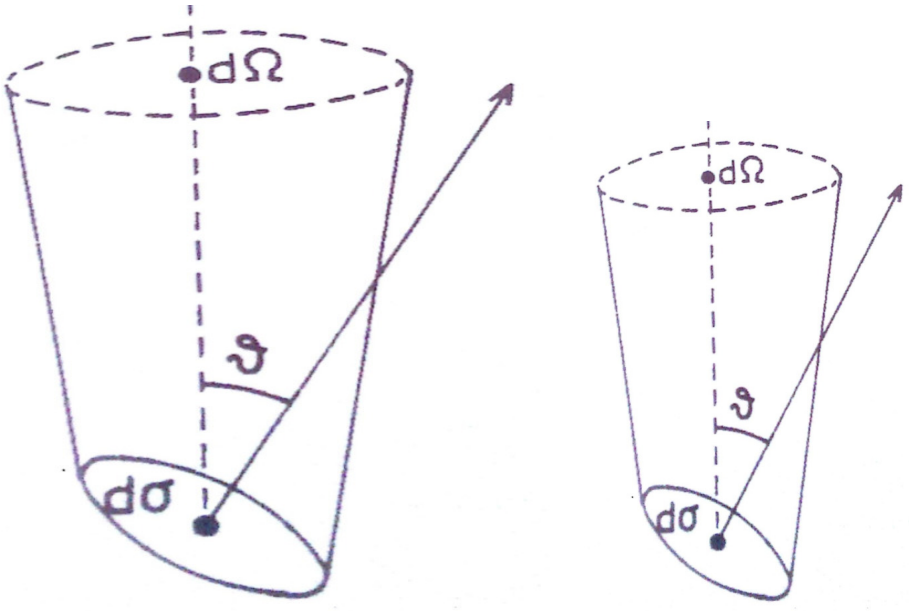

Figure 8.2: Definition of brightness

The term intensity or specific intensity Iν is used instead of the term brightness. The total flux (in W $m^{-2}Hz^{-1}$) of a source is obtained by integrating the past ecuation over the total solid angle Ωs subtended by the source:

$$S\nu = \int_{\Omega s} I\nu(\theta,\phi)\cos\theta d\Omega$$

The flux density Sν of radio sources is very small, thus the Jansky (Jy) unit has been introduced

$$1\ Jy = 10^{-26}\ Wm^{-2}Hz^{-1} = 10^{-23} erg\ s^{-1}cm^{-2}Hz^{-1}$$

The brightness of an extended source is a quantity similar to the suface brightness in optical astronomy, it is independent of the distance to the source.

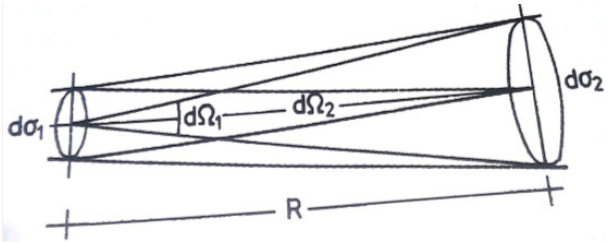

Figure 8.3: The brightness is independent of the distance along a ray.

The total flux, Sν, density shows the dependence of $1/r^2$. Consider a sphere with uniform brightness Iν with a radius R, the total flux received by an observer at the distance r is

$$S\nu = \int_{\Omega s} I\nu \cos\theta d\Omega = I\nu \int_0^{2\pi} \left(\int_0^{\theta c} \sin\theta \cos\theta d\theta \right) d\phi$$

where the angle θc that the radius of the sphere subtends at r is

$$\sin\theta c = \frac{R}{r}$$

We obtain

$$S\nu = \pi I\nu \sin^2 \theta c \text{ or } S\nu = I\nu \frac{\pi R^2}{r^2} = I\nu \Delta \Omega$$

where $\Delta \Omega$ is defined as the solid angle subtended by an object at a distance r.

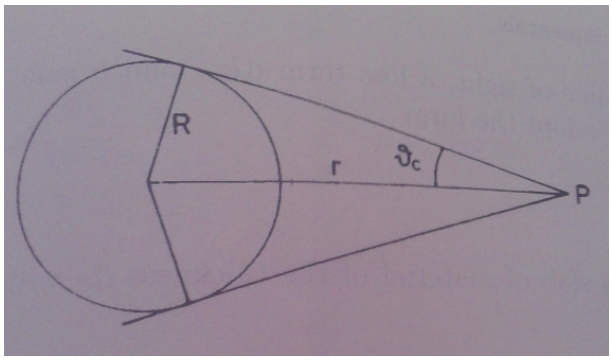

Figure 8.4: Geometry describing the total flux received at a point P from an uniformly bright sphere.

The energy density per solid angle is

$$u\nu(\Omega) = \frac{1}{c} I\nu$$

If integrated over the complete sphere, 4π steradian the past ecuation, results in the total energy density

$$u\nu = \int_{4\pi} u\nu(\Omega) d(\Omega) = \frac{1}{c} \int_{4\pi} I\nu d\Omega$$

Line profile

A transition show a profile $\phi(\nu)$ named line profile function normalized, which line profile is a function center in νo, that goes to 0 out of the central frequency, thus

$$\int_{-\infty}^{\infty} \phi(\nu)\ \mathrm{d}\nu = 1$$

The maximum value of the line profile $\phi(\nu\mathrm{o})$, is the inverse of the equivalent width of the line $\Delta\nu$eq

$$\Delta(\nu\mathrm{o})\Delta(\nu\mathrm{eq}) = \int_{-\infty}^{\infty} \phi(\nu)\ \mathrm{d}\nu = 1$$

The equivalent width of the line profile is the same of the full width half maximum $\Delta\nu_{\ 1/2}$.
The observed width in a line allow obtain an upper limit of the kinetic temperature of the region.

$$\frac{T_k}{K} \leq 22.7 \frac{m}{m_H}\ \frac{\Delta\nu_o bs}{km/s}^{\ 2}$$

8.6.3 Thermodinamic equilibrium

In thermodynamic Equilibrium (TE).

$$\mathrm{I}\nu = \mathrm{B}\nu(\mathrm{T}) = \epsilon_\nu\ /\kappa_\nu$$

Where the spectral distribution of the radiation in thermodynamic equilibrium is given by the Planck law, which depends only on the temperature T.

$$\mathrm{B}\nu(\mathrm{T}) = \frac{2h\nu^3}{c^2}\ \frac{1}{e^{(h\nu/\kappa T)-1}}$$

Where h is the Planck constant, κ is the Boltzman constant, c is the speed of light, ν is the frequency, and T the temperature.
At lower frequencies is possible to use the Raleigh-Jean approximation

$$\mathrm{I}\nu = \frac{2k\nu^2}{c^2}\mathrm{T}_B$$

In this case, the radiation temperature is proportional to the intensity

$$\mathrm{I}\nu = \frac{2k\nu^2}{c^2}\mathrm{T}_R$$

$$\mathrm{T}_R = \mathrm{I}\nu\mathrm{T}_B$$

In radioastronomy, one uses the radiation temperature to measure the intensity of the molecular lines. As discussed in Chapter 2, different temperatures scales are used depending on the source size.
From the observed temperature of the molecular lines one can estimate column densities and rotation temperatures (T rot) for each species.
The energetic states are in equilibrium too, that mean, the ionization states are described by the Saha equation for a ionization teperature T_{ion}=T

$$\frac{nr+ne}{nr} = 2\frac{gr+1}{gr}\ (\frac{2\pi mkT}{h^2})^{3/2}\ \mathrm{e}^{\chi r/KT}$$

where nr is the particle density in the ionization state r and χr is the ionization potential that the level population of energy of each ionization state of one specie are the Boltzmann law for an excitation temperature T_{ex}=T

$$\frac{n2}{n1} = \frac{g2}{g1} e^{-\frac{\Delta E}{kT}}$$

and the velocity distribution of the particles is calculated with the Maxell law for a kinetic temperature Tk=T

$$f(v) = \left(\frac{m}{2\pi kT}\right)^{3/2} e^{-mv^2/2KT}$$

All the temperatures in termodinamical equilibrium are in agreement and define the termodinamical temperature in equilibrium T

$$T_B = T_{ion} = T_{ex} = T_k = T$$

1.Local Thermodinamic equilibrium (LTE)

Thermodynamic equilibrium will be realized only in very special circumstances such as in a black enclosure or in stellar interiors. As already mentioned, in LTE:

$$\frac{\epsilon_\nu}{\kappa_\nu} = B\nu(T)$$

Considering $d\tau\nu$ as:

$$d\tau\nu = - \kappa_\nu ds$$

Applying the optical depth to the transfer equation one obtains:

$$-\frac{1}{\kappa_\nu} \frac{dI\nu}{ds} = \frac{dI\nu}{d\tau\nu} = I\nu - B\nu(T)$$

There are two limit cases:

- Optically thin emission when it is that with $\tau\nu \ll 1$ the radiation along the way is negigible.
- Optically thick emission when $\tau\nu \gg 1$, the emitted radiation is also absorbed. Such absorption can be in the region where radiation is emitted, and also along the way.

The Local termodinamical Equilibrium is a situation when the density of a system grow and the energetical state of the particles in the medium is controlated by collisions. The velocities into the particles are easy termalized, then are controled by a Maxwell law for a temperature Tk. If the collisional transitions are more than radiative transitions, levels are termalized and the populations are calculated by Boltzman law with Tex$\simeq$Tk, and for the termalized of ionization states is calculated with Saha law Tion$\simeq$Tk.

Absorption and Emission coefficients

The absortion and the emission coefficients in the case of molecular clouds are related with the Interaction between a photon and molecule through three kinds of transitions:

- Absorption: The photon is absorbed by the molecule. Thus, the system changes from low excitation (Elow, E1 in Fig. 6) state to higher excitation(Eup, E2 in Fig. 6) state. The probability of the situation is indicated by Einstein coefficient of absorption, B_{LU}.

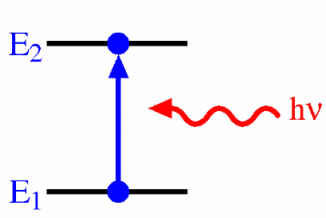

Figure 8.5: Absortion of a photon hν.

- Spontaneous emission (see Fig. 7). The system decays from the upper level to the lower level, radiating a photon with an energy E=hν_U. The Einstein coefficient of spontaneous emission A_{UL} is related to B_{LU} as $A_{UL}=\frac{2h\nu_{UL}^3}{c^2}B_{UL}$. The lifetime of the electron in the higher energy level is $1/A_{UL}$ (see Fig. 8).

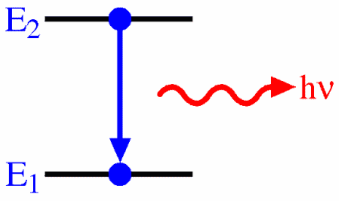

Figure 8.6: Spontaneous emission

- Stimulated emission. Is the interaction of a molecule with energy h$\nu_U L$ corresponding to the energy jump between two molecular levels, induces theemission of the photon with the same energy. The probability of this transition is given by the Einstein coefficient of stimulated emission, $B_U L$. Also, the Absortion B_{LU} and the stimulated coefficients are related by $g_L B_{LU}= g_U B_U L$ where g_L is the statistical weights of lower level and g_U belong to the statistical weights of the upper level.

Using Planck law, level population from Boltzman law at temperature T, one obtain a relation between coefficients

$$A_{21}= \frac{2h\nu_{21}^3}{c^2}\ B_{21}$$

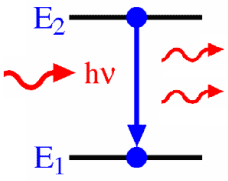

Figure 8.7: Definition of stimulated emission

8.6.4 Excitation temperature

If we named the emission coefficient j_ν and the absorcion coefficients κ_ν, then the radiative transport equation is

$$\frac{dI\nu}{dl} = -\kappa_\nu \, I\nu + j\nu$$

The absortion coefficient has cm^{-1} unit, emission coefficient erg s^{-1} cm^{-3} $sr^{-1}Hz^{-1}$, the inverse of absortion coefficient is a length and it is named mean free path of the radiation or photon $l\nu$ and is the mean distance line by a photon of frequency ν before to be absorbed.

$$l\nu = \frac{1}{\kappa_\nu}$$

The source function $S\nu = j\nu/\kappa_\nu$ is a characterization of the excitation temperature Tex, then

$$S\nu = \frac{j_\nu}{\kappa_\nu}$$

and the transport equation is

$$\frac{dI\nu}{d\tau\nu} = -I\nu + S\nu$$

The excitation temperature is that temperature in which the source function is the same of the Planck function and is depending of the frequency.

$$S\nu = B\nu(Tex)$$

In the Raleigh-Jeans approximation the source function is proportional at the excitation temperature

$$S\nu = \frac{2\kappa\nu^2}{c^2} Tex$$

Using the brightness and excitation temperature, the transport equation in the Raleigh-Jeans approximation is

$$T_B = T_{bg} e^{-\tau_\nu} + T_{ex}(1 - e^{-\tau\nu})$$

In a plane parallel region formed by two sheet with the same temperature T_{ex} and optical deep $\tau 1$ and $\tau 2$ the brightness temperature for the transport equation is

$$T_{B1}= T_{bg}e^{-\tau_1}+T_{ex}(1\text{-}e^{-\tau_1})$$

$$T_{B2}= [T_{bg}\ e^{-\tau_1}\ +\ T_{ex}\ \text{-}\ T_{ex}e^{-\tau_1}]e^{-\tau_2}+\ T_{ex}\text{-}T_{ex}e^{-\tau_2}\ =\ T_{bg}\ e^{-(\tau_1+\tau_2)}+T_{ex}[2\text{-}e^{-(\tau_1+\tau_2)})]$$

If the optical deep is $\tau 1+\tau 2$, the brightness temperature is

$$T_B= T_{bg}e^{-(\tau_1+\tau_2)}+\ T_{ex}[1\text{-}e^{-(\tau_1+\tau_2)}]$$

8.6.5 Colisional Transitions

There are other process that can yield excitation or desexcitation of the system are the Colisionals transitions . In one collision with other particle, the system can get part of the kinetic energy of the colision particle and cross from 1 to 2 state, contrary, give energy to the colisionant energy and move from 2 to 1 state. The Colisional excitation probability is C_{12} and desexcitation C_{21}. The transition colisional probabilities C_{12} and C_{21} are the product of the colisional particule densities n, the coefficient of colisional excitation $\gamma_1 2$ and the the coefficient of colisional desexcitation $\gamma_2 1$.

$$\gamma_{ij}=\int \sigma_{ij}(\nu)\nu f(\nu)d\nu$$

where the cross section of colision is σ_{ij} and correspond to the velocity ν and f(ν) the velocity distribution of the colisionant particles.
The coefficient of excitation and desexcitation are independents.
The excitation coefficient is smaller than desexcitation coefficient. Out of termodinamical equilibrium,

$$\frac{\gamma_{12}}{\gamma_{21}}\ =\ \frac{g_2}{g_1}\ e^{\frac{h\nu_{21}}{kT_k}}$$

8.6.6 Emision and absortion lines

When one spectral line is observed, the intensity is I_ν^{ON} has a contribution of the neighboring continuum and the line

$$I_\nu^{ON}= I\nu(0)e^{-\tau_\nu}\ +\ S\nu(1\text{-}\ e^{-\tau_\nu})$$

The elimination of the baseline (the neighboring continuum) lie in rest the observed intensity out of the line, $I_\nu^{OFF}(\tau\nu=0)$

$$I_\nu^{OFF}=I_\nu(0)$$

and the received intensity of the line is

$$I_\nu= I_\nu^{ON}\text{-}I_\nu^{OFF}= [S\nu\text{-}I_\nu(0)](1\text{-}\ e^{-\tau_\nu})$$

In temperature units, the line temperature T_L is a radiation temperature T_L=Jν(T_B)

$$I\nu= \frac{2\kappa\nu_{21}^2}{c^2}T_L(\nu)$$

In the Raleigh-Jeans Approach the line temperature is

$$T_L(\nu)= (T_{ex}\text{-}T_{bg})(1\text{-}\ e^{-\tau_\nu})$$

The Emission line is $T_{ex} \succ T_{bg}$, if the spectal line is negative one can observe an Absortion line $T_{ex} \prec T_{bg}$ and the intensity will be negative.

8.6.7 Maser emision

The maser effect (Microwave Amplification by Stimulated Emission of Radiation) is created when there is an inversion of transition level population n2/g2 $\succ$ n1/g1. The populations inversion mean that the excitation temperature is negative and the optical deep is negative too, because

$$\mathrm{e}^{(}h\nu_{21}/\kappa Tex) \prec 1.$$

The intensity of a line with maser effect is

$$\mathrm{T}_0 = (\mathrm{T}_{ex}\text{-}\mathrm{T}_{bg})(1\text{- }\mathrm{e}^{-\tau_0}) \simeq \parallel \mathrm{T}_{ex} \parallel \mathrm{e}^{\parallel\tau_0\parallel}$$

There are an exponential amplification of the radiation when it interact with matter. The line temperature of a maser transition can be high. The maser emission ocurr in small regions named maser spots, and the antenna temperature or flux density are intense moderately, also by consequence of the radiation amplification has high variability.
In order to have maser effect is needful the existence of transitions to and from other levels, this transitions are named "pumping" because are the responsible of support the population inversion. In an example, Consider 3 levels, if $\mathrm{P}_1 2 \succ \mathrm{P}_2 1$ can produce population inversion and maser effect in the transition.
The pumping mechanism are not clear but are required high densities such as $\mathrm{n} \simeq 10^8\text{-}10^{10}\mathrm{cm}^{-3}$, high temperatures $\mathrm{T} \simeq 10^2\text{-}10^3\mathrm{K}$ and a close bright source ($\succ 10\mathrm{L}\odot$).
There are two kinds of pumping:

- Radiative: Produced by IR radiation from a brightness star (circumstellar regions of M giant stars)
- Collisional: It is produced in regions of stellar formation in the interstellar medium near of early stars O-B.

Part II

APPENDIX B: Complete fit Gauss for the galaxies

In this section we show the complete tables of the results obtained for al the transitions in every molecule toward NGC 253, NGC 4945 and Arp 220.

Molecule Transition	ν (MHz)	AREA (mK Km s^{-1})	$\Delta V_{1/2}$ (km s^{-1})	V_{LSR} (km s^{-1})	T_{MB} K	N (cm^{-2})
CO 3- 2	345795.9899	685.130	136.12	182.67	4.231	17.912
CO 3- 2	345795.9899	437.634	95.24	300.22	3.351	17.985
$C^{17}O$ 3- 2	337061.1298	1.164	48.04	184.82	0.023	15.089
$C^{17}O$ 3- 2	337061.1298	3.702	140.89	286.06	0.025	15.685
$C^{18}O$ 3- 2	329330.5453	10.750	66.87	164.48	0.151	16.05
$C^{18}O$ 3- 2	329330.5453	24.679	113.68	266.30	0.202	16.552
^{13}CO 3- 2	330587.9601	61.758	122.29	186.72	0.469	16.84
^{13}CO 3- 2	330587.9601	45.246	93.42	288.31	0.445	16.85
CS 6- 5	293912.244	5.485	95.95	171.02	0.054	13.757
CS 6- 5	293912.244	6.401	105.28	259.98	0.057	14.136
CS 7- 6	342883	4.438	95.95	171.02	0.043	13.757
CS 7- 6	342883	3.561	105.28	259.98	0.032	14.136
$C^{34}S$ 6- 5	289209.23	0.875	95	214.34	0.009	12.860
$C^{34}S$ 6- 5	289209.23	0.063	105	159.67	0.001	12.860
$C^{34}S$ 7- 6	337396.6901	0.862	95	214.34	0.009	12.860
HCO^+v=0 1 2 4 0 0- 3 0 0	356734.134	24.680	87.31	176.76	0.264	13.419
HCO^+v=0 1 2 4 0 0- 3 0 0	356734.134	31.247	101.05	267.96	0.287	13.792
HCN 4- 3	354505.4759	11.561	96.75	171.98	0.112	13.314
HCN 4- 3	354505.4759	24.401	107.42	267.34	0.211	13.914
HNC 4- 3	362630.303	10.109	94.83	185.60	0.100	13.22
HNC 4- 3	362630.303	5.236	73.96	263.50	0.066	13.198
HNCO 13 0 13-12 0 12	285722.0543	0.485	90	185.89	0.005	14.959
HNCO 13 0 13-12 0 12	285722.0563	0.449	90	185.89	0.005	14.959
HNCO 13 0 13-12 0 12	285722.0588	0.415	90	185.89	0.004	14.959
HNCO 14 0 14-13 0 13	307694.0325	0.244	90	185.89	0.003	14.959
HNCO 14 0 14-13 0 13	307694.0342	0.227	90	185.89	0.002	14.959
HNCO 14 0 14-13 0 13	307694.0363	0.211	90	185.89	0.002	14.959
HNCO 15 0 15-14 0 14	329664.535	0.112	90	185.89	0.001	14.959
HNCO 15 0 15-14 0 14	329664.5366	0.105	90	185.89	0.001	14.959
HNCO 15 0 15-14 0 14	329664.5383	0.098	90	185.89	0.001	14.959
SO 1 1- 0 1	286340.207	0.078	100.90	181.09	0.001	13.832
SO 1 1- 0 1	286340.207	0.154	84.61	283.08	0.002	14.072
SO 7 6- 6 5	296550.045	0.602	100.90	181.09	0.006	13.832
SO 7 6- 6 5	296550.045	0.277	84.61	283.08	0.003	14.072
SO 7 7- 6 6	301286.124	0.535	100.90	181.09	0.005	13.832
SO 7 7- 6 6	301286.124	0.206	84.61	283.08	0.002	14.072
SO 7 8- 6 7	304077.844	0.992	100.90	181.09	0.009	13.832
SO 7 8- 6 7	304077.844	0.494	84.61	283.08	0.005	14.072
SO 2 2- 1 2	309502.444	0.100	100.90	181.09	0.001	13.832
SO 2 2- 1 2	309502.444	0.176	84.61	283.08	0.002	14.072
SO 2 1- 1 0	329385.477	0.068	100.90	181.09	0.001	13.832
SO 2 1- 1 0	329385.477	0.133	84.61	283.08	0.001	14.072

SO 3 3- 2 3	339341.459	0.097	100.90	181.09	0.001	13.832
SO 3 3- 2 3	339341.459	0.142	84.61	283.08	0.002	14.072
SO 8 7- 7 6	340714.155	0.415	100.90	181.09	0.004	13.832
SO 8 7- 7 6	340714.155	0.118	84.61	283.08	0.001	14.072
SO 8 8- 7 7	344310.612	0.353	100.90	181.09	0.003	13.832
SO 8 8- 7 7	344310.612	0.084	84.61	283.08	0.001	14.072
SO 8 9- 7 8	346528.481	0.634	100.90	181.09	0.006	13.832
SO 8 9- 7 8	346528.481	0.194	84.61	283.08	0.002	14.072
C_2H 4 5 5- 3 4 4	349337.4558	2.870	112.37	182.98	0.024	14.34
C_2H 4 5 5- 3 4 4	349337.4558	1.419	75.89	251.25	0.018	14.299
C_2H 4 5 4- 3 4 3	349338.7284	2.294	112.37	182.98	0.019	14.34
C_2H 4 5 4- 3 4 3	349338.7284	1.134	75.89	251.25	0.014	14.299
C_2H 4 4 4- 3 3 3	349398.9061	2.249	112.37	182.98	0.019	14.34
C_2H 4 4 4- 3 3 3	349398.9061	1.112	75.89	251.25	0.014	14.299
C_2H 4 4 3- 3 3 2	349400.2918	1.678	112.37	182.98	0.014	14.34
C_2H 4 4 3- 3 3 2	349400.2918	0.829	75.89	251.25	0.010	14.299
CH_2NH 2 1 2- 1 0 1	284253.1396	0.073	123.23	240.47	0.001	13.558
CH_2NH 2 1 2- 1 0 1	284253.4107	0.218	123.23	240.47	0.002	13.558
CH_2NH 2 1 2- 1 0 1	284254.2754	0.407	123.23	240.47	0.003	13.558
CH_2NH 2 1 2- 1 0 1	284254.4997	0.097	123.23	240.47	0.001	13.558
CH_2NH 2 1 2- 1 0 1	284255.1775	0.073	123.23	240.47	0.001	13.558
CH_2NH 5 1 5- 4 1 4	306172.3621	0.154	123.23	240.47	0.001	13.558
CH_2NH 5 1 5- 4 1 4	306172.3664	0.190	123.23	240.47	0.001	13.558
CH_2NH 5 1 5- 4 1 4	306172.4223	0.233	123.23	240.47	0.002	13.558
CH_2NH 5 0 5- 4 0 4	317405.1566	0.273	123.23	240.47	0.002	13.558
CH_2NH 5 0 5- 4 0 4	317405.241	0.221	123.23	240.47	0.002	13.558
CH_2NH 5 0 5- 4 0 4	317405.2471	0.337	123.23	240.47	0.003	13.558
CH_2NH 5 2 4- 4 2 3	319631.0867	0.080	123.23	240.47	0.001	13.558
CH_2NH 5 2 3- 4 2 2	322161.8424	0.080	123.23	240.47	0.001	13.558
CH_2NH 7 0 7- 6 1 6	325305.252	0.071	123.23	240.47	0.001	13.558
CH_2NH 5 1 4- 4 1 3	332573.0414	0.194	123.23	240.47	0.001	13.558
CH_2NH 5 1 4- 4 1 3	332573.0676	0.239	123.23	240.47	0.002	13.558
CH_2NH 5 1 4- 4 1 3	332573.1137	0.157	123.23	240.47	0.001	13.558
CH_2NH 3 1 3- 2 0 2	340353.3736	0.359	123.23	240.47	0.003	13.558
CH_2NH 3 1 3- 2 0 2	340354.3146	0.520	123.23	240.47	0.004	13.558
CH_2NH 3 1 3- 2 0 2	340354.5777	0.242	123.23	240.47	0.002	13.558
CH_2NH 6 1 6- 5 1 5	367072.3842	0.167	123.23	240.47	0.001	13.558
CH_2NH 6 1 6- 5 1 5	367072.3914	0.141	123.23	240.47	0.001	13.558
CH_2NH 6 1 6- 5 1 5	367072.432	0.199	123.23	240.47	0.002	13.558
CH_3CCH 17 2-16 2	290479.9316	1.059	120.6	674.43	0.008	15.561
CH_3CCH 17 2-16 2	290479.9316	0.137	113.4	282.41	0.001	16.620
CH_3CCH 17 1-16 1	290496.543	2.064	120.6	674.43	0.016	15.561
CH_3CCH 17 1-16 1	290496.543	0.586	113.4	282.41	0.005	16.620
CH_3CCH 17 0-16 0	290502.0809	2.577	120.6	674.43	0.020	15.561
CH_3CCH 17 0-16 0	290502.0809	0.950	113.4	282.41	0.008	16.620
CH_3CCH 18 2-17 2	307559.6032	0.813	120.6	674.43	0.006	15.561
CH_3CCH 18 2-17 2	307559.6032	0.062	113.4	282.41	0.001	16.620

CH_3CCH 18 1-17 1	307577.1847	1.583	120.6	674.43	0.012	15.561
CH_3CCH 18 1-17 1	307577.1847	0.264	113.4	282.41	0.002	16.620
CH_3CCH 18 0-17 0	307583.0459	1.977	120.6	674.43	0.015	15.561
CH_3CCH 18 0-17 0	307583.0459	0.427	113.4	282.41	0.004	16.620
CH_3CCH 19 1-18 1	324656.5622	1.169	120.6	674.43	0.009	15.561
CH_3CCH 19 1-18 1	324656.5622	0.111	113.4	282.41	0.001	16.620
CH_3CCH 19 0-18 0	324662.7465	1.460	120.6	674.43	0.011	15.561
CH_3CCH 19 0-18 0	324662.7465	0.179	113.4	282.41	0.001	16.620
CH_3CCH 20 0-19 0	341741.1132	1.039	120.6	674.43	0.008	15.561
CH_3CCH 20 0-19 0	341741.1132	0.071	113.4	282.41	0.001	16.620
H_2CO 4 1 4- 3 1 3	281526.929	0.936	68.67	172.97	0.013	13.01
H_2CO 4 1 4- 3 1 3	281526.929	2.057	112.85	291.73	0.017	13.59
H_2CO 4 0 4- 3 0 3	290623.405	0.505	68.67	172.97	0.007	13.01
H_2CO 4 0 4- 3 0 3	290623.405	1.698	112.85	291.73	0.014	13.59
H_2CO 4 2 3- 3 2 2	291237.78	0.083	68.67	172.97	0.001	13.01
H_2CO 4 2 2- 3 2 1	291948.06	0.083	68.67	172.97	0.001	13.01
H_2CO 4 1 3- 3 1 2	300836.635	1.008	68.67	172.97	0.014	13.01
H_2CO 4 1 3- 3 1 2	300836.635	2.022	112.85	291.73	0.017	13.59
H_2CO 5 1 5- 4 1 4	351768.645	1.121	68.67	172.97	0.015	13.01
H_2CO 5 1 5- 4 1 4	351768.645	1.266	112.85	291.73	0.011	13.59
H_2CO 5 0 5- 4 0 4	362736.048	0.575	68.67	172.97	0.008	13.01
H_2CO 5 0 5- 4 0 4	362736.048	0.973	112.85	291.73	0.008	13.59
H_2CO 5 2 4- 4 2 3	363945.894	0.105	68.67	172.97	0.001	13.01
H_2CO 5 2 3- 4 2 2	365363.428	0.106	68.67	172.97	0.001	13.01
H_2CS 8 0 8- 7 0 7	274520.8698	0.134	110.7	170	0.001	13.31
H_2CS 8 2 7- 7 2 6	274702.0548	0.072	110.7	170	0.001	13.31
H_2CS 8 2 6- 7 2 5	274952.473	0.072	110.7	170	0.001	13.31
H_2CS 8 1 7- 7 1 6	278886.4003	0.352	110.7	170	0.003	13.31
H_2CS 9 1 9- 8 1 8	304305.9748	0.421	110.7	170	0.004	13.31
H_2CS 9 0 9- 8 0 8	308748.0375	0.167	110.7	170	0.001	13.31
H_2CS 9 2 8- 8 2 7	309015.1908	0.091	110.7	170	0.001	13.31
H_2CS 9 2 7- 8 2 6	309372.6855	0.091	110.7	170	0.001	13.31
H_2CS 9 1 8- 8 1 7	313714.9072	0.439	110.7	170	0.004	13.31
H_2CS 10 1 10- 9 1 9	338080.8306	0.494	110.7	170	0.004	13.31
H_2CS 10 0 10- 9 0 9	342944.3689	0.194	110.7	170	0.002	13.31
H_2CS 10 2 9- 9 2 8	343319.6445	0.107	110.7	170	0.001	13.31
H_2CS 10 2 8- 9 2 7	343810.7553	0.107	110.7	170	0.001	13.31
H_2CS 10 1 9- 9 1 8	348531.8733	0.511	110.7	170	0.004	13.31
H_2CS 11 1 11-10 1 10	371844.2411	0.546	110.7	170	0.005	13.31
NH_2CN 14 1 14-13 1 13	278019.6584	0.750	148.43	283	0.005	13.746
NH_2CN 14 0 14-13 0 13	279818.8464	0.475	148.43	283	0.003	13.746
NH_2CN 14 1 13-13 1 12	281708.318	0.728	148.43	283	0.005	13.746
NH_2CN 15 1 15-14 1 14	297868.8474	0.494	148.43	283	0.003	13.746
NH_2CN 15 0 15-14 0 14	299786.8815	0.311	148.43	283	0.002	13.746
NH_2CN 15 1 14-14 1 13	301820.356	0.475	148.43	283	0.003	13.746
NH_2CN 16 1 16-15 1 15	317716.1094	0.306	148.43	283	0.002	13.746
NH_2CN 16 0 16-15 0 15	319750.9896	0.192	148.43	283	0.001	13.746

NH_2CN 16 1 15-15 1 14	321930.3198	0.292	148.43	283	0.002	13.746
NH_2CN 17 1 17-16 1 16	337561.319	0.179	148.43	283	0.001	13.746
NH_2CN 17 0 17-16 0 16	339710.9131	0.111	148.43	283	0.001	13.746
NH_2CN 17 1 16-16 1 15	342038.0685	0.169	148.43	283	0.001	13.746
SiO 7- 6	303926.96	0.422	100	238	0.004	13.000
SiO 8- 7	347330.631	0.176	100	238	0.002	13.000
CH_3OH 9 -1- 8 0	278304.512	0.070	62.30	172.13	0.001	14.118
CH_3OH 9 -1- 8 0	278304.512	0.067	98.39	266.02	0.001	14.335
CH_3OH 2 -2- 3 -1	278342.261	0.055	62.30	172.13	0.001	14.118
CH_3OH 2 -2- 3 -1	278342.261	0.100	98.39	266.02	0.001	14.335
CH_3OH 3 2 – 4 1 -	285111.111	0.064	62.30	172.13	0.001	14.118
CH_3OH 3 2 – 4 1 -	285111.111	0.100	98.39	266.02	0.001	14.335
CH_3OH 6 1 +- 5 1 +	287670.767	0.305	62.30	172.13	0.005	14.118
CH_3OH 6 1 +- 5 1 +	287670.767	0.433	98.39	266.02	0.004	14.335
CH_3OH 6 0- 5 0	289939.377	0.330	62.30	172.13	0.005	14.118
CH_3OH 6 0- 5 0	289939.377	0.472	98.39	266.02	0.005	14.335
CH_3OH 6 -1- 5 -1	290069.747	0.416	62.30	172.13	0.006	14.118
CH_3OH 6 -1- 5 -1	290069.747	0.633	98.39	266.02	0.006	14.335
CH_3OH 6 0 +- 5 0 +	290110.637	0.517	62.30	172.13	0.008	14.118
CH_3OH 6 0 +- 5 0 +	290110.637	0.825	98.39	266.02	0.008	14.335
CH_3OH 6 2 – 5 2 -	290184.674	0.128	62.30	172.13	0.002	14.118
CH_3OH 6 2 – 5 2 -	290184.674	0.149	98.39	266.02	0.001	14.335
CH_3OH 6 3 +- 5 3 +	290189.515	0.071	62.30	172.13	0.001	14.118
CH_3OH 6 3 +- 5 3 +	290189.515	0.075	98.39	266.02	0.001	14.335
CH_3OH 6 3 – 5 3 -	290190.549	0.071	62.30	172.13	0.001	14.118
CH_3OH 6 3 – 5 3 -	290190.549	0.075	98.39	266.02	0.001	14.335
CH_3OH 6 -3- 5 -3	290209.695	0.046	62.30	172.13	0.001	14.118
CH_3OH 6 3- 5 3	290213.18	0.076	62.30	172.13	0.001	14.118
CH_3OH 6 3- 5 3	290213.18	0.082	98.39	266.02	0.001	14.335
CH_3OH 6 1- 5 1	290248.685	0.252	62.30	172.13	0.004	14.118
CH_3OH 6 1- 5 1	290248.685	0.337	98.39	266.02	0.003	14.335
CH_3OH 6 2 +- 5 2 +	290264.068	0.128	62.30	172.13	0.002	14.118
CH_3OH 6 2 +- 5 2 +	290264.068	0.149	98.39	266.02	0.001	14.335
CH_3OH 6 -2- 5 -2	290307.281	0.191	62.30	172.13	0.003	14.118
CH_3OH 6 -2- 5 -2	290307.281	0.245	98.39	266.02	0.002	14.335
CH_3OH 6 2- 5 2	290307.738	0.213	62.30	172.13	0.003	14.118
CH_3OH 6 2- 5 2	290307.738	0.283	98.39	266.02	0.003	14.335
CH_3OH 6 1 – 5 1 -	292672.889	0.308	62.30	172.13	0.005	14.118
CH_3OH 6 1 – 5 1 -	292672.889	0.434	98.39	266.02	0.004	14.335
CH_3OH 3 2 +- 4 1 +	293464.055	0.068	62.30	172.13	0.001	14.118
CH_3OH 3 2 +- 4 1 +	293464.055	0.106	98.39	266.02	0.001	14.335
CH_3OH 3 0- 2 -1	302369.773	0.248	62.30	172.13	0.004	14.118
CH_3OH 3 0- 2 -1	302369.773	0.474	98.39	266.02	0.005	14.335
CH_3OH 1 1 – 1 0 +	303366.921	0.729	62.30	172.13	0.011	14.118
CH_3OH 1 1 – 1 0 +	303366.921	1.516	98.39	266.02	0.014	14.335
CH_3OH 2 1 – 2 0 +	304208.348	0.966	62.30	172.13	0.015	14.118
CH_3OH 2 1 – 2 0 +	304208.348	1.931	98.39	266.02	0.018	14.335

CH_3OH 3 1 – 3 0 +	305473.491	0.818	62.30	172.13	0.012	14.118
CH_3OH 3 1 – 3 0 +	305473.491	1.544	98.39	266.02	0.015	14.335
CH_3OH 4 1 – 4 0 +	307165.924	0.771	62.30	172.13	0.012	14.118
CH_3OH 4 1 – 4 0 +	307165.924	1.345	98.39	266.02	0.013	14.335
CH_3OH 5 1 – 5 0 +	309290.36	0.639	62.30	172.13	0.010	14.118
CH_3OH 5 1 – 5 0 +	309290.36	1.010	98.39	266.02	0.010	14.335
CH_3OH 3 1- 2 0	310192.994	0.351	62.30	172.13	0.005	14.118
CH_3OH 3 1- 2 0	310192.994	0.627	98.39	266.02	0.006	14.335
CH_3OH 6 1 – 6 0 +	311852.612	0.473	62.30	172.13	0.007	14.118
CH_3OH 6 1 – 6 0 +	311852.612	0.666	98.39	266.02	0.006	14.335
CH_3OH 7 1- 6 2	313596.76	0.070	62.30	172.13	0.001	14.118
CH_3OH 7 1- 6 2	313596.76	0.082	98.39	266.02	0.001	14.335
CH_3OH 7 1 – 7 0 +	314859.528	0.317	62.30	172.13	0.005	14.118
CH_3OH 7 1 – 7 0 +	314859.528	0.389	98.39	266.02	0.004	14.335
CH_3OH 6 2- 5 1	315266.861	0.253	62.30	172.13	0.004	14.118
CH_3OH 6 2- 5 1	315266.861	0.335	98.39	266.02	0.003	14.335
CH_3OH 8 1 – 8 0 +	318318.919	0.193	62.30	172.13	0.003	14.118
CH_3OH 8 1 – 8 0 +	318318.919	0.202	98.39	266.02	0.002	14.335
CH_3OH 9 1 – 9 0 +	322239.462	0.107	62.30	172.13	0.002	14.118
CH_3OH 9 1 – 9 0 +	322239.462	0.094	98.39	266.02	0.001	14.335
CH_3OH 10 1 –10 0 +	326630.583	0.054	62.30	172.13	0.001	14.118
CH_3OH 10 -1- 9 0	326961.232	0.052	62.30	172.13	0.001	14.118
CH_3OH 2 2 – 3 1 -	335133.57	0.051	62.30	172.13	0.001	14.118
CH_3OH 2 2 – 3 1 -	335133.57	0.084	98.39	266.02	0.001	14.335
CH_3OH 7 1 +- 6 1 +	335582.017	0.290	62.30	172.13	0.004	14.118
CH_3OH 7 1 +- 6 1 +	335582.017	0.359	98.39	266.02	0.003	14.335
CH_3OH 7 0- 6 0	338124.488	0.309	62.30	172.13	0.005	14.118
CH_3OH 7 0- 6 0	338124.488	0.386	98.39	266.02	0.004	14.335
CH_3OH 7 -1- 6 -1	338344.588	0.392	62.30	172.13	0.006	14.118
CH_3OH 7 -1- 6 -1	338344.588	0.522	98.39	266.02	0.005	14.335
CH_3OH 7 0 +- 6 0 +	338408.698	0.484	62.30	172.13	0.007	14.118
CH_3OH 7 0 +- 6 0 +	338408.698	0.675	98.39	266.02	0.006	14.335
CH_3OH 7 2 – 6 2 -	338512.853	0.124	62.30	172.13	0.002	14.118
CH_3OH 7 2 – 6 2 -	338512.853	0.126	98.39	266.02	0.001	14.335
CH_3OH 7 3 +- 6 3 +	338540.826	0.072	62.30	172.13	0.001	14.118
CH_3OH 7 3 +- 6 3 +	338540.826	0.066	98.39	266.02	0.001	14.335
CH_3OH 7 3 – 6 3 -	338543.152	0.072	62.30	172.13	0.001	14.118
CH_3OH 7 3 – 6 3 -	338543.152	0.066	98.39	266.02	0.001	14.335
CH_3OH 7 -3- 6 -3	338559.963	0.047	62.30	172.13	0.001	14.118
CH_3OH 7 3- 6 3	338583.216	0.078	62.30	172.13	0.001	14.118
CH_3OH 7 3- 6 3	338583.216	0.073	98.39	266.02	0.001	14.335
CH_3OH 7 1- 6 1	338614.936	0.237	62.30	172.13	0.004	14.118
CH_3OH 7 1- 6 1	338614.936	0.277	98.39	266.02	0.003	14.335
CH_3OH 7 2 +- 6 2 +	338639.802	0.124	62.30	172.13	0.002	14.118
CH_3OH 7 2 +- 6 2 +	338639.802	0.126	98.39	266.02	0.001	14.335
CH_3OH 7 2- 6 2	338721.693	0.206	62.30	172.13	0.003	14.118
CH_3OH 7 2- 6 2	338721.693	0.239	98.39	266.02	0.002	14.335

CH_3OH 7 -2- 6 -2	338722.898	0.184	62.30	172.13	0.003	14.118
CH_3OH 7 -2- 6 -2	338722.898	0.207	98.39	266.02	0.002	14.335
CH_3OH 2 2 +- 3 1 +	340141.143	0.053	62.30	172.13	0.001	14.118
CH_3OH 2 2 +- 3 1 +	340141.143	0.087	98.39	266.02	0.001	14.335
CH_3OH 7 1 – 6 1 -	341415.615	0.289	62.30	172.13	0.004	14.118
CH_3OH 7 1 – 6 1 -	341415.615	0.355	98.39	266.02	0.003	14.335
CH_3OH 4 0- 3 -1	350687.662	0.380	62.30	172.13	0.006	14.118
CH_3OH 4 0- 3 -1	350687.662	0.672	98.39	266.02	0.006	14.335
CH_3OH 1 1 +- 0 0 +	350905.1	0.941	62.30	172.13	0.014	14.118
CH_3OH 1 1 +- 0 0 +	350905.1	1.958	98.39	266.02	0.019	14.335
CH_3OH 4 1- 3 0	358605.799	0.432	62.30	172.13	0.007	14.118
CH_3OH 4 1- 3 0	358605.799	0.715	98.39	266.02	0.007	14.335
CH_3OH 8 1- 7 2	361852.195	0.060	62.30	172.13	0.001	14.118
CH_3OH 8 1- 7 2	361852.195	0.061	98.39	266.02	0.001	14.335
CH_3OH 7 2- 6 1	363739.868	0.212	62.30	172.13	0.003	14.118
CH_3OH 7 2- 6 1	363739.868	0.246	98.39	266.02	0.002	14.335
N_2H^+ + 3- 2	279511.701	2.471	79.19	178.42	0.029	12.591
N_2H^+ + 3- 2	279511.701	6.944	107.99	263.12	0.060	13.04
NO 4 -1 4- 3 1 3	350689.494	1.155	135.58	225.67	0.008	15.46
NO 4 -1 4- 3 1 3	350689.494	0.391	98.46	172.70	0.004	15.32
NO 4 -1 4- 3 1 3	350690.766	0.849	135.58	225.67	0.006	15.46
NO 4 -1 4- 3 1 3	350690.766	0.287	98.46	172.70	0.003	15.32
NO 4 -1 4- 3 1 3	350694.772	0.616	135.58	225.67	0.004	15.46
NO 4 -1 4- 3 1 3	350694.772	0.208	98.46	172.70	0.002	15.32
NO 4 -1 4- 3 1 3	350729.583	0.075	135.58	225.67	0.001	15.46
NO 4 -1 4- 3 1 3	350736.778	0.075	135.58	225.67	0.001	15.46
NO 4 1 4- 3 -1 3	350963.37	0.075	135.58	225.67	0.001	15.46
NO 4 1 4- 3 -1 3	350989.583	0.075	135.58	225.67	0.001	15.46
NO 4 1 4- 3 -1 3	351043.524	1.155	135.58	225.67	0.008	15.46
NO 4 1 4- 3 -1 3	351043.524	0.389	98.46	172.70	0.004	15.32
NO 4 1 4- 3 -1 3	351051.469	0.849	135.58	225.67	0.006	15.46
NO 4 1 4- 3 -1 3	351051.469	0.286	98.46	172.70	0.003	15.32
NO 4 1 4- 3 -1 3	351051.705	0.616	135.58	225.67	0.004	15.46
NO 4 1 4- 3 -1 3	351051.705	0.208	98.46	172.70	0.002	15.32
CN v=0 1 3 0 3- 2 0 3	339446.777	0.081	74.88	168.87	0.001	13.957
CN v=0 1 3 0 3- 2 0 3	339446.777	0.157	100.93	254.55	0.001	14.407
CN v=0 1 3 0 3- 2 0 3	339475.904	0.113	74.88	168.87	0.001	13.957
CN v=0 1 3 0 3- 2 0 3	339475.904	0.221	100.93	254.55	0.002	14.407
CN v=0 1 3 0 3- 2 0 3	339516.658	0.180	74.88	168.87	0.002	13.957
CN v=0 1 3 0 3- 2 0 3	339516.658	0.351	100.93	254.55	0.003	14.407
CN v=0 1 3 0 3- 2 0 2	340008.097	0.330	74.88	168.87	0.004	13.957
CN v=0 1 3 0 3- 2 0 2	340008.097	0.643	100.93	254.55	0.006	14.407
CN v=0 1 3 0 3- 2 0 2	340019.602	0.329	74.88	168.87	0.004	13.957
CN v=0 1 3 0 3- 2 0 2	340019.602	0.641	100.93	254.55	0.006	14.407
CN v=0 1 3 0 3- 2 0 2	340031.544	2.727	74.88	168.87	0.034	13.957
CN v=0 1 3 0 3- 2 0 2	340031.544	5.296	100.93	254.55	0.049	14.407
CN v=0 1 3 0 3- 2 0 2	340035.408	1.024	74.88	168.87	0.013	13.957

CN v=0 1 3 0 3- 2 0 2	340035.408	1.993	100.93	254.55	0.019	14.407
CN v=0 1 3 0 3- 2 0 2	340035.408	1.719	74.88	168.87	0.022	13.957
CN v=0 1 3 0 3- 2 0 2	340035.408	3.343	100.93	254.55	0.031	14.407
CN v=0 1 3 0 4- 2 0 3	340247.77	2.687	74.88	168.87	0.034	13.957
CN v=0 1 3 0 4- 2 0 3	340247.77	5.214	100.93	254.55	0.048	14.407
CN v=0 1 3 0 4- 2 0 3	340247.77	3.653	74.88	168.87	0.046	13.957
CN v=0 1 3 0 4- 2 0 3	340247.77	7.083	100.93	254.55	0.066	14.407
CN v=0 1 3 0 4- 2 0 3	340248.5764	1.951	74.88	168.87	0.024	13.957
CN v=0 1 3 0 4- 2 0 3	340248.5764	3.788	100.93	254.55	0.035	14.407
CN v=0 1 3 0 4- 2 0 3	340261.818	0.238	74.88	168.87	0.003	13.957
CN v=0 1 3 0 4- 2 0 3	340261.818	0.463	100.93	254.55	0.004	14.407
CN v=0 1 3 0 4- 2 0 3	340265.025	0.237	74.88	168.87	0.003	13.957
CN v=0 1 3 0 4- 2 0 3	340265.025	0.462	100.93	254.55	0.004	14.407
SO_2 11 4 8-11 3 9	357387.57	0.172	115	250.93	0.001	14.766
SO_2 8 4 4- 8 3 5	357581.4483	0.720	115	250.93	0.006	14.766
SO_2 9 4 6- 9 3 7	357671.78	0.485	115	250.93	0.004	14.766
SO_2 7 4 4- 7 3 5	357892.442	0.974	115	250.93	0.008	14.766
SO_2 6 4 2- 6 3 3	357925.96	1.173	115	250.93	0.010	14.766
SO_2 5 4 2- 5 3 3	358013.09	1.200	115	250.93	0.010	14.766
SO_2 4 4 0- 4 3 1	358038.08	0.886	115	250.93	0.007	14.766
OCS 23-22	279685.318	2.248	200	250	0.011	14.69
OCS 24-23	291839.673	2.291	200	250	0.011	14.69
NS v=0 7 1 7- 6 -1 6	299699.781	0.184	180	200	0.001	13.500
NS v=0 7 1 7- 6 -1 6	299699.781	0.157	180	200	0.001	13.500
NS v=0 7 1 7- 6 -1 6	299700.901	0.134	180	200	0.001	13.500
NS v=0 7 -1 7- 6 1 6	300097.098	0.183	180	200	0.001	13.500
NS v=0 7 -1 7- 6 1 6	300098.611	0.156	180	200	0.001	13.500
NS v=0 7 -1 7- 6 1 6	300098.611	0.133	180	200	0.001	13.500

Table 8.1: NGC 253 Gaussian fit.

Molecule Transition	ν (MHz)	AREA (mK Km s^{-1})	$\Delta V_{1/2}$ (km s^{-1})	V_{LSR} (km s^{-1})	T_{MB} K	N (cm^{-2})
CS 6- 5	293912.244	4.298	114.671	237.74	0.035	13.504
CS 6- 5	293912.244	4.325	118.895	482.681	0.034	13.482
CS 6- 5	293912.244	2.984	97.142	673.215	0.029	13.295
CS 7- 6	342883	4.115	114.671	237.74	0.034	13.504
CS 7- 6	342883	4.391	118.895	482.681	0.035	13.482
CS 7- 6	342883	3.411	97.142	673.215	0.033	13.295
CO 3- 2	345795.9899	538.648	114.671	295.302	4.11	17.729
CO 3- 2	345795.9899	549.111	120.306	515.999	4.045	17.727
CO 3- 2	345795.9899	248.911	72.717	695.102	3.123	17.385
HNC 3- 2	271981.142	9.524	114.671	217.714	0.078	13.397
HNC 3- 2	271981.142	4.755	118.895	378.283	0.038	12.997
HNC 3- 2	271981.142	9.031	97.142	647.645	0.087	13.35
HNC 4- 3	362630.303	6.396	114.671	217.714	0.052	13.397

HNC 4- 3	362630.303	4.405	118.895	378.283	0.035	12.997
HNC 4- 3	362630.303	6.528	97.142	647.645	0.063	13.35
HCN 4- 3	354505.4759	17.716	114.671	425.735	0.145	13.416
HCN 4- 3	354505.4759	12.133	118.895	553.655	0.096	13.236
HCN 4- 3	354505.4759	16.327	97.142	696.124	0.158	13.36
HCO^+v=0 1 2 4 0 0- 3 0 0	356734.134	19.206	120	367.013	0.15	13.22
HCO^+v=0 1 2 4 0 0- 3 0 0	356734.134	13.847	118.895	511.591	0.109	13.062
HCO^+v=0 1 2 4 0 0- 3 0 0	356734.134	18.927	97.142	668.467	0.183	13.192
$C^{18}O$ 3- 2	329330.5453	21.401	114.671	417.363	0.175	16.315
$C^{18}O$ 3- 2	329330.5453	15.332	118.895	558.953	0.121	16.171
$C^{18}O$ 3- 2	329330.5453	14.659	93.372086	698.444	0.147	16.18
$C^{17}O$ 3- 2	337061.1298	2.518	114.671	454.137	0.021	15.365
$C^{17}O$ 3- 2	337061.1298	1.487	118.895	581.643	0.012	15.137
$C^{17}O$ 3- 2	337061.1298	1.601	97.142	684.78	0.015	15.195
^{13}CO 3- 2	330587.9601	54.238	114.671	358.576	0.441	16.719
^{13}CO 3- 2	330587.9601	37.67	118.895	522.507	0.296	16.56
^{13}CO 3- 2	330587.9601	34.541	97.142	688.879	0.333	16.55
CN v=0 1 3 0 3- 2 0 3	339446.777	0.123	114.671	378.288	0.001	14.089
CN v=0 1 3 0 3- 2 0 3	339446.777	0.126	97.142	691.905	0.0012	14.124
CN v=0 1 3 0 3- 2 0 3	339475.904	0.173	114.671	378.288	0.0014	14.089
CN v=0 1 3 0 3- 2 0 3	339475.904	0.067	118.895	431.607	0.0005	13.676
CN v=0 1 3 0 3- 2 0 3	339475.904	0.177	97.142	691.905	0.0017	14.124
CN v=0 1 3 0 3- 2 0 3	339516.658	0.276	114.671	378.288	0.0023	14.089
CN v=0 1 3 0 3- 2 0 3	339516.658	0.107	118.895	431.607	0.0008	13.676
CN v=0 1 3 0 3- 2 0 3	339516.658	0.282	97.142	691.905	0.0027	14.124
CN v=0 1 3 0 3- 2 0 2	340008.097	0.505	114.671	378.288	0.0041	14.089
CN v=0 1 3 0 3- 2 0 2	340008.097	0.195	118.895	431.607	0.0015	13.676
CN v=0 1 3 0 3- 2 0 2	340008.097	0.516	97.142	691.905	0.005	14.124
CN v=0 1 3 0 3- 2 0 2	340019.602	0.503	114.671	378.288	0.0041	14.089
CN v=0 1 3 0 3- 2 0 2	340019.602	0.195	118.895	431.607	0.0015	13.676
CN v=0 1 3 0 3- 2 0 2	340019.602	0.514	97.142	691.905	0.005	14.124
CN v=0 1 3 0 3- 2 0 2	340031.544	4.171	114.671	378.288	0.0342	14.089
CN v=0 1 3 0 3- 2 0 2	340031.544	1.613	118.895	431.607	0.0127	13.676
CN v=0 1 3 0 3- 2 0 2	340031.544	4.264	97.142	691.905	0.0412	14.124
CN v=0 1 3 0 3- 2 0 2	340035.408	1.567	114.671	378.288	0.0128	14.089
CN v=0 1 3 0 3- 2 0 2	340035.408	0.606	118.895	431.607	0.0048	13.676
CN v=0 1 3 0 3- 2 0 2	340035.408	1.602	97.142	691.905	0.0155	14.124
CN v=0 1 3 0 3- 2 0 2	340035.408	2.63	114.671	378.288	0.0215	14.089
CN v=0 1 3 0 3- 2 0 2	340035.408	1.017	118.895	431.607	0.008	13.676
CN v=0 1 3 0 3- 2 0 2	340035.408	2.688	97.142	691.905	0.026	14.124
CN v=0 1 3 0 4- 2 0 3	340247.77	4.112	114.671	378.288	0.0337	14.089
CN v=0 1 3 0 4- 2 0 3	340247.77	1.59	118.895	431.607	0.0126	13.676
CN v=0 1 3 0 4- 2 0 3	340247.77	4.205	97.142	691.905	0.0407	14.124
CN v=0 1 3 0 4- 2 0 3	340247.77	5.591	114.671	378.288	0.0458	14.089
CN v=0 1 3 0 4- 2 0 3	340247.77	2.163	118.895	431.607	0.0171	13.676
CN v=0 1 3 0 4- 2 0 3	340247.77	5.719	97.142	691.905	0.0553	14.124
CN v=0 1 3 0 4- 2 0 3	340248.5764	2.985	114.671	378.288	0.0244	14.089

CN v=0 1 3 0 4- 2 0 3	340248.5764	1.154	118.895	431.607	0.0091	13.676
CN v=0 1 3 0 4- 2 0 3	340248.5764	3.052	97.142	691.905	0.0295	14.124
CN v=0 1 3 0 4- 2 0 3	340261.818	0.364	114.671	378.288	0.003	14.089
CN v=0 1 3 0 4- 2 0 3	340261.818	0.141	118.895	431.607	0.0011	13.676
CN v=0 1 3 0 4- 2 0 3	340261.818	0.372	97.142	691.9045	0.0036	14.124
CN v=0 1 3 0 4- 2 0 3	340265.025	0.363	114.671	378.288	0.003	14.089
CN v=0 1 3 0 4- 2 0 3	340265.025	0.14	118.895	431.607	0.0011	13.676
CN v=0 1 3 0 4- 2 0 3	340265.025	0.371	97.142	691.905	0.0036	14.124
SO_2 7 2 6- 6 1 5	271529.0152	0.909	114.671	635.66	0.0074	14.1
SO_2 15 3 13-15 2 14	275240.182	0.131	114.671	635.66	0.0011	14.1
SO_2 15 1 15-14 0 14	281762.6	0.448	114.671	635.66	0.0037	14.1
SO_2 6 2 4- 5 1 5	282036.58	0.844	114.671	635.66	0.0069	14.1
SO_2 16 0 16-15 1 15	283464.6	0.321	114.671	635.66	0.0026	14.1
SO_2 9 2 8- 8 1 7	298576.3083	0.852	114.671	635.66	0.007	14.1
SO_2 3 3 1- 2 2 0	313279.7183	1.478	114.671	635.66	0.0121	14.1
SO_2 17 1 17-16 0 16	313660.8505	0.27	114.671	635.66	0.0022	14.1
SO_2 18 0 18-17 1 17	321330.1645	0.187	114.671	635.66	0.0015	14.1
SO_2 11 2 10-10 1 9	323026.4609	0.678	114.671	635.66	0.0056	14.1
SO_2 4 3 1- 3 2 2	332505.2422	1.551	114.671	635.66	0.0127	14.1
SO_2 8 2 6- 7 1 7	334673.3518	0.774	114.671	635.66	0.0063	14.1
SO_2 13 2 12-12 1 11	345338.5391	0.467	114.671	635.66	0.0038	14.1
SO_2 16 4 12-16 3 13	346523.8776	0.086	114.671	635.66	0.0007	14.1
SO_2 5 3 3- 4 2 2	351257.224	1.585	114.671	635.66	0.013	14.1
SO_2 14 4 10-14 3 11	351873.8725	0.184	114.671	635.66	0.0015	14.1
SO_2 12 4 8-12 3 9	355045.5162	0.34	114.671	635.66	0.0028	14.1
SO_2 10 4 6-10 3 7	356755.1893	0.534	114.671	635.66	0.0044	14.1
SO_2 13 4 10-13 3 11	357165.36	0.259	114.671	635.66	0.0021	14.1
SO_2 15 4 12-15 3 13	357241.19	0.132	114.671	635.66	0.0011	14.1
SO_2 11 4 8-11 3 9	357387.57	0.438	114.671	635.66	0.0036	14.1
SO_2 8 4 4- 8 3 5	357581.4483	0.695	114.671	635.66	0.0057	14.1
SO_2 9 4 6- 9 3 7	357671.78	0.627	114.671	635.66	0.0051	14.1
SO_2 7 4 4- 7 3 5	357892.442	0.727	114.671	635.66	0.006	14.1
SO_2 6 4 2- 6 3 3	357925.96	0.698	114.671	635.66	0.0057	14.1
SO_2 5 4 2- 5 3 3	358013.09	0.588	114.671	635.66	0.0048	14.1
SO_2 4 4 0- 4 3 1	358038.08	0.37	114.671	635.66	0.003	14.1
SO_2 15 2 14-14 1 13	366214.4708	0.281	114.671	635.66	0.0023	14.1
SO_2 6 3 3- 5 2 4	371172.452	1.569	114.671	635.66	0.0129	14.1
H_2CO 4 1 4- 3 1 3	281526.929	1.261	114.671	377.44	0.0103	13.101
H_2CO 4 1 4- 3 1 3	281526.929	1.505	118.895	537.42	0.0119	13.187
H_2CO 4 1 4- 3 1 3	281526.929	0.922	97.142	716.22	0.0089	13.026
H_2CO 4 0 4- 3 0 3	290623.405	0.672	114.671	377.44	0.0055	13.101
H_2CO 4 0 4- 3 0 3	290623.405	0.772	118.895	537.42	0.0061	13.187
H_2CO 4 0 4- 3 0 3	290623.405	0.438	97.142	716.22	0.0042	13.026
H_2CO 4 2 3- 3 2 2	291237.78	0.115	114.671	377.44	0.0009	13.101
H_2CO 4 2 3- 3 2 2	291237.78	0.156	118.895	537.42	0.0012	13.187
H_2CO 4 2 3- 3 2 2	291237.78	0.125	97.142	716.22	0.0012	13.026
H_2CO 4 3 2- 3 3 1	291380.488	0.065	97.142	716.22	0.0006	13.026

H_2CO 4 3 1- 3 3 0	291384.264	0.065	97.142	716.22	0.0006	13.026
H_2CO 4 2 2- 3 2 1	291948.06	0.115	114.671	377.44	0.0009	13.101
H_2CO 4 2 2- 3 2 1	291948.06	0.157	118.895	537.42	0.0012	13.187
H_2CO 4 2 2- 3 2 1	291948.06	0.125	97.142	716.22	0.0012	13.026
H_2CO 4 1 3- 3 1 2	300836.635	1.354	114.671	377.44	0.0111	13.101
H_2CO 4 1 3- 3 1 2	300836.635	1.629	118.895	537.42	0.0129	13.187
H_2CO 4 1 3- 3 1 2	300836.635	1.014	97.142	716.22	0.0098	13.026
H_2CO 5 1 5- 4 1 4	351768.645	1.511	114.671	377.44	0.0124	13.101
H_2CO 5 1 5- 4 1 4	351768.645	1.914	118.895	537.42	0.0151	13.187
H_2CO 5 1 5- 4 1 4	351768.645	1.324	97.142	716.22	0.0128	13.026
H_2CO 5 0 5- 4 0 4	362736.048	0.766	114.671	377.44	0.0063	13.101
H_2CO 5 0 5- 4 0 4	362736.048	0.936	118.895	537.42	0.0074	13.187
H_2CO 5 0 5- 4 0 4	362736.048	0.601	97.142	716.22	0.0058	13.026
H_2CO 5 2 4- 4 2 3	363945.894	0.147	114.671	377.44	0.0012	13.101
H_2CO 5 2 4- 4 2 3	363945.894	0.212	118.895	537.42	0.0017	13.187
H_2CO 5 2 4- 4 2 3	363945.894	0.192	97.142	716.22	0.0019	13.026
H_2CO 5 3 3- 4 3 2	364275.141	0.094	118.895	537.42	0.0007	13.187
H_2CO 5 3 3- 4 3 2	364275.141	0.13	97.142	716.22	0.0013	13.026
H_2CO 5 3 2- 4 3 1	364288.884	0.094	118.895	537.42	0.0007	13.187
H_2CO 5 3 2- 4 3 1	364288.884	0.131	97.142	716.22	0.0013	13.026
H_2CO 5 2 3- 4 2 2	365363.428	0.147	114.671	377.44	0.0012	13.101
H_2CO 5 2 3- 4 2 2	365363.428	0.213	118.895	537.42	0.0017	13.187
H_2CO 5 2 3- 4 2 2	365363.428	0.193	97.142	716.22	0.0019	13.026
SO 7 6- 6 5	296550.045	0.587	200	418.885	0.0028	13.868
SO 7 7- 6 6	301286.124	0.507	200	418.885	0.0024	13.868
SO 7 8- 6 7	304077.844	0.978	200	418.885	0.0046	13.868
SO 2 2- 1 2	309502.444	0.12	200	418.885	0.0006	13.868
SO 8 8- 7 7	344310.612	0.306	200	418.885	0.0014	13.868
C_2H 4 5 5- 3 4 4	349337.4558	2.237	114.671	454.137	0.0183	14.188
C_2H 4 5 5- 3 4 4	349337.4558	2.054	118.895	581.643	0.0162	14.137
C_2H 4 5 5- 3 4 4	349337.4558	1.603	97.142	684.78	0.0155	14.026
C_2H 4 5 4- 3 4 3	349338.7284	1.788	114.671	454.137	0.0146	14.188
C_2H 4 5 4- 3 4 3	349338.7284	1.281	97.142	684.78	0.0124	14.026
C_2H 4 4 4- 3 3 3	349398.9061	1.61	118.895	581.643	0.0127	14.137
C_2H 4 4 4- 3 3 3	349398.9061	1.256	97.142	684.78	0.0121	14.026
C_2H 4 4 3- 3 3 2	349400.2918	1.308	114.671	454.137	0.0107	14.188
C_2H 4 4 3- 3 3 2	349400.2918	1.201	118.895	581.643	0.0095	14.137
C_2H 4 4 3- 3 3 2	349400.2918	0.937	97.142	684.78	0.0091	14.026
c-C_3H_2 8 1 8- 7 0 7	284805.2056	1.444	300	621.094	0.0045	13.418
c-C_3H_2 8 0 8- 7 1 7	284805.2053	0.481	300	621.094	0.0015	13.418
c-C_3H_2 6 2 4- 5 3 3	284913.0055	0.301	300	621.094	0.0009	13.418
c-C_3H_2 7 1 6- 6 2 5	284998.0002	1.162	300	621.094	0.0036	13.418
c-C_3H_2 7 2 6- 6 1 5	284999.3518	0.387	300	621.094	0.0012	13.418
c-C_3H_2 6 3 4- 5 2 3	285795.6688	0.911	300	621.094	0.0029	13.418
c-C_3H_2 5 4 2- 4 3 1	300191.7052	0.298	300	621.094	0.0009	13.418
c-C_3H_2 6 3 3- 5 4 2	312709.5738	0.202	300	621.094	0.0006	13.418
c-C_3H_2 9 0 9- 8 1 8	318294.3682	1.284	300	621.094	0.004	13.418

c-C_3H_2 9 1 9- 8 0 8	318294.3682	0.428	300	621.094	0.0013	13.418
c-C_3H_2 8 1 7- 7 2 6	318482.2636	0.359	300	621.094	0.0011	13.418
c-C_3H_2 8 2 7- 7 1 6	318482.3526	1.078	300	621.094	0.0034	13.418
c-C_3H_2 7 2 5- 6 3 4	318696.9695	0.913	300	621.094	0.0029	13.418
c-C_3H_2 7 3 5- 6 2 4	318790.2377	0.305	300	621.094	0.001	13.418
c-C_3H_2 6 4 3- 5 3 2	326152.758	0.755	300	621.094	0.0024	13.418
c-C_3H_2 4 4 1- 3 1 2	336948.5895	0.17	300	621.094	0.0005	13.418
c-C_3H_2 5 5 1- 4 4 0	338203.9881	0.551	300	621.094	0.0017	13.418
c-C_3H_2 5 5 0- 4 4 1	349263.9776	1.638	300	621.094	0.0051	13.418
c-C_3H_2 7 3 4- 6 4 3	351523.2708	0.687	300	621.094	0.0022	13.418
c-C_3H_2 10 1 10- 9 0 9	351781.5686	1.034	300	621.094	0.0032	13.418
c-C_3H_2 10 0 10- 9 1 9	351781.5686	0.345	300	621.094	0.0011	13.418
c-C_3H_2 9 2 8- 8 1 7	351965.939	0.299	300	621.094	0.0009	13.418
c-C_3H_2 9 1 8- 8 2 7	351965.9336	0.896	300	621.094	0.0028	13.418
c-C_3H_2 8 2 6- 7 3 5	352185.5135	0.268	300	621.094	0.0008	13.418
c-C_3H_2 8 3 6- 7 2 5	352193.6357	0.803	300	621.094	0.0025	13.418
c-C_3H_2 7 4 4- 6 3 3	354142.9712	0.234	300	621.094	0.0007	13.418
c-C_3H_2 5 4 1- 4 3 2	368293.6196	0.607	300	621.094	0.0019	13.418
c-C_3H_2 7 4 3- 6 5 2	373669.9511	0.385	300	621.094	0.0012	13.418
c-C_3H_2 6 5 2- 5 4 1	374357.6975	0.906	300	621.094	0.0028	13.418
N_2H^+ + 3- 2	279511.701	3.496	114.671	454.137	0.0286	12.736
N_2H^+ + 3- 2	279511.701	3.347	118.895	581.643	0.0264	12.718
N_2H^+ + 3- 2	279511.701	2.941	97.142	684.78	0.0284	12.662
N_2H^+ + 4- 3	372672.509	3.296	114.671	454.137	0.027	12.736
N_2H^+ + 4- 3	372672.509	3.156	118.895	581.643	0.0249	12.718
N_2H^+ + 4- 3	372672.509	2.773	97.142	684.78	0.0268	12.662
CH_3OH 6 1 +- 5 1 +	287670.767	0.206	114.671	454.137	0.0017	14.059
CH_3OH 6 1 +- 5 1 +	287670.767	0.116	118.895	581.643	0.0009	13.811
CH_3OH 6 1 +- 5 1 +	287670.767	0.145	97.142	684.78	0.0014	13.906
CH_3OH 6 0- 5 0	289939.377	0.226	114.671	454.137	0.0019	14.059
CH_3OH 6 0- 5 0	289939.377	0.128	118.895	581.643	0.001	13.811
CH_3OH 6 0- 5 0	289939.377	0.159	97.142	684.78	0.0015	13.906
CH_3OH 6 -1- 5 -1	290069.747	0.321	114.671	454.137	0.0026	14.059
CH_3OH 6 -1- 5 -1	290069.747	0.182	118.895	581.643	0.0014	13.811
CH_3OH 6 -1- 5 -1	290069.747	0.226	97.142	684.78	0.0022	13.906
CH_3OH 6 0 +- 5 0 +	290110.637	0.437	114.671	454.137	0.0036	14.059
CH_3OH 6 0 +- 5 0 +	290110.637	0.247	118.895	581.643	0.0019	13.811
CH_3OH 6 0 +- 5 0 +	290110.637	0.307	97.142	684.78	0.003	13.906
CH_3OH 6 1- 5 1	290248.685	0.152	114.671	454.137	0.0012	14.059
CH_3OH 6 1- 5 1	290248.685	0.086	118.895	581.643	0.0007	13.811
CH_3OH 6 1- 5 1	290248.685	0.107	97.142	684.78	0.001	13.906
CH_3OH 6 -2- 5 -2	290307.281	0.107	114.671	454.137	0.0009	14.059
CH_3OH 6 -2- 5 -2	290307.281	0.075	97.142	684.78	0.0007	13.906
CH_3OH 6 2- 5 2	290307.738	0.126	114.671	454.137	0.001	14.059
CH_3OH 6 2- 5 2	290307.738	0.071	118.895	581.643	0.0006	13.811
CH_3OH 6 2- 5 2	290307.738	0.089	97.142	684.78	0.0009	13.906
CH_3OH 6 1 – 5 1 -	292672.889	0.205	114.671	454.137	0.0017	14.059

CH_3OH 6 1 – 5 1 -	292672.889	0.116	118.895	581.643	0.0009	13.811
CH_3OH 6 1 – 5 1 -	292672.889	0.144	97.142	684.78	0.0014	13.906
CH_3OH 3 0- 2 -1	302369.773	0.295	114.671	454.137	0.0024	14.059
CH_3OH 3 0- 2 -1	302369.773	0.167	118.895	581.643	0.0013	13.811
CH_3OH 3 0- 2 -1	302369.773	0.207	97.142	684.78	0.002	13.906
CH_3OH 1 1 – 1 0 +	303366.921	1.018	114.671	454.137	0.0083	14.059
CH_3OH 1 1 – 1 0 +	303366.921	0.575	118.895	581.643	0.0045	13.811
CH_3OH 1 1 – 1 0 +	303366.921	0.715	97.142	684.78	0.0069	13.906
CH_3OH 2 1 – 2 0 +	304208.348	1.252	114.671	454.137	0.0103	14.059
CH_3OH 2 1 – 2 0 +	304208.348	0.707	118.895	581.643	0.0056	13.811
CH_3OH 2 1 – 2 0 +	304208.348	0.88	97.142	684.78	0.0085	13.906
CH_3OH 3 1 – 3 0 +	305473.491	0.949	114.671	454.137	0.0078	14.059
CH_3OH 3 1 – 3 0 +	305473.491	0.536	118.895	581.643	0.0042	13.811
CH_3OH 3 1 – 3 0 +	305473.491	0.666	97.142	684.78	0.0064	13.906
CH_3OH 4 1 – 4 0 +	307165.924	0.77	114.671	454.137	0.0063	14.059
CH_3OH 4 1 – 4 0 +	307165.924	0.435	118.895	581.643	0.0034	13.811
CH_3OH 4 1 – 4 0 +	307165.924	0.541	97.142	684.78	0.0052	13.906
CH_3OH 5 1 – 5 0 +	309290.36	0.529	114.671	454.137	0.0043	14.059
CH_3OH 5 1 – 5 0 +	309290.36	0.299	118.895	581.643	0.0024	13.811
CH_3OH 5 1 – 5 0 +	309290.36	0.372	97.142	684.78	0.0036	13.906
CH_3OH 3 1- 2 0	310192.994	0.367	114.671	454.137	0.003	14.059
CH_3OH 3 1- 2 0	310192.994	0.207	118.895	581.643	0.0016	13.811
CH_3OH 3 1- 2 0	310192.994	0.258	97.142	684.78	0.0025	13.906
CH_3OH 6 1 – 6 0 +	311852.612	0.313	114.671	454.137	0.0026	14.059
CH_3OH 6 1 – 6 0 +	311852.612	0.177	118.895	581.643	0.0014	13.811
CH_3OH 6 1 – 6 0 +	311852.612	0.22	97.142	684.78	0.0021	13.906
CH_3OH 7 1 – 7 0 +	314859.528	0.162	114.671	454.137	0.0013	14.059
CH_3OH 7 1 – 7 0 +	314859.528	0.091	118.895	581.643	0.0007	13.811
CH_3OH 7 1 – 7 0 +	314859.528	0.113	97.142	684.78	0.0011	13.906
CH_3OH 6 2- 5 1	315266.861	0.149	114.671	454.137	0.0012	14.059
CH_3OH 6 2- 5 1	315266.861	0.084	118.895	581.643	0.0007	13.811
CH_3OH 6 2- 5 1	315266.861	0.105	97.142	684.78	0.001	13.906
CH_3OH 8 1 – 8 0 +	318318.919	0.073	114.671	454.137	0.0006	14.059
CH_3OH 7 1 +- 6 1 +	335582.017	0.15	114.671	454.137	0.0012	14.059
CH_3OH 7 1 +- 6 1 +	335582.017	0.085	118.895	581.643	0.0007	13.811
CH_3OH 7 1 +- 6 1 +	335582.017	0.105	97.142	684.78	0.001	13.906
CH_3OH 7 0- 6 0	338124.488	0.162	114.671	454.137	0.0013	14.059
CH_3OH 7 0- 6 0	338124.488	0.091	118.895	581.643	0.0007	13.811
CH_3OH 7 0- 6 0	338124.488	0.114	97.142	684.78	0.0011	13.906
CH_3OH 7 -1- 6 -1	338344.588	0.232	114.671	454.137	0.0019	14.059
CH_3OH 7 -1- 6 -1	338344.588	0.131	118.895	581.643	0.001	13.811
CH_3OH 7 -1- 6 -1	338344.588	0.163	97.142	684.78	0.0016	13.906
CH_3OH 7 0 +- 6 0 +	338408.698	0.313	114.671	454.137	0.0026	14.059
CH_3OH 7 0 +- 6 0 +	338408.698	0.176	118.895	581.643	0.0014	13.811
CH_3OH 7 0 +- 6 0 +	338408.698	0.22	97.142	684.78	0.0021	13.906
CH_3OH 7 1- 6 1	338614.936	0.11	114.671	454.137	0.0009	14.059
CH_3OH 7 1- 6 1	338614.936	0.077	97.142	684.78	0.0007	13.906

CH_3OH 7 2- 6 2	338721.693	0.093	114.671	454.137	0.0008	14.059
CH_3OH 7 2- 6 2	338721.693	0.066	97.142	684.78	0.0006	13.906
CH_3OH 7 -2- 6 -2	338722.898	0.079	114.671	454.137	0.0006	14.059
CH_3OH 7 -2- 6 -2	338722.898	0.055	97.142	684.78	0.0005	13.906
CH_3OH 7 1 – 6 1 -	341415.615	0.147	114.671	454.137	0.0012	14.059
CH_3OH 7 1 – 6 1 -	341415.615	0.083	118.895	581.643	0.0007	13.811
CH_3OH 7 1 – 6 1 -	341415.615	0.103	97.142	684.78	0.001	13.906
CH_3OH 4 0- 3 -1	350687.662	0.386	114.671	454.137	0.0032	14.059
CH_3OH 4 0- 3 -1	350687.662	0.218	118.895	581.643	0.0017	13.811
CH_3OH 4 0- 3 -1	350687.662	0.271	97.142	684.78	0.0026	13.906
CH_3OH 1 1 +- 0 0 +	350905.1	1.302	114.671	454.137	0.0107	14.059
CH_3OH 1 1 +- 0 0 +	350905.1	0.736	118.895	581.643	0.0058	13.811
CH_3OH 1 1 +- 0 0 +	350905.1	0.915	97.142	684.78	0.0088	13.906
CH_3OH 4 1- 3 0	358605.799	0.386	114.671	454.137	0.0032	14.059
CH_3OH 4 1- 3 0	358605.799	0.218	118.895	581.643	0.0017	13.811
CH_3OH 4 1- 3 0	358605.799	0.271	97.142	684.78	0.0026	13.906
CH_3OH 7 2- 6 1	363739.868	0.096	114.671	454.137	0.0008	14.059
CH_3OH 7 2- 6 1	363739.868	0.067	97.142	684.78	0.0006	13.906
SiO 7- 6	303926.96	0.728	200	548.9928	0.0034	12.38
SiO 8- 7	347330.631	0.679	200	548.9928	0.0032	12.38
HNCO 13 1 13-12 1 12	284662.172	0.146	114.671	454.137	0.0012	13.675
HNCO 13 1 13-12 1 12	284662.172	0.44	118.895	581.643	0.0035	14.015
HNCO 13 1 13-12 1 12	284662.172	0.273	97.142	684.78	0.0026	13.566
HNCO 13 0 13-12 0 12	285721.951	0.576	114.671	454.137	0.0047	13.675
HNCO 13 0 13-12 0 12	285721.951	1.491	118.895	581.643	0.0118	14.015
HNCO 13 0 13-12 0 12	285721.951	0.678	97.142	684.78	0.0066	13.566
HNCO 13 1 12-12 1 11	286746.514	0.145	114.671	454.137	0.0012	13.675
HNCO 13 1 12-12 1 11	286746.514	0.438	118.895	581.643	0.0035	14.015
HNCO 13 1 12-12 1 11	286746.514	0.273	97.142	684.78	0.0026	13.566
HNCO 14 1 14-13 1 13	306553.733	0.116	114.671	454.137	0.001	13.675
HNCO 14 1 14-13 1 13	306553.733	0.369	118.895	581.643	0.0029	14.015
HNCO 14 1 14-13 1 13	306553.733	0.254	97.142	684.78	0.0025	13.566
HNCO 14 0 14-13 0 13	307693.905	0.458	114.671	454.137	0.0037	13.675
HNCO 14 0 14-13 0 13	307693.905	1.247	118.895	581.643	0.0099	14.015
HNCO 14 0 14-13 0 13	307693.905	0.631	97.142	684.78	0.0061	13.566
HNCO 14 1 13-13 1 12	308798.184	0.115	114.671	454.137	0.0009	13.675
HNCO 14 1 13-13 1 12	308798.184	0.366	118.895	581.643	0.0029	14.015
HNCO 14 1 13-13 1 12	308798.184	0.254	97.142	684.78	0.0025	13.566
HNCO 15 0 15-14 0 14	329664.367	0.344	114.671	454.137	0.0028	13.675
HNCO 15 0 15-14 0 14	329664.367	0.992	118.895	581.643	0.0078	14.015
HNCO 15 0 15-14 0 14	329664.367	0.562	97.142	684.78	0.0054	13.566
HNCO 16 0 16-15 0 15	351633.257	0.246	114.671	454.137	0.002	13.675
HNCO 16 0 16-15 0 15	351633.257	0.753	118.895	581.643	0.0059	14.015
HNCO 16 0 16-15 0 15	351633.257	0.482	97.142	684.78	0.0047	13.566
HNCO 17 0 17-16 0 16	373600.448	0.167	114.671	454.137	0.0014	13.675
HNCO 17 0 17-16 0 16	373600.448	0.546	118.895	581.643	0.0043	14.015
HNCO 17 0 17-16 0 16	373600.448	0.398	97.142	684.78	0.0038	13.566

NO 4 -1 4- 3 1 3	350689.494	0.219	112	600	0.0018	14.69
NO 4 -1 4- 3 1 3	350689.494	0.169	114	700	0.0014	14.6
NO 4 -1 4- 3 1 3	350690.766	0.161	112	600	0.0014	14.69
NO 4 -1 4- 3 1 3	350690.766	0.124	114	700	0.001	14.6
NO 4 -1 4- 3 1 3	350694.772	0.117	112	600	0.001	14.69
NO 4 -1 4- 3 1 3	350694.772	0.09	114	700	0.0007	14.6
NO 4 1 4- 3 -1 3	351043.524	0.219	112	600	0.0018	14.69
NO 4 1 4- 3 -1 3	351043.524	0.169	114	700	0.0014	14.6
NO 4 1 4- 3 -1 3	351051.469	0.161	112	600	0.0014	14.69
NO 4 1 4- 3 -1 3	351051.469	0.125	114	700	0.001	14.6
NO 4 1 4- 3 -1 3	351051.705	0.117	112	600	0.001	14.69
NO 4 1 4- 3 -1 3	351051.705	0.09	114	700	0.0007	14.6
OCS 23-22	279685.318 1.911	483	669	0.0037	15.46	
OCS 24-23	291839.673 1.467	483	669	0.0029	15.46	

Table 8.2: NGC 4945 Gaussian fit.

Molecule Transition	ν (MHz)	AREA (mK Km s^{-1})	$\Delta V_{1/2}$ (km s^{-1})	V_{LSR} (km s^{-1})	T_{MB} K	N (cm^{-2})
HCN 4- 3	354505.4759	5.33904	250	5092.5117	0.0193	14.865
HCN 4- 3	354505.4759	5.60592	249.368	5332.5654	0.0203	14.889
C_2H 4 5 5- 3 4 4	349337.4558	0.95343	250	5116	0.0036	15.763
C_2H 4 5 5- 3 4 4	349337.4558	1.39878	250	5390	0.0052	15.933
C_2H 4 5 4- 3 4 3	349338.7284	0.76368	250	5116	0.0029	15.763
C_2H 4 5 4- 3 4 3	349338.7284	1.1216	250	5390	0.0042	15.933
C_2H 4 4 4- 3 3 3	349398.9061	0.74865	250	5116	0.0028	15.763
C_2H 4 4 4- 3 3 3	349398.9061	1.09961	250	5390	0.0041	15.933
C_2H 4 4 3- 3 3 2	349400.2918	0.55967	250	5116	0.0021	15.763
C_2H 4 4 3- 3 3 2	349400.2918	0.82293	250	5390	0.0031	15.933
CN v=0 1 3 0 3- 2 0 2	340031.544	0.33466	250	5390	0.0013	14.81
CN v=0 1 3 0 3- 2 0 2	340035.408	0.21125	250	5390	0.0008	14.81
CN v=0 1 3 0 4- 2 0 3	340247.77	0.32969	250	5390	0.0012	14.81
CN v=0 1 3 0 4- 2 0 3	340247.77	0.44782	250	5390	0.0017	14.81
CN v=0 1 3 0 4- 2 0 3	340248.5764	0.23954	250	5390	0.0009	14.81
CS 6- 5	293912.244	0.46807	250	5116	0.0018	14.664
CS 6- 5	293912.244	2.15568	250	5390	0.0079	15.34
CS 7- 6	342883	0.29071	250	5116	0.0011	14.664
CS 7- 6	342883	1.35646	250	5390	0.005	15.34
HCO^+v=0 1 2 4 0 0- 3 0 0	356734.134	1.53897	250	5116	0.0057	14.075
HCO^+v=0 1 2 4 0 0- 3 0 0	356734.134	3.84301	250	5390	0.0141	14.485
HNC 4- 3	362630.303	2.0746	250	5116	0.0077	14.411
HNC 4- 3	362630.303	7.68349	250	5390	0.0274	15.01
OCS 23-22	279685.318	1.52781	250	5230	0.0057	16.161
OCS 23-22	279685.318	3.54816	250	5540	0.0133	16.53
OCS 24-23	291839.673	1.65088	250	5230	0.0062	16.161
OCS 24-23	291839.673	3.82208	250	5540	0.0143	16.53

H_2S 3 3 0- 3 2 1	300505.56	1.12236	250	5116	0.0042	15.76
H_2S 3 3 0- 3 2 1	300505.56	1.1203	250	5390	0.0042	15.76
H_2S 3 2 1- 3 1 2	369101.45	2.48542	250	5116	0.0093	15.76
H_2S 3 2 1- 3 1 2	369101.45	2.48086	250	5390	0.0093	15.76
CH_3OH 6 1 - 5 1 +	287670.767	0.14868	250	5390	0.0006	15.609
CH_3OH 6 0- 5 0	289939.377	0.16441	250	5390	0.0006	15.609
CH_3OH 6 -1- 5 -1	290069.747	0.23342	250	5390	0.0009	15.609
CH_3OH 6 0 +- 5 0 +	290110.637	0.16348	250	5116	0.0006	15.32
CH_3OH 6 0 +- 5 0 +	290110.637	0.31695	250	5390	0.0012	15.609
CH_3OH 6 1 – 5 1 -	292672.889	0.15013	250	5390	0.0006	15.609
CH_3OH 3 0- 2 -1	302369.773	0.22213	250	5390	0.0008	15.609
CH_3OH 1 1 – 1 0 +	303366.921	0.39522	250	5116	0.0015	15.32
CH_3OH 1 1 – 1 0 +	303366.921	0.76476	250	5390	0.0029	15.609
CH_3OH 2 1 – 2 0 +	304208.348	0.48682	250	5116	0.0018	15.32
CH_3OH 2 1 – 2 0 +	304208.348	0.94126	250	5390	0.0035	15.609
CH_3OH 3 1 – 3 0 +	305473.491	0.37053	250	5116	0.0014	15.32
CH_3OH 3 1 – 3 0 +	305473.491	0.71716	250	5390	0.0027	15.609
CH_3OH 4 1 – 4 0 +	307165.924	0.30223	250	5116	0.0011	15.32
CH_3OH 4 1 – 4 0 +	307165.924	0.58534	250	5390	0.0022	15.609
CH_3OH 5 1 – 5 0 +	309290.36	0.20918	250	5116	0.0008	15.32
CH_3OH 5 1 – 5 0 +	309290.36	0.40545	250	5390	0.0015	15.609
CH_3OH 3 1- 2 0	310192.994	0.14544	250	5116	0.0005	15.32
CH_3OH 3 1- 2 0	310192.994	0.28207	250	5390	0.0011	15.609
CH_3OH 6 1 – 6 0 +	311852.612	0.24234	250	5390	0.0009	15.609
CH_3OH 7 0- 6 0	338124.488	0.13517	250	5390	0.0005	15.609
CH_3OH 7 -1- 6 -1	338344.588	0.19347	250	5390	0.0007	15.609
CH_3OH 7 0 +- 6 0 +	338408.698	0.13448	250	5116	0.0005	15.32
CH_3OH 7 0 +- 6 0 +	338408.698	0.26087	250	5390	0.001	15.609
CH_3OH 4 0- 3 -1	350687.662	0.17202	250	5116	0.0006	15.32
CH_3OH 4 0- 3 -1	350687.662	0.33363	250	5390	0.0013	15.609
CH_3OH 1 1 +- 0 0 +	350905.1	0.57932	250	5116	0.0022	15.32
CH_3OH 1 1 +- 0 0 +	350905.1	1.12033	250	5390	0.0042	15.609
CH_3OH 4 1- 3 0	358605.799	0.17604	250	5116	0.0007	15.32
CH_3OH 4 1- 3 0	358605.799	0.34143	250	5390	0.0013	15.609
CO 3- 2	345795.9899	66.93822	299.18	5138	0.1958	17.87
CO 3- 2	345795.9899	29.47334	213.915	5420	0.1241	17.493
CO^+ 3 3- 2 2	353741.262	0.19873	205	5380	0.0009	13.625
CO^+ 3 4- 2 3	354014.247	0.28389	205	5380	0.0013	13.625
SiO 7- 6	303926.96	0.98022	363	5350	0.0025	14.79
SiO 8- 7	347330.631	0.55342	363	5350	0.0014	14.79
$C^{34}S$ 6- 5	289209.23	0.79481	450	5350	0.0017	14.9
$C^{34}S$ 7- 6	337396.6901	0.50251	450	5350	0.001	14.9
N_2H^+ v=0 3- 2	279511.7348	7.97901	519.35693	5353	0.0139	14.86
N_2H^+ v=0 4- 3	372672.4645	7.8416	519.35693	5353	0.0138	14.86

Table 8.3: Arp 220 Gaussian fit.

Part III

APPENDIX C: Molecules in the extragalactic medium

Up to now there are more than 60 molecular species detected in the extragalactic medium, from diatomic molecules as CS to 8-atom molecules as HC_6H. Most of them are organic molecules, that is, such they contain Carbon atoms.

All molecules have been detected by rotational spectroscopy in the radiofrequency to far-infrared spectral regions unless indicated otherwise. * indicates molecules that have been detected by their rotation-vibration spectrum, Fig. 4.1 shows the list of detected molecules, where ** indicates molecules detected by electronic spectroscopy only.

2 atoms	3 atoms	4 atoms	5 atoms	6 atoms	7 atoms	8 atoms	>8 atoms
OH	H_2O	H_2CO	*c*-C_3H_2	CH_3OH	CH_3CCH	HC_6H	*c*-C_6H_6 *
CO	HCN	NH_3	HC_3N	CH_3CN	CH_3NH_2		C_{60}* (?)
H_2 *	HCO^+	HNCO	CH_2NH	HC_4H *	CH_3CHO		
CH	C_2H	C_2H_2 *	NH_2CN	$HC(O)NH_2$			
CS	HNC	H_2CS ?	*l*-C_3H_2				
CH^+ **	N_2H^+	$HOCO^+$	H_2CCN				
CN	OCS	*c*-C_3H	H_2CCO				
SO	HCO	H_3O^+	C_4H				
SiO	H_2S	*l*-C_3H					
CO^+	SO_2						
NO	HOC^+						
NS	C_2S						
NH	H_2O^+						
OH^+	HCS^+						
HF	H_2Cl^+ 2014						
SO^+	NH_2 2014						

Figure 8.8: Extragalactic moleules reported in The Cologne Database for Molecular Spectroscopy.

8.7 Molecular transitions

When two or more atoms together are forming a molecule, they constitute a more complex system than in the case of a single atom. One way to approach the study of complex spectroscopy systems is by using the Born-Oppenheimer approximation that assumes that the motion of atomic nuclei and electrons in a molecule can be separated. A molecule shows three kinds of transitions: (a) Rotational transitions, i. e. rotation of the nucleus respect to the centre of mass; (b) Vibrational transitions, i. e. the nuclus vibrates around the equilibrium position; (c) Electronic transitions, i. e. a change in the distribution of the electronic cloud. When a rotational transition ocurrs from vibrationally excited levels, the observed transitions are know as vibrational-rotational transition.

CO is the second most abundance molecule in the Interstellar medium. Its relative abundance with respect to H_2 is $[CO/H_2] \simeq 1.8 \times 10^{-4}$. H_2 lacks a dipolar momentum and hence can only radiate throught electric quadrupole transitions. Therefore it is observable directly in molecular clouds only in high temperatures ($T \geq 100K$) regions.

8.7.1 Electronic transitions

In the Born-Oppenheimer approximation, we can define "a", the molecular size (1 Å), "M", a typical molecular mass (M∼10mp), and "m" the electron mass
In the Born-Oppenheimer approach the total energy of the molecule is

$$E = E_{el} + E_{vib} + E_{rot}$$

By the uncertainty principle, $\Delta p \Delta x \simeq pa \simeq \hbar$, the momentum is $p \simeq \hbar/a$, and the energy is $E = p^2/2m$; then the separation between levels will be

$$Eel \simeq \hbar^2 / ma^2$$

Then using the values, $E_{el} \simeq 7.5$eV at $\lambda_{el} = 1700\ \mathring{A}$ in the UV spectral range.

8.7.2 Vibrational transitions

For stable molecules the internuclear potential has a minimun for the nuclear separation. One can approach the vibration of a nucleus around the equilibrium position with angular frequency ω and amplitude ϵ less a. The oscillator energy is $E_{vib} \simeq 1/2\ M\omega^2\ \epsilon^2$; in the limit case $\epsilon \simeq a$, the energy should be of the order by an harmonic oscilator.

$$\omega \simeq (\hbar^2 / mMa^4)1/2, \text{ then } Evib \simeq (m/M)E_{el}$$

Where Eel is the electronic energy. Tipicaly $E\text{–}vib \simeq 0.06$eV, which corresponds to $\lambda_{vib} = 23\mu$m, in the IR spectral range.

8.7.3 Rotational transitions

The angular momentum of the molecule is quantified and is a multiple of $\hbar$. For lower rotational levels , $L = I\omega \simeq \hbar$, with $I \simeq Ma^2$ being inertia momentum of the molecule. One obtains that the rotational energy is given by:

$$Erot \simeq (m/M)Eel$$

For example $E_{rot} = 4x10^{-4}$eV, which correspond to $\lambda rot = 3.1$mm in radio band.

8.7.4 Rotational spectrum and their moments of inertia

The rotational spectrum of molecules are divided into three groups regarding their moments of inertia:

- Linear molecules: This is the case of diatomic molecules (e.g. CS). The ωangular momentum in this case depends upon one moment of inertia, I.

$$L = I\omega \text{ with } \omega \text{ being the angular frequency of the rotation.}$$

The energy of the rotational quantum level with number, J, is:

$$E_J = hBo[J(J+1)]$$

where Bo is the rotational constant given by.

$Bo = h/\ 8\pi\ ^2I$

- Symmetric rotors. This kind of molecules have two moments of inertia with rotational constants B and C. The energy of their rotational levels are defined by two quantum numbers J and K:

$$E(J,K) = h[BJ(J+1)+(C-B)K^2]$$

where J is the quantum number asociated with the total angular momentum, and K the one associated with its projection onto the simetric axis of the molecule, with $K \leq J$

- Asymmetric rotors. The three moments of inertia are different.

8.8 Molecular Structure

Fine and hyperfine structure

The rotational levels are usually degenerate. The degeneracy in the rotational levels can be broken by perturbation induced by e.g. the nuclear spin. This will give rise to the fine and hyperfine structure in the rotational energy levels. There are observed lines formed by a group of hyperfines components not resolved. In this case, the relative intensity of this components is included in the spectroscopical parameters which cannot be resolved due the broad linewidth observed in molecular clouds and is usually independent of the excitation temperature of the gas.

8.8.1 The molecules of this thesis

In this section we show different example of the structure of the molecules considered in this thesis:

- CH_3OH: METHANOL
- CH3CCH: METHYL ACETYLENE (Propyne)
- C2H: ETHYNYL
- CS: CARBON MONOSULFIDE
- C2S: Carbon Disulfide
- c-C3H2: Cyclopropenylidene
- CH3CHO: ETHANAL

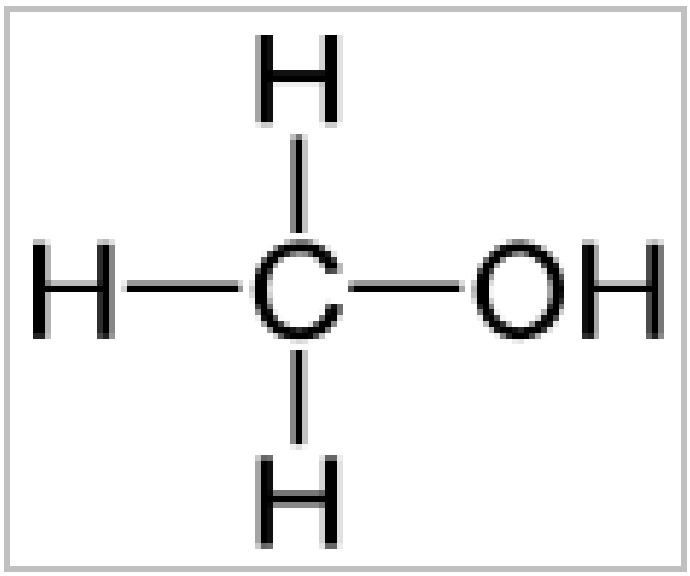

Figure 8.9: Methanol structure.

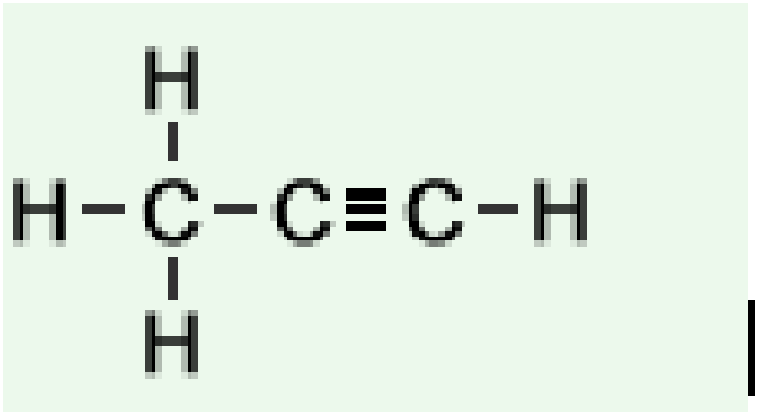

Figure 8.10: Methyl acetylene molecule.

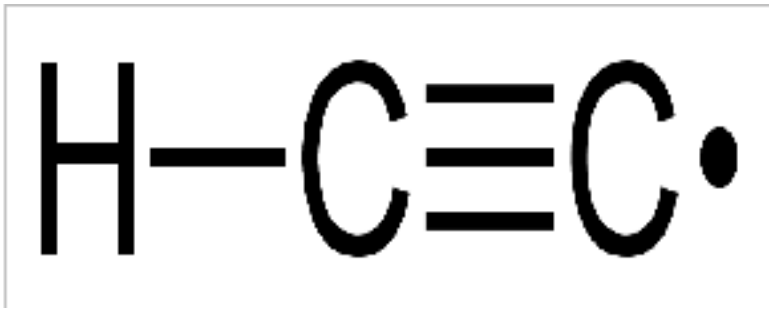

Figure 8.11: Ethynyl molecule.

- C3H : Propynylidyne
- CH2CO: Ethanone
- CH3NH2: Methylamine
- CH3CN: METHYL CYANIDE

Figure 8.12: CARBON MONOSULFIDE molecule .

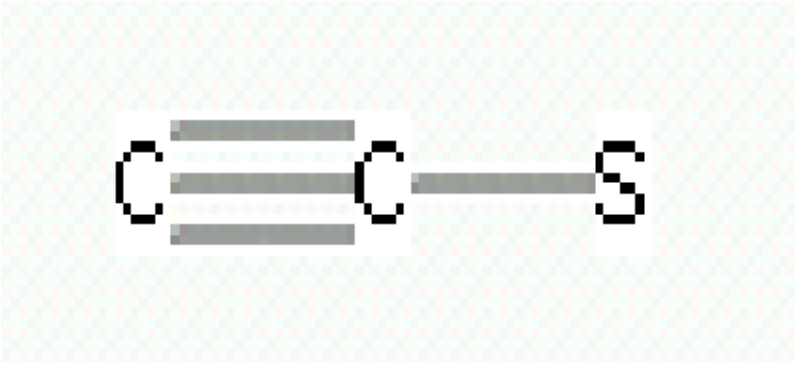

Figure 8.13: Carbon Disulfide molecule.

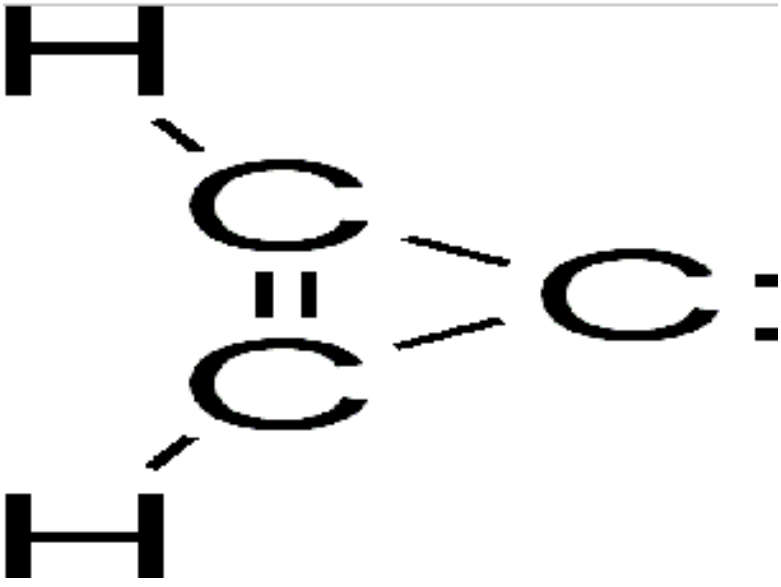

Figure 8.14: Cyclopropenylidene molecule.

- CN: Cyanide
- CO: Carbon monoxide
- CH2NH: METHANIMINE

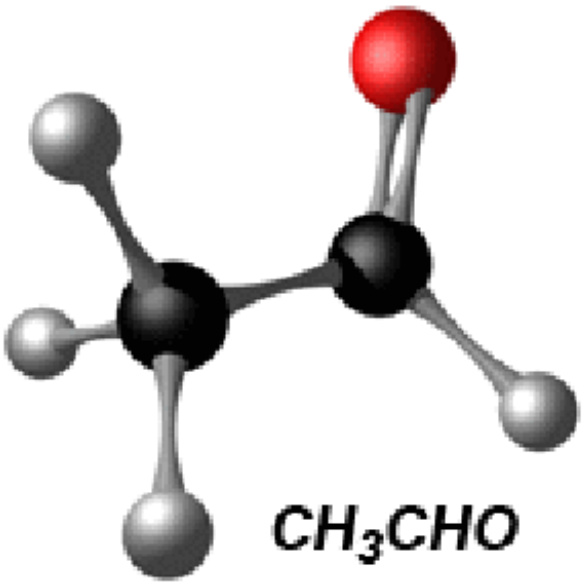

Figure 8.15: ETHANAL .

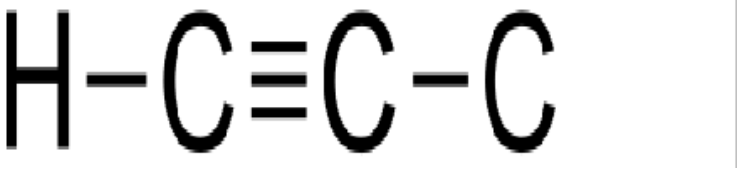

Figure 8.16: Propynylidyne.

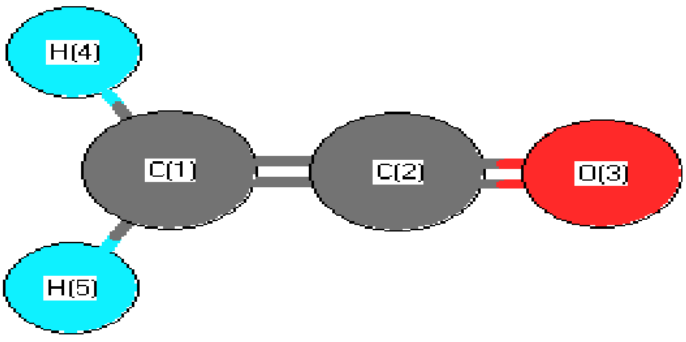

Figure 8.17: Ethanone.

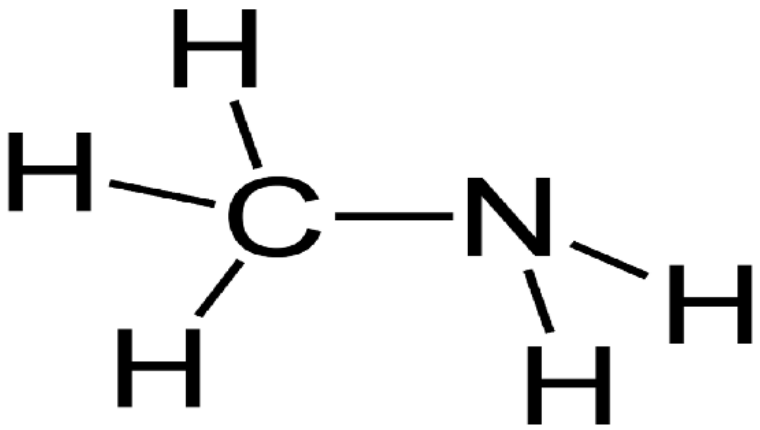

Figure 8.18: Methylamine.

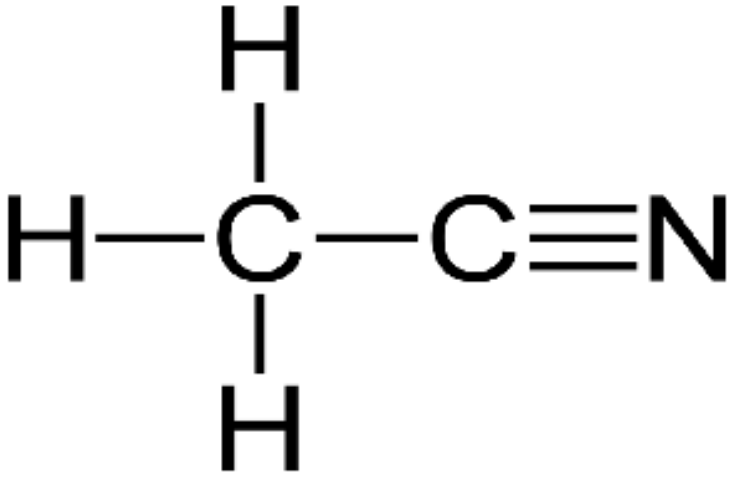

Figure 8.19: METHYL CYANIDE.

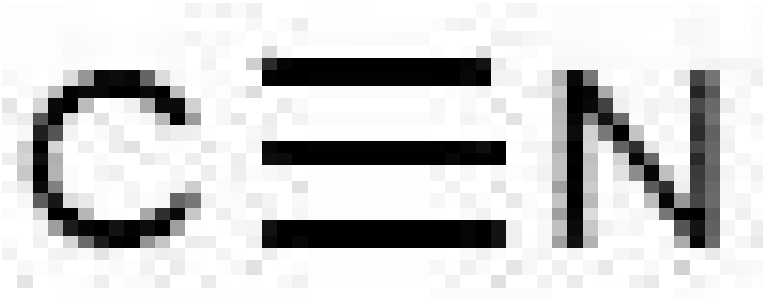

Figure 8.20: Cyanide.

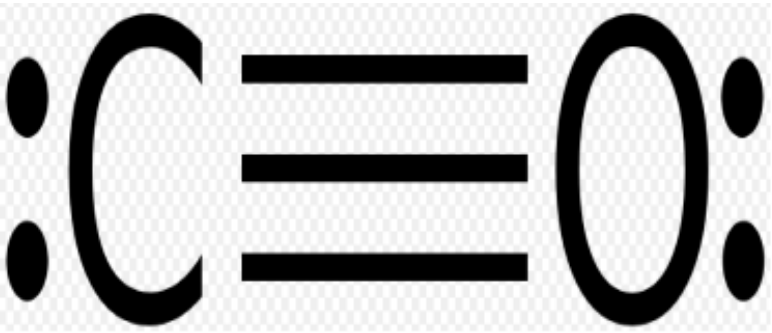

Figure 8.21: Carbon monoxide.

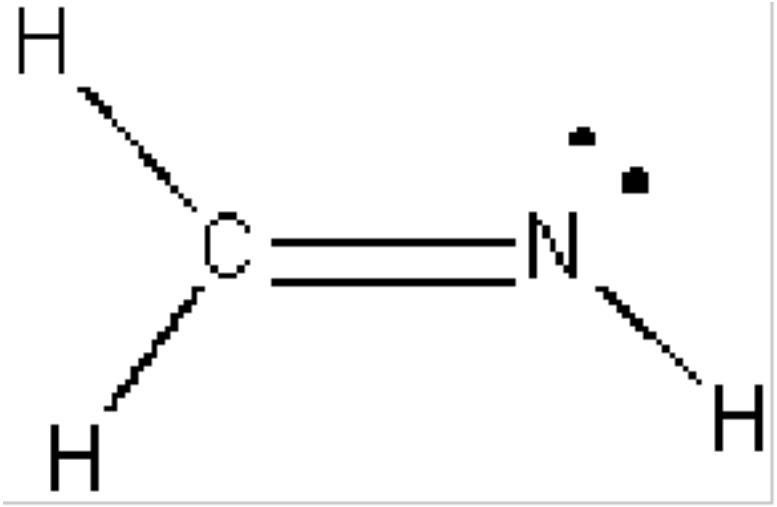

Figure 8.22: Methanimine.

Part IV

REFERENCES

REFERENCES